Spherical Silicon for Photovoltaic Applications: Material, Modeling and Devices

by

Majid Gharghi

A thesis

presented to the University of Waterloo

in fulfillment of the

thesis requirement for the degree of

Doctor of Philosophy

in

Electrical and Computer Engineering

Waterloo, Ontario, Canada 2007

I hereby declare that I am the sole author of this thesis. This is a true copy of the thesis, including any required final revisions, as accepted by my examiners.

Majid Gharghi

I understand that my thesis may be made electronically available to the public.

Majid Gharghi

Abstract

Detailed material characterization of spherical silicon is conducted for the first time. Experimental results on crystallinity, impurities, and structural defects are presented to investigate the effect of growth mechanism and processing of the spheres.

Based on the material properties, the spherical bulk is characterized from electronic point of view. A model is developed to interpret photoconductivity decay measurements and extract minority carrier lifetime, the most influential parameter in device performance. The model includes the spherical geometry as well as the radial profile of carrier lifetime and the measurement results are used to characterize the quality of the spheres and the effectiveness of the process steps.

To analyze and predict the performance of spherical cells, a three dimensional opto-electric model is developed. The model separately treats the optical generation and carrier collection and is able to calculate the spectral response and the device characteristics. A simulation tool is created based on this model. The simulation results are of great importance in designing novel structures and optimizing fabrication processes.

The necessary characterization methodologies are developed to measure the spectral response and I-Vcharacteristics of individual cells, as well as an array consisting of several cells.

A new device design with passivated selective emitter is proposed based on simulation results. Plasma processes were developed to selectively etch back the deep emitter of the spherical cells using reactive ion etching, and then passivate the surface using plasma enhanced chemical vapor deposition of silicon nitride. The improvement in characteristics of the fabricated device is characterized using the developed measurement setups.

Industrial up-scaling and manufacturability of the proposed devices and processes are also discussed.

Acknowledgment

I wish to sincerely express my gratitude to:

Professor Siva Sivoththaman

for his supervision and support throughout this work;

Professor Xianguo Li, Professor Adel Sedra, Professor Andrei Sazanov, and **Professor My Ali El Khakani**

for accepting to review my work;

My colleagues **Hua Bai**, **Syed Iftekhar Ali**, **Dr. Mahdi Farrokh Baroughi, Bahareh Sadeghimakki, Cherry Cheng, Hassan Elgohary**

for precious cooperation and useful discussions;

Joseph Street, **Robert Mollins,** and **Richard Barber**

for their efforts in SIDIC and G2N Labs;

Gary Stevens and **Khalil Zeaiter** and other collaborators from **Spheral Solar Power**

for cooperation in sphere sample preparation, annealing and lifetime measurements;

Reza Chaji, Dr. Shahin Jafarabadashtiani, Mohammadreza Esmaeili-rad, **Saeed Fathololoumi,**

for the unforgettable time we spent as colleagues in Waterloo;

Maryam Moradi, Nader Safavian, Flora Li, Kai Wang, Hyon Jung Lee, and other members of **G2N Group**

for kind cooperation and useful discussions.

To my parents,

in gratitude and love

Contents

List of Figures

List of Tables

Publications Emanating From This Research

Journal

- M. Gharghi, S. Sivoththaman, *Photoconductivity Decay in Silicon Spheres in Response to Impulse Light Stimulation*, Journal of Materials Science: Materials in Electronics, v.18, n. S1, p. S111-S115.
- M. Gharghi, H. Bai, G. Stevens, S. Sivoththaman, *Three-Dimensional Modeling and Simulation of p-n Junction Spherical Silicon Solar Cells*, IEEE Transaction on Electron Devices, v.53, 2006, p1355-1363.
- M. Gharghi, S. Sivoththaman, *Formation of Nanoscale Columnar Structures in Silicon by a Maskless Reactive Ion Etching Process*, Journal of Vacuum Science and Technology A, v. 24, 2006, p723-727.
- S. Ali, M. Gharghi, S. Sivoththaman, K. Zeaiter, *Properties and Characterization of Low-Temperature Amorphous PECVD Silicon Nitride Films for Solar Cell Passivation*, Journal of Materials Science, v.40, 2005, p1469-1473.

Conference

- M. Gharghi, S. Sivoththaman, *Graded Silicon Based PECVD Thin Film for Photovoltaic Applications*, SPIE Optics and Photonics, Aug 2007, Proceeding of SPIE, vol. 6674, p66740A-1-10.
- B. Sadeghimakki, M. Gharghi, S. Sivoththaman, *Passivation of Si Nanopillars for Photovoltaic Applications*, the 13th Canadian Semiconductor Technology Conference Aug 2007.
- C. Cheng, M. Gharghi, S. Sivoththaman, *Surface Recombination in Spherical Silicon Used for Photovoltaic Applications*, the13th Canadian Semiconductor Technology Conference Aug 2007.
- M. Gharghi, S. Sivoththaman, *Photoconductivity Decay in Silicon Spheres in Response to Impulse Light Stimulation*, **presented at** the International Conference on Optical and Optoelectronic Properties of Materials and Applications, Jul 2006, Darwin, Australia.
- M. Gharghi, G. Stevens, S. Sivoththaman, *Interpretation of Photo-Conductivity Decay Lifetime in Silicon Spheres*, IEEE 4th World Conference on Photovoltaic Energy Conversion, May 2006, Hawaii, p1138-1141.
- M. Gharghi, S. Sivoththaman, *Formation of Micro and Nano-scale columnar structures in Silicon by a Maskless RIE Process*, **presented at** the 12th Canadian Semiconductor Technology Conference, Aug 2005, Ottawa.
- M. Gharghi, H. Bai, G. Stevens, S. Sivoththaman, *Modeling and Simulation of Spherical Solar Cells*, 31st IEEE Photovoltaic Specialists Conference, Jan 2005, Orlando, Florida, p1177-1180.
- S. Ali, M. Gharghi, S. Sivoththaman, K. Zeaiter, *Characterization of PECVD SiN for Surface Passivation*, **presented at** the International Conference on Physics, Chemistry, and Engineering of Solar Cells, May 2004, Spain.
- H. Bai, M. Gharghi, S. Sivoththaman, G Stevens, M. Hammerbacher, *A Quasi-Three-Dimensional Numerical Model for Spherical Photovoltaic Devices*, Tech. Digest of the 14th International Photovoltaic Science and Engineering Conference, Jan 2004, Thailand, p.769-770.

Submitted

- M. Gharghi, S. Sivoththaman, *Process Development for Tailoring the Emitter on Sphere Shaped Silicon Structures*, submitted to 33rd IEEE Photovoltaic Specialists Conference, May 2008, San Diego California.

Prepared Manuscripts

- M. Gharghi, S. Sivoththaman, *Advanced Spherical Solar Cell with Tailored Emitter Design and Surface Passivation* , submission to IEEE Electron Device Letters.
- M. Gharghi, S. Sivoththaman, *Structural Characterization of Spherical Silicon Crystals Grown from Powder*, submission to IEEE/TMS Journal of Electronic Materials.
- M. Gharghi, S. Sivoththaman, *Material and Electronic Properties of Silicon Spheres Fabricated for Photovoltaic Applications*, submission to Journal of Applied Physics.
- M. Gharghi, S. Sivoththaman, *Shallow and Deep Emitter Spherical Photovoltaic Devices*, submission to Semiconductor Science and Technology.
- M. Gharghi, S. Sivoththaman, *Minority Carrier Lifetime for Process Monitoring in Spherical Silicon*, submission to Semiconductor Science and Technology.
- M. Gharghi, S. Sivoththaman, *Process Modeling and Control of Dry Etching on Non-Planar Surfaces*, submission to Journal of Micromechanics and Microengineering.

Chapter 1

Introduction

The fact that fossil resources are limited and will soon end given the current consumption rate, and the environmental consequences of using these resources such as pollution and global warming drive the interest in the renewable energy sources for the years to come. The major renewable energy sources are biomass, hydroelectric, geothermal, solar, and wind. Among the renewable energy sources, photovoltaic (PV) is very attractive as it converts the solar energy directly into electricity. Replacing one kilowatt of electrical energy from fossil sources by photovoltaic energy reduces carbon dioxide emission by about one ton per year [1]. PV systems are durable, environmentally friendly, need little maintenance, and produce no hazardous byproduct or waste during the long term operation. Thus PV market has had a drastic growth in the past few years [2].

1.1 Photovoltaic Energy

Several technologies have been developed for fabrication of photovoltaic devices. Most of the photovoltaic systems today rely on silicon based devices. Single and multi crystalline materials are the largest category. Thin film glass substrate cells take advantage of thin film amorphous Si (no Si wafer required) and offer the opportunity of low temperature processing but suffer from poor long term stability. Other thin film technologies such as CdTe and CuInSe, although cheap

in fabrication, are not as widely industrialized due to low efficiency or lack of stability. Compound direct bandgap III-V semiconductors such as GaAs are too expensive for general terrestrial photovoltaic applications and are mainly used in space applications. Organic films and dyes have been also considered for solar energy conversion, yet are still far from efficient operation and especially long term stability.

Crystalline silicon constitutes approximately 85% of the solar PV industry [3]. The single crystalline and multi crystalline silicon made from melt and then cut into wafers are the most widely used materials. The main drawback of PV systems is the cost issue. PV energy is not yet economical for large-scale energy generation. The price of PV energy is 2 to 6 times greater than the price of the electricity obtained from hydroelectric, nuclear, and fossil sources [4].

1.2 Motivation for This Research

The key issues of PV technologies are material cost, conversion efficiency, stability, and durability. Material cost in silicon PV systems accounts for nearly 50% of module costs [5].

Another important issue in the solar cell technology is the maximum size of a photovoltaic module that can be processed, shipped, safely handled, etc. Si wafer based solar cells are limited in size to the maximum wafer area, which is in turn limited to ingot size and growth equipment. Also, module size can not be very large due to the fragile nature of the substrate materials.

A third emerging issue in the silicon PV industry is the shortage in the silicon feedstock. The very fast growth of PV cell industry has created an enormous demand for silicon wafers. The silicon industry has not been able to grow as quickly, and the demand for solar grade silicon has caused a feedstock crisis. The ingot growth and wafering are the bottlenecks to the high throughput production of solar grade silicon.

One approach to combine low cost feed stock with perfect performance of single crystal is spherical silicon. In this technology, Si spheres are made from low cost feedstock that is unusable in VLSI technology, and considered as silicon loss in the microelectronic industry. The start material might come from the metallurgical grade silicon MG-Si, poly-crystal rod ends (not suitable for Czochralski CZ or Float Zone FZ), reactor dust, or kerf loss during wafer cutting.

In addition to the low material expenses, the spherical silicon technology is an appropriate technique to address the feedstock crisis. The rod end and kerf loss provide high quality purified silicon that can be perfectly used to produce high quality spheres, which are used to fabricate photovoltaic cells without having to go through the ingot growth and wafering steps.

Spherical solar cell modules are not limited for the maximum size because of the flexibility of the modules and absence of any rigid substrate. It is possible to roll modules and carry them, wrap a building with them, or even spread them on floor like a carpet which is strong enough to walk on.

Based on the above mentioned features, spherical solar technology has proved to be promising for the future of photovoltaic systems.

1.3 Methodology of the Research

The past efforts in the field of spherical photovoltaic technology have been mainly dedicated to industrial manufacturability of solar modules, and little scientific work has been carried out on the material aspects of silicon spheres and device design of spherical cells. While the manufacturing has been established to the actual commercialization level for spherical modules, serious existing issues and limitations at the single sphere level prevent the fabrication of efficient cells. In order to approach high efficiency spherical cells, several crucial steps are required:

- Due to the importance of material properties in photovoltaic devices, it is important to investigate the growth mechanism and control materials properties of silicon spheres.

- Because of the direct connection of electronic properties with the device performance, models and characterization methodologies must be developed to monitor and enhance the electronic properties in silicon spheres.
- For device design and characterization purposes, models, simulation tools, and measurement methodologies need to be developed to include the geometry and material specific aspects and properties of spherical silicon.
- For enhanced efficiency, new designs beyond the existing primitive device structure are required along with process development to fabricate the new device designs.
- The practical considerations for feasibility of the approaches, processes, and new designs should be ensured to guarantee the industrial manufacturability is not intervened.

The above mentioned steps and methodology were followed in this research work and for the first time, a thorough and detailed scientific approach has been made towards understanding the material properties and designing high efficiency spherical photovoltaic devices. The materials quality control as is developed in this work and the fabrication of advanced devices are expected to provide a basis for the next generation spherical PV devices.

1.4 Organization of the Thesis

The following chapters of this thesis present the developed models, the results of materials and device characterization, and new advanced designs for solar devices according to the methodology of Section 1.3.

In Chapter 2, a brief overview of alternative silicon technologies for PV applications is given along with a more detailed description of spherical technology. Material growth and device fabrication are explained. The challenges and the disadvantages of the technology are highlighted.

Chapter 3 discusses the results of material characterization of spherical silicon. Different approaches are adopted to access the spherical bulk in order to characterize crystallinity, impurities, defects, etc. The results of material properties characterization are instrumental to the electronic characterization of the spherical silicon.

Chapter 4 is dedicated to the electronic properties of spherical silicon. The chapter covers a detailed modeling and characterization of carrier lifetime in silicon spheres. The carrier lifetime measurements are shown to be a useful tool for process monitoring and process developing. The spatial variation of carrier lifetime is also obtained.

The modeling and simulation of spherical devices is presented in Chapter 5. The model includes optical and electrical aspects of the devices. The simulation results provide information on how the materials properties affect efficiency and also on how to design advanced devices for maximum efficiency with certain material parameters.

Chapter 6 covers the different characterization approaches on several levels of standard and test modules and single device. The challenges of direct measurements on the individual devices, together with the setups developed specifically for the spherical cell/module measurements are discussed. The developed methodologies are later used to characterize the new device designs.

The new designs and the developed fabrication processes are presented in Chapter 7 with the characterization results. These designs include passivated devices, shallow emitter diodes, and selective emitter cells for maximum blue response of the cells.

Chapter 8 presents guidelines on the practical manufacturability of the proposed designs and processes to be industrially implemented in the actual production environment. These include process integration and equipment design for the manufacturing line.

The whole work is concluded in Chapter 9 of the thesis.

Chapter 2

Review of Alternative Silicon Materials for Photovoltaic Applications

The cost of material is one of the major issues to be addressed in order to move towards cost effective solar electricity. With crystalline silicon being the dominant technology, and given substrate material costs account for approximately 50% of the solar module production cost, feedstock preparation and crystallization have been the subject of extensive work in the silicon PV industry.

The first step in the silicon technology is reduction of silica from natural sources to low purity silicon called metallurgical grade silicon or MG-Si. Metallurgical grade silicon is then further purified through several chemical reactions to produce high purity semiconductor grade silicon (SG-Si), which is mostly in poly-crystalline form and serves as the melt stock for silicon crystallization. Once the desired purity of silicon material is produced, the material is fed to the crystallization system to grow a single- or multi- crystal substrate.

Both purity and crystal quality requirements are less stringent in the PV technology compared to the microelectronic technology, and thus several approaches have been adopted to reduce the cost of the silicon material by compromising the quality. The tolerable impurity levels in the solar grade silicon (Sol-Si) are usually in the part per million atomic (ppma) or below, where as much

lower impurity levels are required for integrated circuit fabrication. Moreover, while single-crystallinity and low defect density is vital in operation of electronic devices (mainly transistors), acceptable efficiencies are still achieved in solar cells fabricated using multi-crystalline silicon and substrates with relatively higher defect densities.

In this chapter, various silicon melt stock preparation schemes and crystallization approaches, including the spherical silicon technology, are reviewed to provide a comprehensive picture of all silicon materials used in solar PV, and the position of spherical silicon. In Section 2.1 the melt stock procedures for metallurgical grade, solar grade, and semiconductor grade start material are discussed. Alternative approaches to produce Sol-Si are briefly discussed and the typical impurity levels of different elements in Sol-Si are compared to those of MG- and SG- Si. In the following sections, the different crystallization approaches are reviewed. In Section 2.2, ingot technologies including Float Zone (FZ), Czochralski (CZ), and cast are compared for solar applications. While the first two result in higher quality single-crystal substrates, the lower cost wafers cut from a cast ingot are attractive for low cost terrestrial PV. In Section 2.3, the sheet or ribbon crystal technology is reviewed. These techniques usually produce multi-crystalline silicon sheets of lower quality compared to ingot technologies. The advantage of sheet technologies is that the cost and silicon loss due to wafering is eliminated, and also higher throughput can be achieved. The two spherical silicon technologies are discussed in Section 2.4, in which silicon spheres of diameters from 0.5 to 2 mm are produced by solidifying a certain mass of silicon into spherical beads. The produced silicon spheres act as tiny substrates for fabrication of single cells, which are later integrated into flexible holder foils and result in flexible solar modules.

2.1 Silicon Material Feedstock

2.2.1 Metallurgical Grade Silicon

The start source for silicon is silica (SiO_2) which is quite abundant in nature. Silica is reduced by means of carbon (in the form of coal, coke, or wood chips) to produce silicon and carbon monoxide. The process occurs at high temperature (>1500^{o}C), and the gaseous byproduct is evacuated from the furnace leaving behind silicon powder referred to as metallurgical grade silicon [6]. MG-Si has various applications in metals industry, yet contains large impurity concentrations that make it inappropriate for electronic applications. Typical impurity levels in MG-Si are summarized in Table 2.1.

2.2.2 Semiconductor Grade Silicon

The MG-Si must be further purified to meet specifications required for integrated circuit fabrication [6]. This is usually achieved by hydrochlorination of silicon. The most commonly used product is $SiHCl_3$ which forms at around 300^{o}C in a fluidized bed reactor. The gaseous or vaporized product of hydrochlorination is distilled for purification, and then decomposed at 1100^{o}C in a chamber where silicon deposits on some silicon “slim” rods that are supported by graphite electrodes and poly-crystalline rods form (known as Siemens method). The resulting silicon contains impurities below part per billion atomic.

An alternative technique is to use MG-Si and magnesium to form a silicide at around 500^{o}C, which when reacting with ammonium chloride in liquid ammonium, produces high purity silane (monosilane process). The resulting high purity silane gas is then entered to a furnace to decompose at above 700^{o}C (pyrolysis). Historically, slim rods were used for pyrolysis, yet more

recently, the gas is entered to a fluidized bed reactor; tiny silicon seeds are floating in the fluidized bed reactor, and silicon deposits in the form of granulars as silane decomposes.

Typical impurity levels in SG-Si are also summarized in Table 2.1. It is worth noting that crystal growth techniques for semiconductor silicon crystal technology enhance the purity even further by directional solidification of the melt during which impurities are segregated out of the solid phase. In spite of the high quality achieved, the high cost per wafer poses a barrier against wide utilization of SG-Si in PV, and except for high efficiency cells using FZ or high quality CZ, lower grade silicon is preferred to reduce the final module cost.

Table 2.1: Typical impurity levels in MG-Si and maximum levels in SG-Si (part per million atomic) [7]

Impurity	Al	B	P	C	Ca	Cr	Cu	Fe	Mg	Mn	Mo	Na	Ni	Ti	V	Zn	Zr
MG-Si	1200 to 4000	37 to 45	27 to 30		590	50 to 140	24 to 90	1600 to 3000		70 to 80	<10		40 to 80	150 to 200	100 to 200		30
SG-Si	.0008	.0002	0.008	0.5	.003	.003	.003	.010	.005	.003	.003	.005	.010	.003	.003	.005	.010

2.2.3 Solar Grade Silicon

While MG-Si suffers from small carrier diffusion length (the most critical parameter in silicon PV devices) due to high impurity concentrations, SG-Si production is too expensive to meet the cost requirements of solar PV especially for terrestrial applications. A compromising solution is the solar grade silicon (Sol-Si), in which silicon melt stock of acceptable purity (for PV applications only) is produced at lower costs compared to monosilane pyrolysis or Siemens processes.

The main approach in Sol-Si is to use alternative purification techniques that, although not as effective in impurity elimination, are much more cost effective compared to those used for SG-Si. One proposed technique is the use of segregation at melt solid interface during solidification of silicon in the carbon reduction of silica [8]. This technique has been employed in arc furnaces to

melt MG-Si and solidify higher purity silicon as the impurities rest in the melt phase. Directional solidification greatly enhances the impurity segregation phenomenon, and can even result in Sol-Si of comparable quality to SG-Si without the hydrochlorination process [9].

Another technique is to replace the Siemens (high temperature decomposition of trichlorosilane) or pyrolysis (of monosilane) processes with metal reduction of silicon tetrachloride. This can be simply achieved using zinc [10] or sodium [11], and results in acceptable Sol-Si without having to go through the high temperature decomposition processes.

Typical impurity concentration levels in Sol-Si produced in arc furnace with and without uni-directional solidification, and with metal reduction of silicon tetrachloride are given Table 2.2. Threshold impurity concentration values have been reported for silicon solar cells to operate efficiently (shown in Figure 2.1) [12]. It is generally accepted that the impurity levels below these thresholds are appropriate for the Sol-Si produced using different techniques including the ones mentioned above.

Table 2.2: Reported impurity levels in ppma in feedstock materials for solar applications

Impurity	Al	B	P	C	Ca	Cr	Cu	Fe	Mg	Mn	Mo	Na	Ni	Ti	V	Zn	Zr
arc reactor	7	7.5	0.8		35	5	2	40		5	5		5	5	5		5
arc reactor directional	1	6.8	0.45			0.003	0.015	0.030	0.005	0.003	0.010	0.003	0.030	0.005	0.003	0.005	0.012
metal (Na) reduction	3	10	100		1	10	1	10	1-10	10	10	10	10	10	10		10

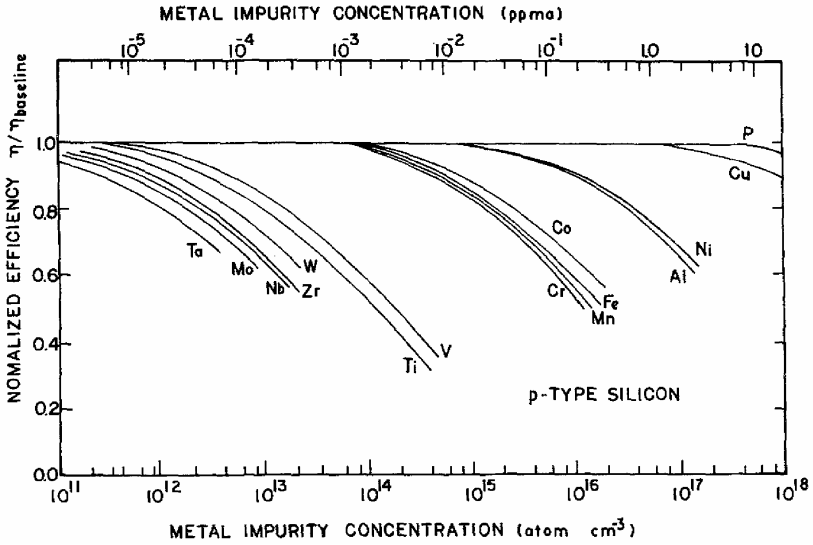

Figure 2.1: Tolerable impurity concentration levels for efficient silicon solar cell operation [12].

2.2 Ingot Silicon Technologies

Once the melt stock silicon is prepared, it is fed to a crystallization system, where the single- or multi- crystalline bulk is grown. In ingot technologies, the crystal is grown as a long silicon rod (ingot), and then cut into wafers after orientation flat has been formed. While the wafering step is almost identical in all cases, depending on the process used to grow the crystal, silicon ingots can be divided to three major categories that are discussed in this section.

2.2.1 Float Zone Silicon

In FZ technology [13], usually poly-rods from Siemens or pyrolysis undergo a zone-melting process, in which heater coils locally melt and recrystallize the silicon material while sweeping along the whole ingot length (Figure 2.2a). FZ usually results in highly pure (oxygen-free) ingots as the poly-rod does not touch any crucible or container during the crystallization, and defect density can be well controlled by the thermal pattern of the zone melting coils.

2.2.2 Czochralski Silicon

In CZ technology [14], broken chunks of poly-rods (from Siemens or pyrolysis) or granulars are fed into a melt load inside a crucible. The crystallization starts from a crystalline Si seed and proceeds as the solidified silicon is pulled up from the melt (Figure 2.2b). The turning and pulling speed are critical, as well as melt movement in the crucible (provided by stirring). Although very high quality ingots can be grown using this technique, the purity is poor compared to FZ as the melt is in contact with the crucible (causing higher oxygen inclusion).

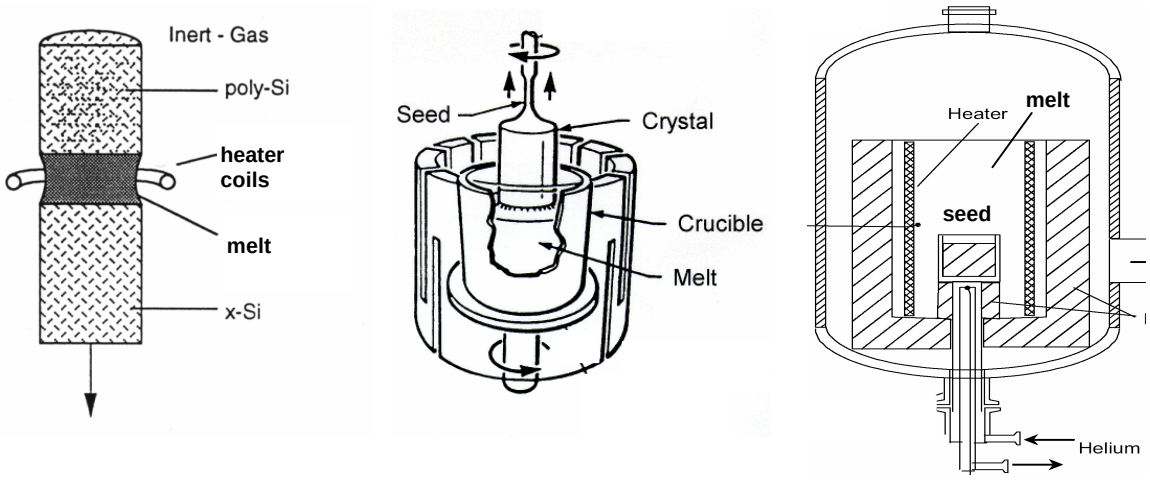

(a) (b) (c)

Figure 2.2: Schematic representation of different silicon ingot growth technologies (a) Float Zone [13] (b) Czochralski [14] (c) HEM cast [15].

2.2.3 Cast Silicon

FZ process is slow and difficult to control while CZ is more appropriate for large diameter ingots. However, in addition to the speed and stirring controls required, the moving parts in the CZ system make it difficult to maintain thermal isolation. Melting silicon chunks or granulars in a cast followed by a directional solidification results in multi-crystalline silicon ingots without any challenges for mechanical movement control or thermal isolation. The throughput of the cast

process can be higher as well. The melt is usually in touch with a cooled seed at the bottom of the crucible where crystallization starts. One well established scheme in cast ingot growth is the Heat Exchanger Method (HEM) [15] in which the cooling is provided by helium gas circulating in a circuit attached to the seed at the bottom of the crucible (Figure 2.2c). Although single-crystal ingots are impossible to grow in a cast, multi-crystals with large grain sizes can be obtained with much lower cost. Another advantage of the cast technique is that the cross section of the ingot does not have to be circular, and square wafers can be produced by slicing a rectangular cast ingot. This is important at the module level where packing factor of the cells must be maximized. In order to achieve close packing with round wafers, a considerable amount of the grown silicon crystal is lost by lapping. Figure 2.3 shows two 10x10 cm^2 cells from round single-crystal CZ and square multi-crystal wafer.

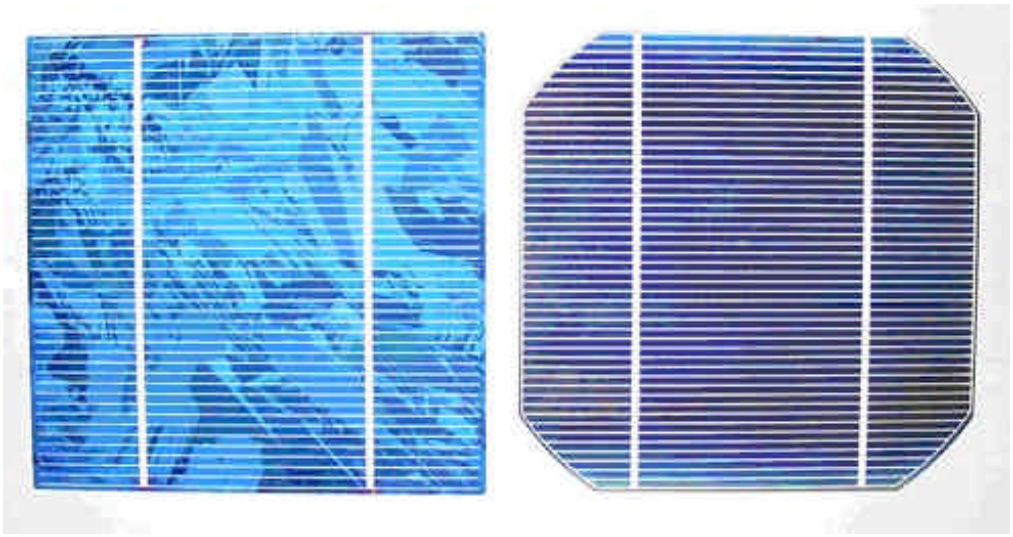

(a) (b)

Figure 2.3: 10x10 cm^2 silicon solar cells from (a) round single-crystal CZ and (b) square multi-crystal wafer.

2.3 Sheet Silicon Technologies

One of the major draw-backs of ingot technologies for solar cell fabrication is the wafering process required after the ingot is grown although high quality crystals can be obtained. The

slicing step is critical as a great portion of silicon is lost due to kerf loss when the diamond saw cuts the ingot. The sliced wafers still require several treatments; they are rounded at the edges and polished, and several chemical etches are performed between steps to remove damages from mechanical processes. An alternative approach for substrate production in the PV industry is the sheet or ribbon silicon technology. It has been proposed that if the equal efficiency of a cast multi-crystal is achieved with silicon sheet (eliminating the need to perform wafering), up to 40% cost reduction can be achieved in silicon solar cells. Several techniques have been used to grow silicon sheet from the melt. In this section, the most widely used techniques are reviewed.

2.3.1 Edge Supported Pulling

Edge supported pulling (ESP) [16] of silicon sheet form a melt load is shown in Figure 2.4, also known as string ribbon. The support rods are graphite or quartz filaments that move through the melt. In the special case that the silicon seeds are used in lieu of the filaments, the ribbon is called Dendritic web due to the resulting dendrite-like crystallization patterns.

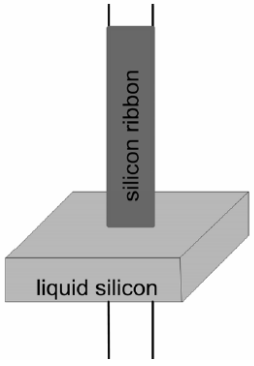

Figure 2.4: Vertical sheet pulling from silicon melt with edge supported pulling.

2.3.2 Edge-Defined Film-Fed Growth

Edge-defined film-fed growth (EFG) [17] is one of the most widely used ribbon techniques, in which the sheet is grown from the melt by pulling through a slit between two dies (Figure 2.5).

The growth speed of EFG is high compared to other techniques and the morphology of the resulting sheet is relatively uniform due to the defining slit. Yet the contact of the defining dies with the melt and melt-solid interface can cause high concentration of impurities in the sheet.

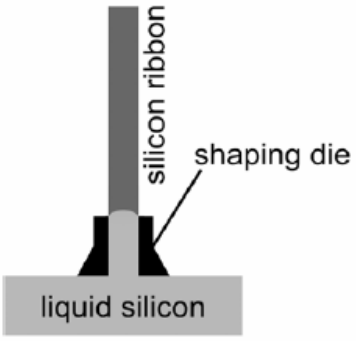

Figure 2.5: Vertical sheet pulling from silicon melt with edge-defined film-fed growth.

2.3.3 Ribbon Growth on Substrate

A third family of ribbon formation technologies depend on a fully supporting horizontal substrate for sheet growth. In ribbon growth on substrate (RGS) [18], the melt is dispensed on a substrate that moves horizontally against the melt container (Figure 2.6).

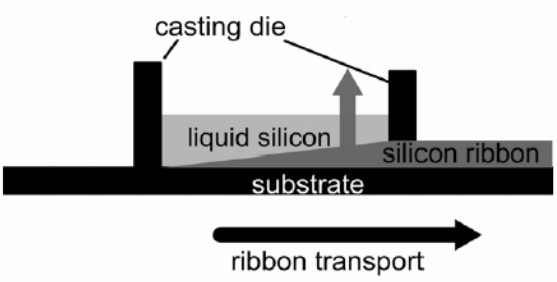

Figure 2.6: Substrate supported silicon sheet growth ribbon growth on substrate.

2.3.4 Other Sheet Technologies

Several other sheet technologies have been developed, but are not as widely used. In horizontally supported web (S-web) [19], a graphite net moves horizontally at the top of the silicon melt and

the sheet is formed by the support of the net. This is similar to RGS, except that the growth force is the adhesion of melt to the net as opposed to gravity.

In ribbon against dropping (RAD) [20], a carbon support sheet pulled vertically against the melt. The silicon sheet forms on the carbon shaper similar to the ESP technique. The carbon shaper is then burned-off in oxygen at high temperature. The technique is highly vulnerable to impurities as the melt and the whole area of the forming sheet are constantly in contact with the supporter.

In silicon sheet from powder (SSP) [21], silicon is dispensed in powder from and then recrystallized only at the outer layer by zone melting using lamp heaters. Once the top side of the powder layer is crystallized, the system is flipped, the substrate is separated, and the crystallized layer acts as the support for the crystallization of the remaining powder. SSP can lead to highly pure sheets, yet suffers from low throughput.

2.4 Spherical Silicon Technologies

A relatively new technique for material growth for PV applications is the spherical silicon. The cell size in the spherical technologies is not limited to the wafer or sheet size, and since the spheres can be produced at high speeds, the throughput of the material growth is higher compared to any planar technology. Moreover, because of the size of the growing crystal (0.5 to 2 mm diameter spheres), the morphology and the grain sizes are not as challenging as in silicon sheet technology.

2.4.1 Dropping Method

In the dropping method [22], certain masses of silicon melt are dispensed from nozzles at the top of a cooling tower. As the silicon droplets travel down along the tower in an inert ambient, they solidify into spheres; 1~2 mm diameter spheres are collected at the bottom of the tower (Figure

2.7). The study performed on the growth mechanism of the dropping method shows that the spheres are inherently of poly-crystalline structures [23]. X-ray diffraction patterns are in agreement with the poly formation during dropping [24]. Several attempts have been made to enhance the quality of the forming crystal, including condensation rate control by lowering the pressure in the cooling tower [25] and crystal seed implantation by spraying tiny crystalline silicon clusters into the melt droplets [26]. Also, hydrogen plasma treatment has been employed to passivate defects in the solid state after the sphere is grown [27].

Since the droplet is in close contact with the nozzle before being dispensed in the cooling tower, the contamination level of the spheres can be high even if high purity melt stock is used. Phosphorous gettering at the final device fabrication steps (after emitter diffusion) has proved to be effective in deactivation of electronic defects [28].

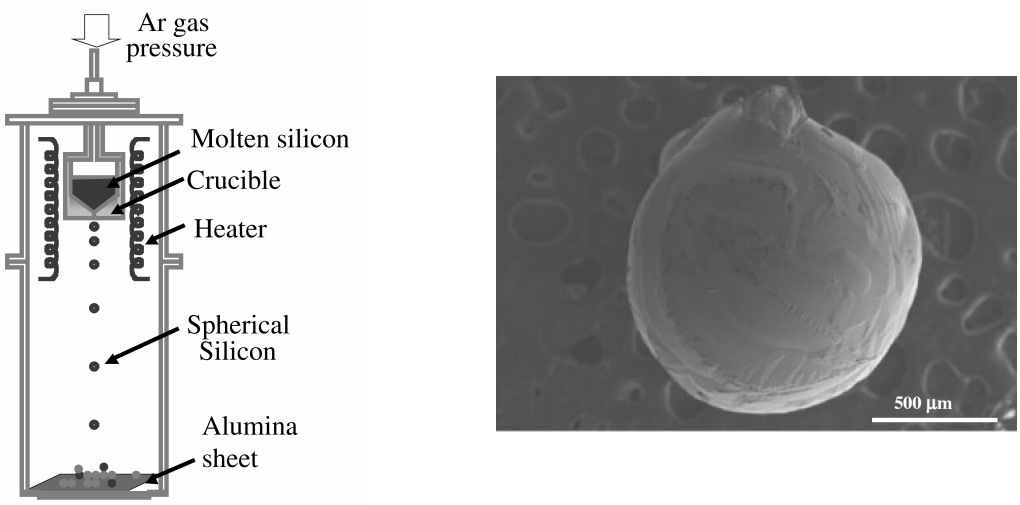

(a) (b)

Figure 2.7: Spherical silicon formation with dropping method (a) the cooling tower schematic (b) micrograph of a sphere collected at the bottom of the tower (poly-crystalline) [22].

2.4.2 Spheroidization by Surface Tension

A second approach to grow silicon in the spherical form is to use the surface tension of molten silicon. For this purpose, silicon powder or small silicon clusters are dispensed in lumps of certain mass and melted on an appropriate substrate in a belt furnace. Due to surface tension of the liquid state, the silicon lump adopts a spherical shape (spheroidizes) as soon as it melts and spheres of less than 1 mm diameter solidify in a controlled manner as they slowly move towards lower temperature zones of the furnace and finally exit. After the formation, the spherical shape is enhanced by mechanical grinding in an air jet grinder [29], and the spheres are sorted for shape and size control [30].

This technique was initially invented in Texas Instruments with the trademark of Spheral Solar^{TM} technology. Since the Spheral technology was initially considered to make use of low purity feedstock (MG-Si and off-spec SG-Si) for solar applications, the attention was mainly directed towards impurity control [31]. To achieve higher purity spheres, sequences of repeated melt and etch processes are considered; during each melt and recrystallization step, the impurities are segregated towards the surface region that is protected by an oxide layer. The oxide and the contaminated silicon are then removed from the surface by chemical etching. Models [32], as well as experimental approaches [33] have been developed to control the impurity level and determine the required number of melt and etch steps depending on the quality of the start feedstock material. Since the electronic properties of the spherical silicon crystals were mainly affected by the impurity concentration level, the growth mechanism, the crystallinity of the spheres, and other crystallization aspects and material properties have received less attention. The flexibility of the Spheral modules has been a motivation to several inventions at the module level, i.e. beyond the material and device aspects of the spherical silicon [34, 35]. As was mentioned in Section 1.3, the focus of the current work is on single sphere material and device aspects rather

than at module level. However, module level considerations are inevitable for some process developments and electrical characterizations.

2.5 Summary

The different material purification schemes and crystal growth approaches for photovoltaic applications were reviewed in this chapter. The solar grade silicon is a compromise between the low quality metallurgical grade and expensive semiconductor grade silicon, and provides silicon melt stock of acceptable quality and cost for PV applications. The crystal growth of silicon in different technologies was reviewed; while the ingot technologies produce high quality crystals, the sheet technologies eliminate the wafering cost and are more desirable for terrestrial PV applications. The spherical silicon is the most recent technology for growth of solar silicon; the possible schemes are dropping silicon melt and spheroidization by surface tension. The spheres can be produced with high throughput and the resulting spheres can be used to manufacture flexible modules. The spheroidized silicon introduced in this chapter will be investigated in the aspects of material and device in the following chapters of this thesis.

Chapter 3

Growth and Characterization of Spherical Silicon: Experimental Results on Material Properties

The spherical silicon is a novel crystal structure, which differs from conventional ingot silicon substrate used in microelectronics or other conventional semiconductor technologies, in the sense of crystal formation and properties, material solidification, impurity, defect, etc.

In order to theoretically model and experimentally develop advanced spherical device structures, and to propose and optimize appropriate process steps for enhanced device fabrication, it is necessary to comprehensively characterize silicon spheres from a material point of view. Accurate understanding of the crystal structure and the impurities is also crucial for the design and implementation of processes such as gettering, hydrogenation, defect passivation, or other improvement techniques at the material level.

Unfortunately, most of the existing characterization techniques are designed based on the planar wafer geometry and are not applicable to the spheres. Moreover, since the crystal formation is totally different from conventional ingot crystal, traditional models and theoretical approaches to identify and study defect formation and defect density are not applicable to silicon spheres. Therefore, modeling approaches, characterization techniques, and data interpretation techniques must be designed or modified according to the geometry and material specific characteristics.

In this chapter, a systematic study is performed to characterize the structural properties of spherical semiconductor silicon. In Section 3.1, the formation processes of silicon spheres from optically fused powder and granular silicon are discussed. The growth is in fact the basis to the material properties which will be characterized throughout the following sections of this chapter. One important property is the radial profile of material parameters which is challenging to characterize. The adopted approaches for radial bulk characterization are also discussed in this section. The very basic property of the spherical silicon, i.e. the crystallinity is discussed in Section 3.2, where it is shown that the spherical silicon possesses crystal properties very close to that of single crystalline quality. This reassures that electrodynamic and electronic processes are identical to the well known semiconductor silicon phenomena. In Section 3.3, modeling and experimental characterization of metallic impurity distribution are presented. The effect of different process steps through the fabrication flow of spherical cells are explored, and it is shown that depending on the start feedstock quality, different impurity levels can be observed, yet the recrystallization of spheres effectively reduces impurity levels. In Section 3.4, the distribution of oxygen and the effect of denuding on the oxygen density profile are characterized. Section 5 discusses the experimental results of defect characterization by delineation. Using defect etching, the creation and evolution of defects in the spherical bulk throughout the fabrication process are monitored. These material characterizations are later used both for extraction of electronic properties spherical of silicon, and for modeling and design of spherical devices.

3.1 Formation of Spherical Silicon

Depending on the start material for the production of silicon spheres, powder silicon or granular silicon may be used to form spheres. The powder is optically fused into silicon clusters of sizes close to the desired sphere size. The optically fused powder (OFP) clusters are later melted and

recrystallized to a sphere form. Granular silicon beads are directly used to produce silicon spheres through melt and recrystallization steps.

3.1.1 Optically Fused Powder

Powder silicon might come from the metallurgical grade silicon MG-Si, poly-crystal rod ends (not suitable for Czochralski CZ or Float Zone FZ), reactor dust, or kerf loss during wafer cutting. MG-Si is the start point of silicon industry and is obtained by reduction of silica using carbon. The MG-Si usually contains a considerable amount of metallic and non-metallic impurities including aluminum, iron, carbon, calcium, etc. in the microelectronic industry, MG-Si is then purified to semiconductor grade silicon SG-Si; by hydrochlorination of MG-Si gaseous silicon compounds (with hydrogen and chlorine) are obtained, which are later distilled and decomposed to produce high purity silicon. The decomposition usually takes place at elevated temperature in a reactor and silicon is deposited on silicon rods in the form of poly-crystal. The poly rods are then shaped into chunks of appropriate size for CZ crystal growth systems. The rod ends and the dust that is collected at the bottom of the reactor can be used in powder form for other purposes. Once the CZ or FZ ingot is grown, the ingot is trimmed and flattened and finally wafers are cut by slicing, and the edges are chipped. The wafer shaping process from an ingot results in considerable amount of silicon loss in the form of powder which is known as kerf loss.

Silicon powder form MG-Si, poly rod ends, kerf loss, and especially reactor dust is optically fused by an arc lamp into clusters of a certain size with a high power flash that melts and fuses the powder to the clusters forms of Figure 3.1 in less than 1 second. The clusters fused form electronic grade kerf loss and reactor dust will be of the highest quality whereas the MG-Si produces the lowest quality due to the high impurity level. Since OFP is obtained from a melt,

grains of the crystalline phase start to form. Yet due to rapid solidification, OFP clusters are expected to form a poly-crystalline structure.

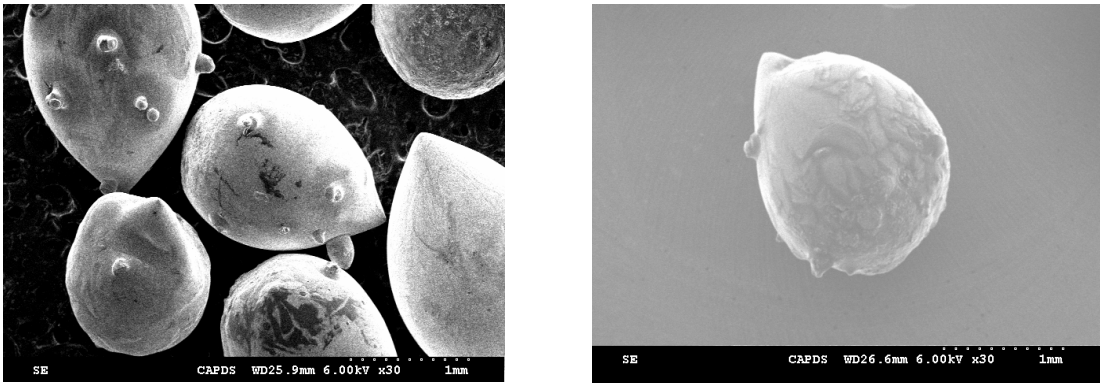

Figure 3.1: Optically fused powder (OFP) clusters from melting and solidifying reactor dust in less than 1 second using high power arc lamp.

3.1.2 Granular Silicon

If the MG-Si is turned into silane form (SiH_4), the distilled gas is decomposed in a fluidized bed with silicon seeds injected, and silicon deposits on the seed to form granular silicon bead. The seeds are usually obtained by grinding SG-Si and might be contaminated with impurities by the grinding machine. Thus the granular Si product is of the same quality of or inferior to the poly rod ends depending on the seeds purity. The granulars that form in this manner vary in size as in Figure 3.2. Since the deposition of silicon from silane takes place at elevated temperature (around 700^{o}C) in the fluidized bed reactor (similar to poly rod formation), granulars form poly-crystalline beads.

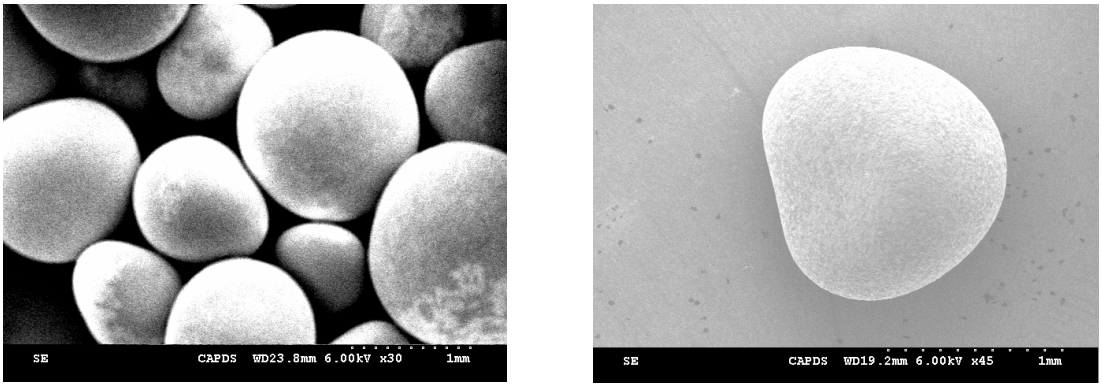

Figure 3.2: Granular Si beads used as the start material for fabrication of silicon spheres; beads are formed in fluidized bed reactor for poly-silicon feedstock process.

3.1.3 Spherical Silicon with Radial Bulk Properties

Once OFP clusters or granular beads are formed, they undergo a melt and recrystallization step at around 1400^{o}C to form round spherical crystals of high quality. Once the clusters or beads are spheroidized, the melting may be repeated to enhance the quality, and every time is preceded by an oxide formation at the surface to prevent the spheres from sticking to each other, and is followed by an oxide removal etch step which also removes the impurities segregated to the surface of the sphere. The final result is spheres with relatively fine shapes and smooth surfaces (Figure 3.3).

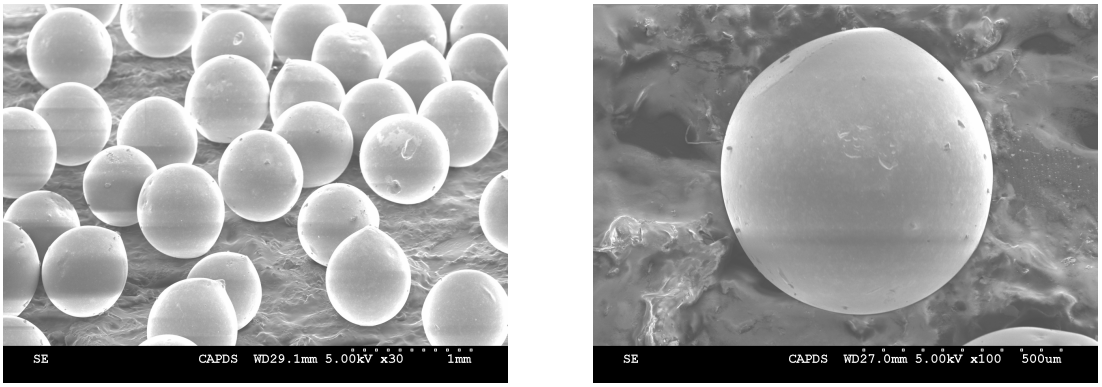

Figure 3.3: Crystalline silicon spheres formed from melting and crystallization of OFP clusters or granular beads.

Since the sphere is thoroughly melted and solidification takes place in a controlled ambient with the spherical surface exposed, the crystallization proceeds in the radial direction, i.e. the solid-melt interface moves radially. Therefore, the crystal structure formation, impurity segregation, thermal stress, and defect formation processes follow a radial profile and the produced spheres are expected to have radial distribution of bulk material properties. Accessing the bulk of spherical silicon is almost impossible from the surface. In contrast to a planar wafer where silicon atoms can be etched (or ion beam sputtered as in secondary mass ion spectroscopy) normal to the wafer surface to access the lower layers for depth profiling, spheres may not be patterned (by etching) or sputtered accurately in the radial direction for depth profiling of the bulk. To gain access to the inner layers in a sphere, two approaches are possible: etching the sphere to smaller radii, or lapping or polishing the sphere to half.

For the characterization experiments, when access to different radii inside the bulk was required, the spheres were etched chemically from the surface using an anisotropic etchant (nitric acid, hydrofluoric acid, acetic acid). A 4:1:1 ratio of the three acids was used for fast etches, and water dilution or acetic acid dilution was used when lower etch rates were desired. Since the etch rate varies depending on the material properties of the spheres, the size of the resulting spheres were measured using optical (and also electron) microscope after etching. Samples of different radii prepared with this method were used for defect etching, secondary ion mass spectroscopy (SIMS), and photoconductivity decay measurements.

On the other hand, in most characterization techniques, for both material properties and electronic properties, a planar surface of the specimen is preferred. By mechanically polishing the spheres to half, we made hemispheres, the equatorial plane of which can be treated as a planar surface for measurement purposes; a lateral scan on the surface of this plane provides information about different radii inside the spherical bulk. This was achieved by embedding the spheres (and OFP

clusters and granular beads) in a plastic or epoxy-like mold, and then thinning the mold to a certain level so that the spheres are polished to half. The final result is schematically shown in Figure 3.4. Specimens of such a structure will be referred to as hemispheres in this thesis.

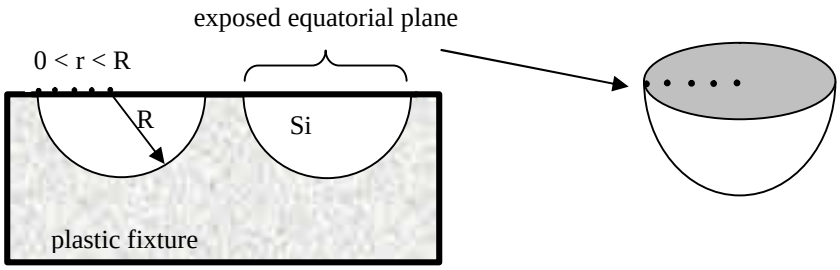

Figure 3.4: Hemispheres polished from Si spheres for the purpose of access to bulk material of spherical silicon for material characterization; the exposed equatorial plane fully represents the spherical bulk.

For hemisphere sample preparation, the spheres embedded in (plastic or epoxy) molds were first grinded close to half using sandpapers of grit numbers equivalent to 50 μm and 30 μm particle sizes. The resulting surfaces were then polished using diamond paste with particle size of 3 μm. The final step was a chemo-mechanical polish using suspension slurry equivalent to 0.05 μm size. The final chemical finish of the hemispheres ensures a clean surface free of any contaminations induced by the polishing process. Hemispheres prepared with this method were used for Raman spectroscopy, crystal characterization using electron diffraction, defect etching, and SIMS analysis.

3.2 Crystallinity of Spherical Silicon

The most basic property in a semiconductor material is the issue of crystallinity. The materials used for the production of silicon spheres, OFP or granular silicon, are in general expected to be in a poly-crystalline form as they are either obtained from melt, or from gas phase deposition at elevated temperature. Raman spectroscopy on polished OFP and granular samples confirms this.

In Figure 3.5 the spectra of OFP and granular samples show a clear contrast to the spectra of an amorphous silicon film and a solid phase crystallized silicon film. The slight difference between the OFP and granular spectra and that of a perfect crystal sample (standard silicon wafer) is an indication of the deviation from the perfect crystalline form in OFP clusters and more considerably in granular beads, which seem to be more of poly-crystalline form.

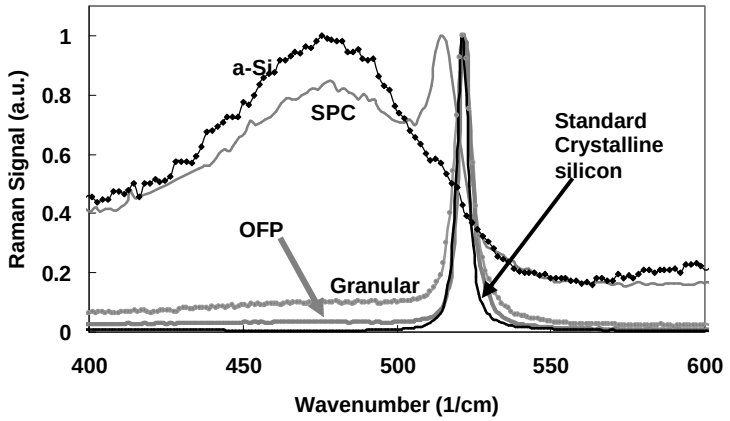

Figure 3.5: Raman Spectra of OFP clusters and Granular beads, compared to a perfect silicon crystal; also are given the spectra of amorphous silicon deposited at 250 ^{o}C and solid phase crystallized (SPC) amorphous silicon annealed at 750 ^{o}C, measured for comparison.

Although the OFP and granulars are found to be different from the perfect crystal, Raman spectroscopy shows that the melt and recrystallization step for the formation of sphere effectively enhances the crystallinity. Figure 3.6 shows the spectra for a granular bead and an OFP cluster compared to the spectra of the corresponding spheres crystallized from them. The Raman spectra approach that of a perfect crystal after spheres are formed from the granular and OFP forms.

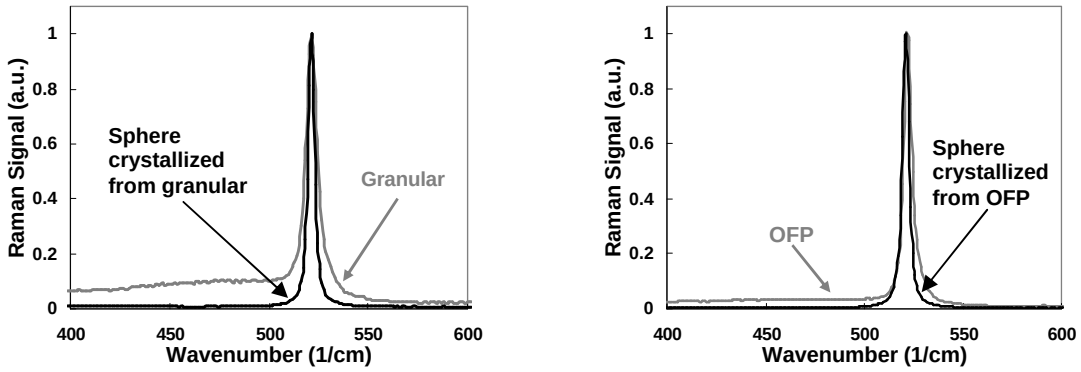

Figure 3.6: Raman spectra of (a) a granular bead and a sphere after recrystallization form granular bead (b) an OFP cluster and a sphere after recrystallization form OFP cluster.

Scanning the surface of the equatorial plane of hemisphere specimen produces the same Raman spectrum as a Czochralski crystal all over the spherical bulk. Yet the accuracy of Raman spectroscopy is insufficient to conclude spheres are single crystal structures. Raman spectrum loses sensitivity in crystal structure with larger grain sizes, and will not be able to solidly confirm the single- versus multi- or large grain poly-crystallinity.

An alternative approach to investigate crystallinity would be electron diffraction. Electron beam can be focused to small sizes, and it is possible to acquire the diffraction pattern on the surface of a polished hemisphere at a certain spot. We performed electron diffraction study on crystallized spheres as well as OFP and granular samples through Orientation Imaging Microscopy (OIM^{TM}). OIM is a tool attached to scanning electron microscope (SEM); the electron beam of the SEM is directed towards the sample and the electron back scattered pattern is detected by a special detector. OIM generates diagrams with patterns of intersecting lines, each of which represents a certain crystallographic orientation as in Figure 3.7.

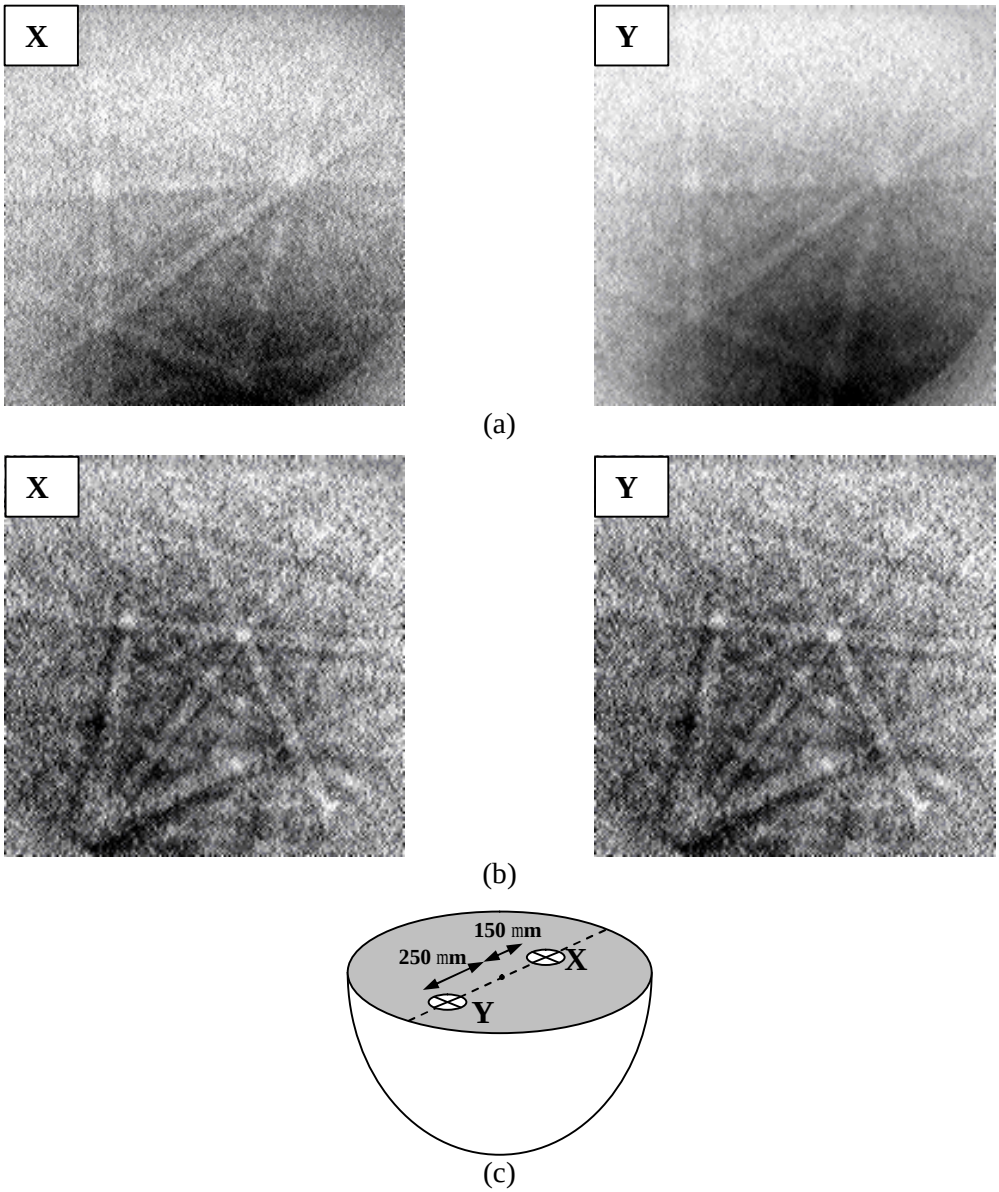

Figure 3.7: OIM™ patterns of two samples a and b at two different spots X and Y on the equatorial plane as chosen in c.

Electron diffraction patterns of two different hemispheres (from different sets) across the surface of the equatorial plane obtained using OIM are shown in Figure 3.7. The sample spots were approximately 400 μm distant across the equatorial plane as shown in Figure 3.7(c). The lines and poles are identical in the patterns of different spots in both samples, implying that the electron

beam was diffracted by the same crystallographic planes at two different spots, and the same crystal structure exists in the region including the two spots.

Based on the experimental results of characterization of crystallinity, the spheres resulting from spheroidization and crystallization generally adopt a single-crystalline form. This is further confirmed by defect etching as will be discussed in Section 3.5 (it will also be seen that double-crystals may also form). Thus, general optical and electronic properties of the spherical silicon are expected to resemble those of crystalline silicon; many electronic and optical properties (such as optical absorption) and semiconducting processes (electronic defect level formation and recombination processes) will be thus identical to the known phenomena of Silicon.

The characterization can also be utilized as a process monitor for the effectiveness of recrystallization progression during melt and solidification of the spheres, and will be instrumental in optimization of sphere growth process.

3.3 Metallic Impurities in Spherical Silicon

One of the main issues in the spherical solar cell is impurity content of silicon. The metallurgical grade (MG) and the off-spec semiconductor grade (SG) silicon feed stock for the technology of spherical silicon may contain large quantities of impurities such as Fe, Ca, Al, Ti, Cu, Cr, and some other heavy metals. Such elements create deep electronic levels in the bandgap leading to poor minority carrier lifetime in the spherical silicon bulk.

During the formation of silicon spheres, these impurities are uniformly distributed all over the initial melt and then redistributed in the solid phase through segregation from solid to melt as the melt-solid interface moves radially during solidification. Repeating melt and recrystallization steps can further influence the redistribution of impurities in the spherical bulk; the process is

often followed by an etch step to remove a considerable portion of impurities that have segregated to the surface. Therefore, the melt and etch processes lead to purification of the silicon material.

3.3.1 Impurity Distribution Modeling in Spheres

Based on a previously reported model of impurity segregation in spheres [32], the impurities are believed to redistribute radially after a melt and recrystallization process with a large portion of atoms segregating and piling up close to the surface of the sphere. This accumulated population of impurity atoms is then eliminated by an etching step that removes an onion skin from around the sphere surface. After a single melt and recrystallization of spheres, the concentration of a certain impurity at radius r is expected to follow [32]:

$$C = C_0 k\left[1-\left(\frac{r}{R}\right)^3\right]^{(k-1)} \tag{3.1}$$

where C_0 and C are the concentration prior to and after purification, k is the corrected segregation factor and R is the sphere radius. Figure 3.8 shows the normalized impurity distribution in the radial direction for several elements. It is predicted by this model that a considerable fraction of the impurities is eliminated by removing a thin outer layer of the sphere after melt and recrystallization step as depicted in Figure 3.8.

More purification steps may be required for lower quality feedstock (e.g. MG-Si) [33] when metallic impurity atoms exist in high concentration and contribute to trap assisted recombination. Moreover, the redistribution of dopant atoms such as B and P are important in determining the bulk resistivity. The weak segregation of boron is beneficial in the fabrication of p-type spheres from boron doped powder or feedstock, whereas phosphorous doping level at the center of a sphere reduces to 35% of the initial doping level after a single recrystallization step. Thus, if fabrication of n-type spheres is desired, the start material must be over-doped with phosphorous.

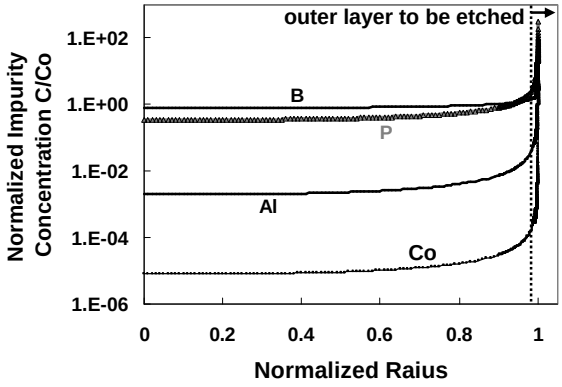

Figure 3.8: Impurity concentration as a function of radius inside spherical Si after one step of melt and segregation; modeled after [32]; impurities piled up at the surface are removed by etching.

3.3.2 Impurity Concentration Characterization in Spheres

It is important to characterize the impurity level in spherical silicon to ensure high material quality at the vicinity of the metallurgical junction where carrier collection takes place through the space charge region. It is also crucial to determine the spatial distribution of impurities. For this purpose, a depth profiling in the spherical bulk is required to extract the radial distribution of the impurities. The technique that makes depth profiling possible is secondary ion mass spectroscopy (SIMS), in which, by an ion beam, the atoms are sputtered from the surface and detected in the form of secondary ions that are separated by magnetic field.

SIMS measurements were performed both on hemispheres and spheres chemically etched to different radii. We collected ion counts for elements that are frequently detected in low grade silicon. We found negligible traces of Ca, V, Cr, Mn, Zr and small amounts of Cu, Fe, and Ti in the start materials, i.e. granular beads and OFP clusters. Depending on the feedstock, these values might change, yet it can be concluded as is shown in Figure 3.9 that the low concentration of these metals are even lower in the crystallized sphere, which is a direct outcome of the impurity behavior shown in Figure 3.8. Aluminum and cobalt are detected in large concentrations in the

spheres and appear to be the dominant impurities. Aluminum creates a shallow level in silicon close to the valence band, and its atomic size is very close to that of silicon, and thus is not expected to affect the electronic properties through deep level traps or structural defects in substitutional sites. However, interstitial Al atom will definitely affect the electronic energy levels in the lattice. Cobalt on the other hand is among the elements that create the deepest levels in silicon with a 0.53 eV acceptor like energy state (just above mid-gap), and Co atoms will be lifetime killer sites in the silicon electronic structure (similar to the potential effect of Fe, Cu, Au, Zn, and Mn which were not detected in considerable quantities).

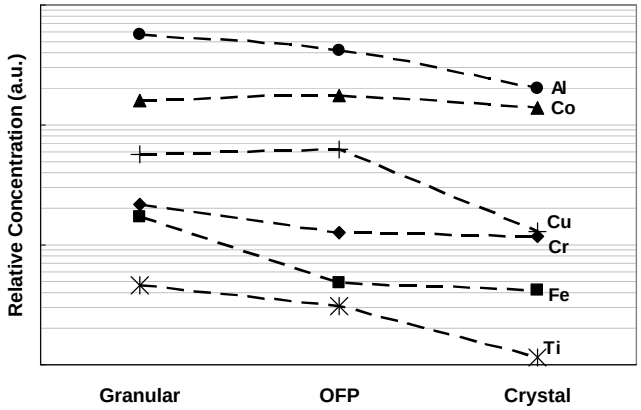

Figure 3.9: Relative impurity concentration from SIMS analysis in OFP, granular, and crystallized silicon sphere.

SIMS results on several stacks of spheres from different steps during the fabrication show that while cobalt has an approximately constant distribution in all cases, aluminum behaves anomalously in different cases (Figure 3.10). In crystallized spheres, aluminum is increasing from center to surface as is predicted by the model in the previous subsection. However, the aluminum shows a rise from surface to center in the spheres after denuding. The denuding is conducted as a solid state process at 1200 ^{o}C. The denuding time for the samples in this experiment was 33 hours, for which the diffusion of Al atoms is around 10 μm. Considering the times for ramp-up,

ramp-down, and annealing at 1000 ^{o}C, aluminum is not expected to show a drastic change in its radial distribution, and the redistribution might be due to accelerated gettering towards the oxide layer that forms at the surface.

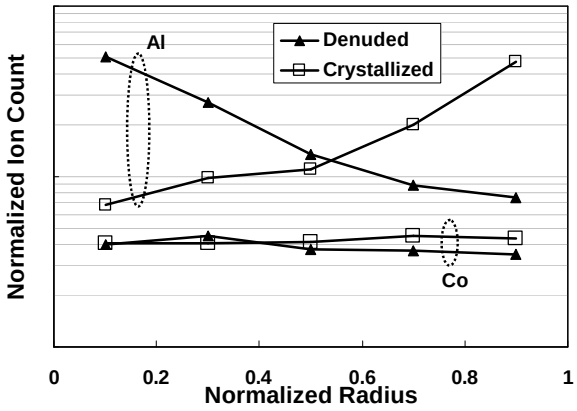

Figure 3.10: SIMS analysis results for Al and Co in silicon spheres at different radii after crystallization and after denuding steps.

To further probe the effect of denuding on Al profile in the spheres, we performed SIMS analysis on hemispheres. For SIMS on hemispheres, the spot size of the ion beam was set to minimum for which the sputtered area for is about 60 μm wide. The crystallized spheres are usually larger in size and a thick layer was etched from the outer surface to achieve spheres of sizes comparable to denude samples. We were able to take five readings across the sample for samples with a radius of about 350 μm. Figure 3.11 shows the results on the crystallized spheres before and after denuding. While this set of crystallized spheres show a relatively constant concentration, which very well agrees with the model results considering the thick removed layer, the Al profile after denuding again shows a drastic drop from center to surface.

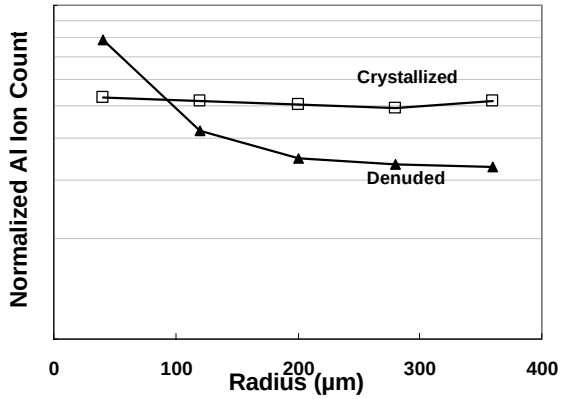

Figure 3.11: SIMS analysis on hemispheres for radial distribution; results of aluminum ion counts before and after denuding.

3.4 Oxygen Content and Denuding in Spherical Silicon

One impurity of great importance in the spherical Si crystal is oxygen. Oxygen remains with a high concentration inside the sphere even after purification steps. During melt and recrystallization, the outer protecting oxide layer does not allow oxygen effusion to proceed effectively. Controlling the oxygen content and denuding is important as the interstitial oxygen atoms are basically lattice imperfections as well as substitutional atoms with the huge size mismatch when compared to silicon. Moreover, oxygen creates an energy level very close to the mid-gap and can act as a lifetime killer in silicon lattice. On the other hand, oxygen sites inside the spherical bulk can act as sites of intrinsic gettering and absorb metallic impurities [36].

Figure 3.12 shows the radial profile of oxygen extracted from SIMS analysis on hemispheres. The profiles are normalized to only account for the spatial distribution and exclude the possible difference in oxygen content of the start material of the two sets. The faster decrease in the oxygen content of the denuded sphere from center towards surface shows the effectiveness of the denuding step. The oxygen diffusion length for 24~48 hours of denuding at 1200 ^{o}C (the typical

denuding process conditions) is around 59~83 μm. Thus it is expected to form denude zones of around 50~100 μm in a typical denuding step. This however depends on the definition of the denuded zone depth in terms of relative or absolute oxygen content. In Chapter 4, we will define the denuded zone in terms of radial variations of electronic properties relative to subsurface region (where the quality is best).

In short, the denuding steps allow oxygen effuse from the subsurface region of the spheres while the following lower temperature processes can be employed to getter metals away from the subsurface region to the remaining oxygen sites close to the center. This lead to a higher quality denuded zone with regards to carrier lifetime, and a core with somewhat inferior quality as we approach the central regions of a sphere.

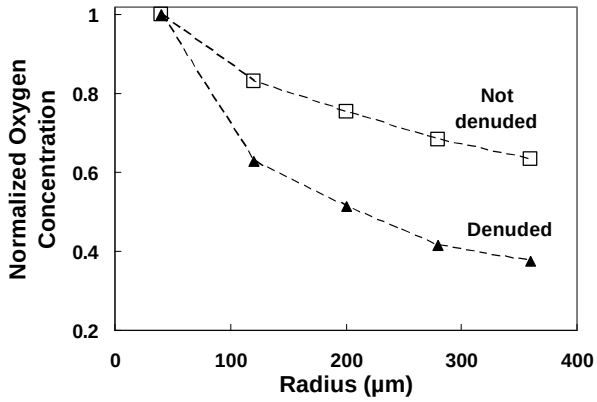

Figure 3.12: Radial profile of oxygen content for a denuded sample vs. a not-denuded sample.

3.5 Defect Characterization and Control in Silicon Spheres

In addition to common impurities and oxygen that were mentioned in the previous sections, structural (lattice) defects in the crystal influence material parameters, in specific, minority carrier lifetime. The special crystal growth mechanism of spheres and the following high temperature steps such as denuding, annealing, and diffusion may induce or cure defects of different kinds.

Thus, defect characterization provides a strong tool to understand the electronic behavior of the material which directly influences device performance. We used a Dash defect etching to characterize the defect creation/anneal during different process. Dash solution is in fact a slow silicon etching mixture of 1:3:10 hydrofluoric, nitric, and acetic acids, which mainly attacks the crystallographically defective sites. The delineation of defects was performed by 1~2 hours of defect etching in Dash.

3.5.1 Defect Etching of OFP Clusters, Granular Beads, and Spheres

Defect delineation on the OFP and granular samples further prove the effectiveness of the crystallization process in converting the poly- and multi- crystal structures of the pre-spheroidization form into crystalline structure.

Figure 3.13 shows the SEM micrographs of different samples after a 90 minute defect etch in Dash solution: a granular bead, an OFP cluster, and two recrystallized spheres from granular beads and OFP clusters. The granular bead obviously consists of very small size grains and is of a poly-crystal form, whereas the OFP sample proves to consist of larger grains with the grain boundaries delineated by the defect etchant. Apparently, some of the grains happen to be more defective, and the pointed tip is definitely the most defective spot of the cluster.

Once crystallized, the produced spheres show improved crystallinity. The sphere recrystallized from the granular bead in Figure 3.13 happens to have a double-crystalline structure. Although this is not a general case, but it happens for some of the spheres. The spheres recrystallized from OFP clusters show better crystallinity in general; in very few of these spheres delineated boundaries for double grains were observed. However, the defect density of the OFP recrystallized sphere in Figure 3.13 is higher compared to the granular recrystallized. Since different recrystallization recipes were used for the two processes, no conclusion can be obtained

on the comparison of actual defect densities in OFP and granular recrystallized spheres; in fact we observed different results on different sets of spheres from these two origins. Yet, it can be conclusively observed that the recrystallization of the OFP clusters and granular beads results mainly in single-crystal (or in some cases double-crystal) structures with lower defect densities of mostly point defect nature.

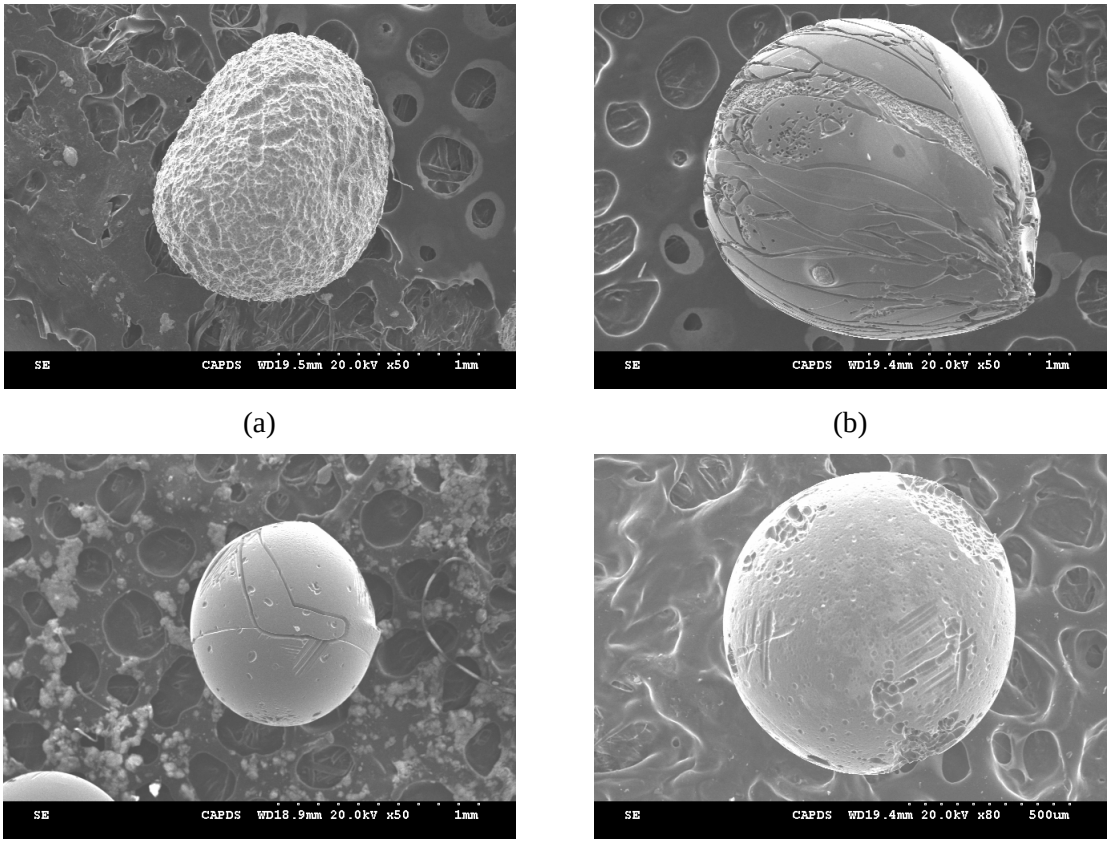

Figure 3.13: SEM micrographs of 90 minutes Dash defect etched (a) granular bead (b) OFP cluster (c) sphere crystallized from granular (d) sphere crystallized from OFP.

3.5.2 Defect Characterization of Recrystallized Spheres

After the spheres are recrystallized from OFP clusters and granular beads, the crystallographic defects are mainly due to imperfections that include impurity atom sites (including oxygen) as

well as lattice point defects and other grown-in defects. We performed defect etching on several stacks of the recrystallized spheres after the protective oxide was removed. Since the protective oxide induces a great amount of defects, the spheres must be etched to remove at least a few micrometers to eliminate the defects originating from surface.

Figure 3.14 shows the delineated defects in a stack of spheres recrystallized from granular beads. The spheres are first etched as mentioned in Section 3.1.3 to the desired radius and then defect etched in Dash solution for 60 minutes. Apparently, less structural defects exist closer to the center. Similar results were observed on several stacks of spheres from granulars.

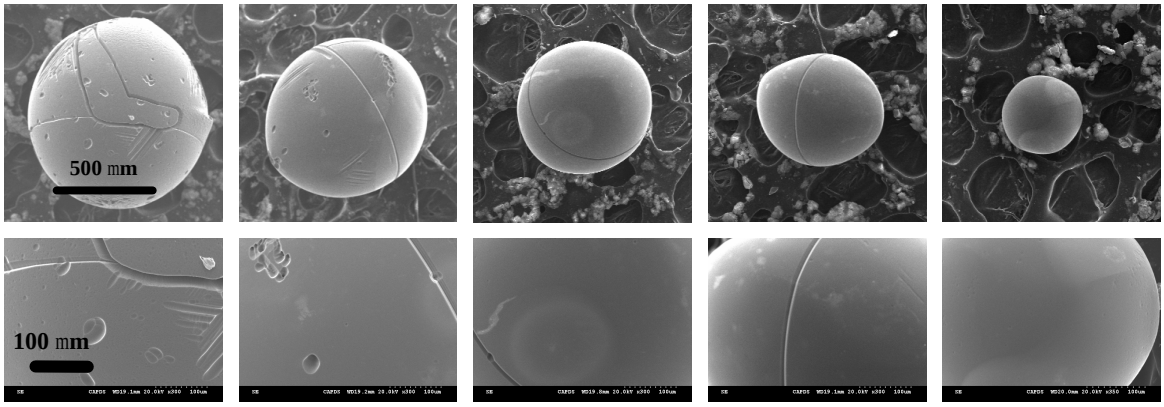

Figure 3.14: Defects in spheres recrystallized from granular beads at different radii delineated by Dash etch, with a decreasing density closer to the center.

Figure 3.15 shows the optical microscope images of defect delineated spheres recrystallized from OFP clusters after 80 minutes of defect etching. Although these spheres were defect etched for a longer time than the spheres of Figure 3.14 and thus show higher defect densities in general, yet the defects again appear to exist in lower densities at the central regions of these spheres as well. The grown-in defects during the crystallization are believed to be mainly due to the stress induced to the lattice at the melt-solid interface [6]. From the results of delineation of spheres, it is concluded that the defects are distributed at higher densities closer to the surface after the sphere formation.

Figure 3.15: Defects in spheres recrystallized from OFP at different radii (decreasing from left to right similar to Figure 3.14) delineated by Dash etch.

3.5.3 Defect Monitoring of Denuded, Annealed, and Diffused Spheres

While the recrystallized spheres appear to have relatively low grown-in defects in spite of the high oxygen content (which electronically degrades the bulk), defect etching of the spheres from different steps during the device fabrication show several phases of creation and curing of process induced defects. The final target is lowest defect density at the end of the process line.

Figure 3.16 shows the optical micrographs of delineated defects in a set of denuded spheres with different radii. The long high temperature (1200 ^{o}C) denuding step apparently creates a huge number of defects inside the bulk. It is also observed that a higher density of defects is created closer to the center. In general, the electronic quality of the spheres somewhat degrades during the denuding process due to substantial creation of defects. This will be further discussed in Chapter 4 where minority carrier lifetime is used to monitor electronic quality of the spheres during the fabrication process flow.

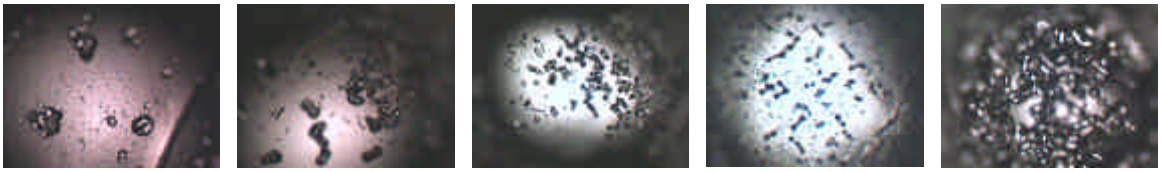

Figure 3.16: Defects in spheres after the denuding process at different radii (decreasing from left to right).

While denuding induces a large density of crystallographic defects, the following high temperature annealing processes effectively cure most of the induced defects. Figure 3.17 depicts

the delineated defects on spheres annealed after denuding. While etching down the spheres, the defect density seems to drastically rise after a certain radius. This high density of defects in the inner core of the spheres is attributed to the precipitation of oxygen atoms in the inner shells of the sphere. While the subsurface region is evacuated from oxygen atoms during the denuding step, a highly defective core is observed in all the spheres very close to the center. This core region in practice starts where the denuded zone ends, and extends towards the lower quality central regions with a quickly degrading crystalline structure (Figure 3.18).

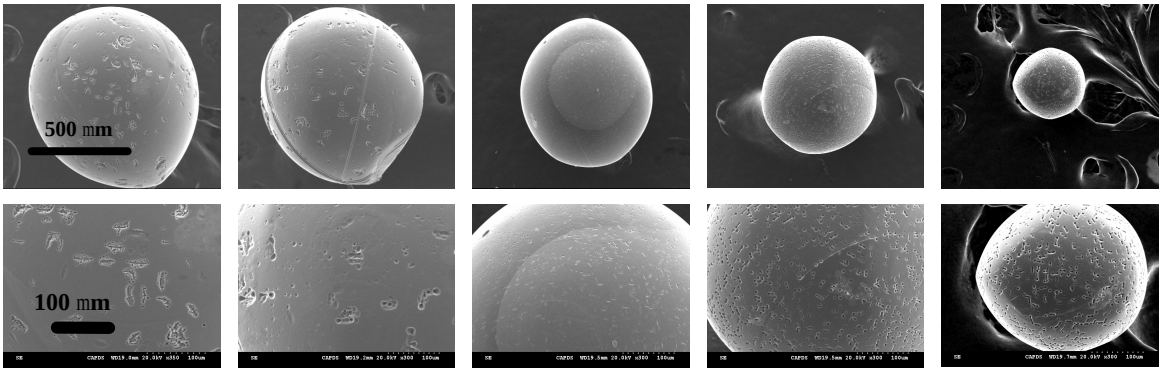

Figure 3.17: Defect annealing in denuded spheres after one step of annealing.

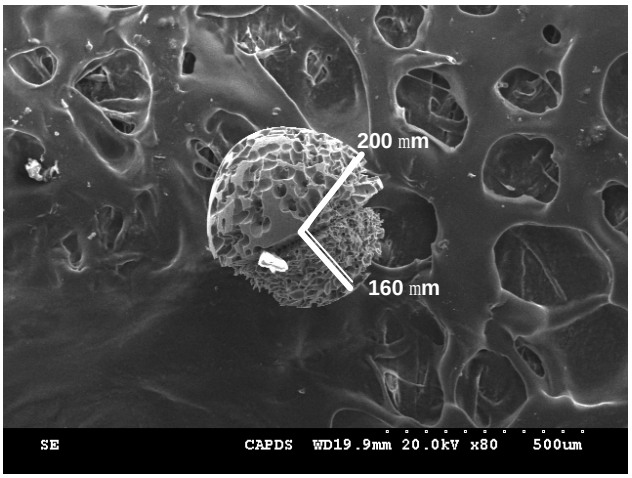

Figure 3.18: A denuded sample (with original radius of around 400 micron) etched approximately to half and then defect etched for an additional 120 minutes; highly defective core exists close to the center.

The diffusion process with a maximum temperature of 950 ^{o}C and a controlled cool down acts as an additional anneal and results in highest quality spheres. After the diffusion, the defect density at the immediate subsurface region is high due to the introduction of large number of phosphorous atoms (Figure 3.19). Yet the defect density is low for the subsurface region beyond the diffused n-type shell. The extent of this high quality bulk inside the sphere is determined by the denuding and annealing processes. At a certain depth, the quality degrades due to structural defects and oxygen precipitates. However, these spheres possess superior electronic properties as will be seen in Chapter 4, and are appropriate for application as a PV device.

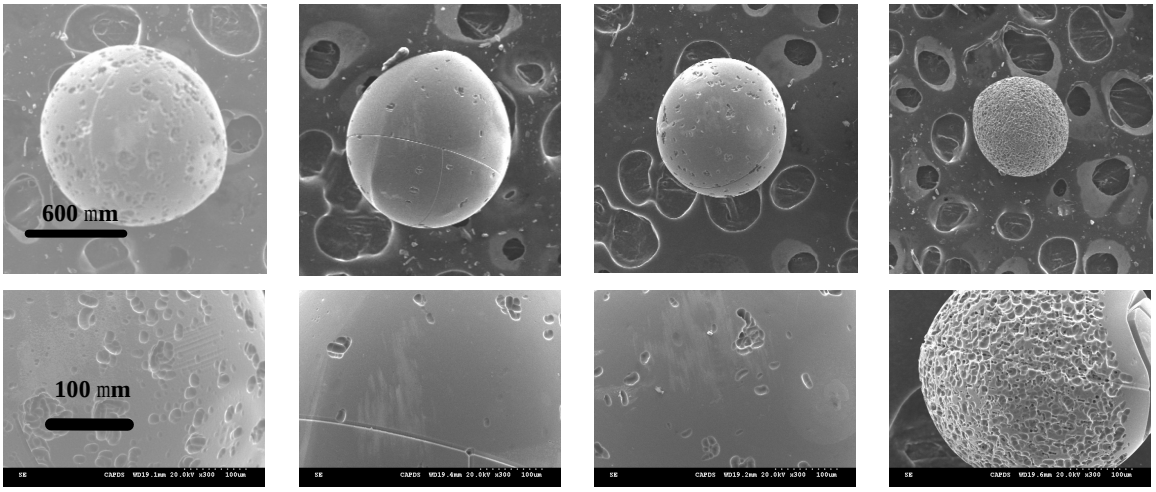

Figure 3.19: Defect delineation in finished spherical pn junctions after diffusion; the not-etched sphere (on the left) has a high defect density due to the defects created during P diffusion.

3.6 Summary

The materials characterization of the silicon spheres demonstrates that Si crystals result from the spheroidization of granular beads (produced in poly-crystal form in fluidized bed reactors) or optically fused powder clusters (from metallurgical grade Si, reactor dust, kerf loss, etc). According to electron diffraction patterns, the spheres prove to consist of single (or sometimes double) grain structures. Depending on the quality of the start material, different impurities may

be found in the fused sphere. Oxygen, Aluminum, and Cobalt are among the impurities that are found in high concentrations based on SIMS analysis. Moreover, structural (lattice) defects inherently exist in the silicon spheres as grow-in defects, i.e. the lattice defects are created during the crystal growth. The evolution of defects during sphere formation and device processing steps was monitored using defect etching. The final pn junction spheres seem to enjoy from a high quality bulk in the subsurface region (denuded zone) while the inner core is still defective.

The results of the characterization of silicon spheres provide information about the structure of the material and will help in identifying the optically and electronically important phenomenon in the bulk, and are useful in developing a basis for the interpretation of electronic measurements in spheres as we will see in the next chapter. These techniques can also be employed for the characterization of the produced spheres, as well as the monitoring of the process steps.

Our initial results of other approaches show that further characterizations can be employed which include bulk microdefect characterization using scanning (confocal) infrared microscopy (SIRM) of the hemispheres, electronic defect mapping using photoluminescence (PL) microscopy, and crystallinity by quantified micro-focused x-ray diffraction (μ-XRD). Positron beam annihilation (PAS), although capable of depth profiling of electronic defects, was found unsuccessful due to unavailability of micro-focused positron beam; the beam covers an area consisting of several spheres, and the background material exposed through the geometrically poor sphere packing.

Chapter 4

Development of Novel Methodology for Electronic Characterization of Spherical Silicon

Structural and material properties were investigated in the previous chapter; these properties determine the electronic properties of silicon spheres. The device performance is mainly influenced by electronic properties of the material. Thus, to more effectively predict the device efficiency and optimize its performance, it is crucial to characterize the electronic properties of spherical silicon based on the previously determined material structure and characteristics.

For silicon photovoltaic devices, which are known as bulk devices due to the photon absorption pattern that is distributed deep in the bulk, the diffusion length is the most important material parameter affecting the efficiency. Diffusion length is determined by minority carrier lifetime and diffusion coefficient. Since the diffusion coefficient is proportional to carrier mobility and is less sensitive to structural defects, impurities, and other imperfections as long as a crystalline structure is concerned, the carrier lifetime plays the most important role in the performance of the device. Depending on the crystal growth technology, lifetime values of 1~10 μs are usually achievable on multi-crystalline silicon, 30~100 μs on Czochralski, and up to milliseconds on float zone, which accounts for the typical efficiency variations of below 14% to above 20% on the cells fabricated using these materials. Moreover, the high sensitivity of carrier lifetime to lattice imperfections

and material quality prompts it as a suitable choice for process monitoring during the fabrication process flow.

In Section 4.1, a methodology is developed to model and interpret minority carrier lifetime in the spherical silicon measured using microwave photoconductivity decay. The effect and interpretation of bulk and surface electronic properties are discussed. The developed methodology is employed in Section 4.2 to characterize the quality of interface and bulk, as well as defects, their presence, creation and evolution. The defect monitoring is shown to be useful for process development and monitoring. A more accurate approach is employed in Section 4.3 to characterize carrier lifetime in the spheres which is capable of extracting the spatial profile of lifetime and also the depth of denuded zone under the sphere surface. These results will be used for device modeling and simulation purposes as will be seen in Chapter 5.

4.1 Minority Carrier Lifetime in Spherical Silicon

While minority carrier lifetime is the most important factor in the performance of a photovoltaic device, most standard lifetime measurement techniques are not directly applicable to spheres. In this section, a model is proposed to reliably measure and extract minority carrier lifetime in spherical silicon using photoconductivity decay (PCD). The results of measurement will be used in the following sections of this chapter to evaluate the quality of the spherical material, as well as a process monitor for various fabrication steps during the material growth and device processing.

4.1.1 Photoconductivity Decay

Microwave photoconductivity decay (μ-PCD) measurement [37] is commonly used to characterize bulk and interface recombination rates. In this technique, the sample is exposed to an initial laser pulse which generates excess carriers in the semiconductor sample; the excess carriers

recombine after the laser power is turned off leading to an exponential decay of conductivity over time. Microwave reflection from the semiconductor sample is proportional to the conductivity; an antenna close to the sample is constantly emitting a microwave signal and the reflected microwave power is monitored to record the decay in photoconductivity.

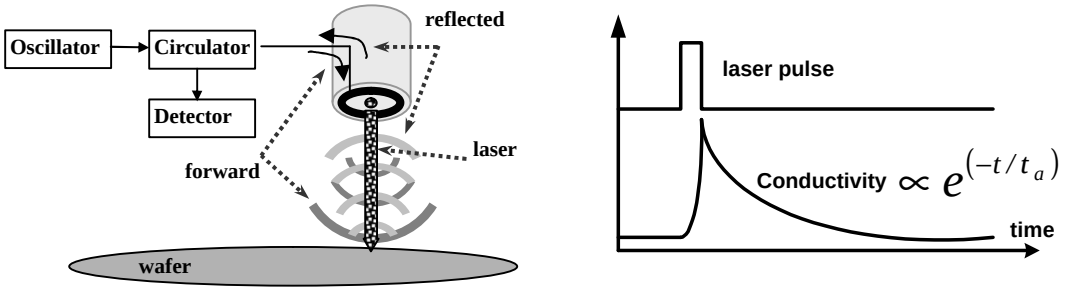

Figure 4.1: Microwave photoconductivity decay measurement of minority carrier lifetime (a) the measurement diagram (b) laser pulse and PCD signal.

The decay in conductivity detected through microwave reflection includes the effects of bulk and surface recombination rates. The bulk recombination rate is represented by bulk lifetime τ_b and the surface recombination rate is known as surface recombination velocity (SRV). There are several modes of decay, each of which combines the bulk lifetime with surface recombination lifetime $\tau_{s\text{-}i}$ (i=1, 2 ...). In a semiconductor wafer, the majority of these modes fade away very quickly, and the first mode lasts longer and generates the single exponential decay with an "effective" or an "apparent" lifetime τ_a [38]. Thus the surface recombination effectively contributes through the first mode surface lifetime $\tau_{s\text{-}1}$ (principle mode) also known in the literature as τ_s for simplicity. The PCD measured "apparent" lifetime is thus interpreted as:

$$\frac{1}{t_a} = \frac{1}{t_b} + \frac{1}{t_{s-1}} \tag{4.1}$$

$\tau_{s\text{-}1}$ is an implicit function of SRV at the back and front surfaces of the wafer [37]. The relation is derived from the solution to the charge kinetics after the laser excitation (continuity equation) with the appropriate boundary conditions. Approximations exist for the cases of well-passivated

and poorly-passivated surfaces of one-dimensional samples (wafers) to explicitly relate τ_{s-1} to SRV [39]. Yet in general, the apparent lifetime extracted from PCD measurement can be a complicated function of bulk lifetime and surface recombination velocities, as well as laser excitation wavelength and geometry of the sample.

4.1.2 Charge Kinetics of Excess Minority Carriers in Sphere

PCD of silicon spheres has been previously treated using a classical approach [40] replicated from measurements of planar wafers. While giving an estimate of the materials quality, the technique may lead to inaccurate results. By considering the geometry, the measured decay signals can be interpreted to produce more accurate and at the same time repeatable and reproducible results.

Due to different geometry, charge kinetics inside a spherical semiconductor in response to an initial laser excitation is different from the one-dimensional kinetics that occurs in conventional PCD measurements on planar wafers. Not only the monitored decay consists of more exponential decay terms that last longer, the relation between SRV and τ_s (of the principal decay) may change. By considering the fact that charge continuity holds in a multi-dimensional form in the case of a sphere, we derive the different decays that are present in the charge kinetics of a sphere in order to accurately interpret the PCD lifetime measurements in Si spheres.

In PCD the initial laser excitation creates excess minority carriers (e.g. excess electrons n in p-type material) followed by charge recombination. The main focus here is on charge kinetics in absence of optical generation and the effect of generation is only the initial condition of the excess carrier distribution. We will show in more details in Chapter 5 that in the case of light exposure normal to the horizontal plane (Figure 4.2), azimuthal (ϕ-direction) symmetry exists and the system reduces to two dimensions of radial (r) and zenith angle (θ) variations.

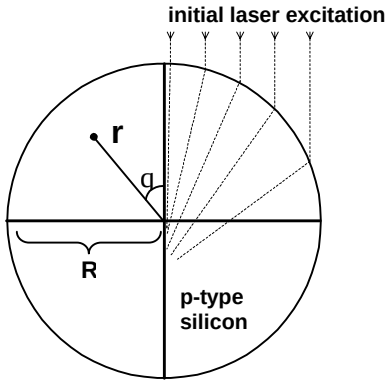

Figure 4.2: A silicon sphere under initial laser excitation; the three dimensional system reduces to a two-dimensional circle due to symmetry; details of optics in Chapter 5.

The charge continuity equation in two dimensions can be written as:

$$\frac{\partial n}{\partial t} = D\left[\frac{1}{r^2}\frac{\partial}{\partial r}\left(r^2\frac{\partial n}{\partial r}\right)+\frac{1}{r^2\sin q}\frac{\partial}{\partial q}\left(\sin q\frac{\partial n}{\partial q}\right)\right]-\frac{n}{t_{eq}} \tag{4.2}$$

with n as the excess minority carriers and t as time. τ_{eq} is the equivalent bulk lifetime of a sphere and D is electron diffusion coefficient. Equation (4.2) is separable and the solution is written as,

$$n = \sum_i \sum_m \Gamma_{i,m}\, exp\left[-\left(\frac{1}{t_{eq}}+D\frac{l_{i,m}^2}{R^2}\right)t\right] j_m\left(l_{i,m}\frac{r}{R}\right)P_m(\cos q) \tag{4.3}$$

where j_m and P_m are spherical Bessel functions of the first kind and Legendre polynomials of order m, R is the radius of the sphere. Decay "constants" $\lambda_{i,m}$ and decay "coefficients" $\Gamma_{i,m}$ are to be determined using boundary and initial conditions. Three boundary conditions of finite carrier density at the center and along zenith axes (r = 0 and $\theta = 0, \pi$) actually eliminate spherical Bessel and Legendre functions of the second kind. The fourth boundary condition is defined at the surface of the sphere and includes the surface recombination velocity *S* at this boundary:

$$-D\left.\frac{\partial n}{\partial r}\right|_{r=R} = s\cdot n\big|_{r=R} \tag{4.4}$$

Substituting the excess carrier distribution from (4.3) into (4.4) leads to a separate equation for every order of m.

$$\frac{Dl}{SR} + \frac{j_m(l)}{j_m'(l)} = 0 \qquad ; \qquad m = 0,1,2,... \tag{4.5}$$

The first term in (4.5) represents a linear function of λ, whereas the second term represents a multi-branch function. In Figure 4.3 these multi-branch functions are plotted for several values of m orders (m = 0,1,3 for simplicity). The intercept of the line, representing (the negative of) the first term in (4.5), with every branch for a certain order m, leads to solutions to (4.5) for that value of m. Thus each equation of form (4.5) (for an order m) has several solutions indexed by i (=1,2,…) known as decay modes (as in the conventional PCD). In Figure 4.3 the intercepts of the line for 1000 cm/s SRV are shown for a sphere with diffusion coefficient of 30 cm^2/s and radius of 300 μm. After the λ values for the i-mode decays are calculated from the intercepts as in Figure 4.3, the final charge kinetics can be written with its several exponential decays of "orders" m and "modes" i, as is represented in (4.3). It is important to note that as SRV increases, the first mode of zeroth order approaches the first mode of order one and the effect of interference of the several modes (absent in planar case) becomes more serious. Similarly, the charge kinetics is expected to approach the planar wafer case with a single apparent exponential decay when surface recombination is suppressed. We will use this conclusion in Section 4.3 to characterize the spherical bulk.

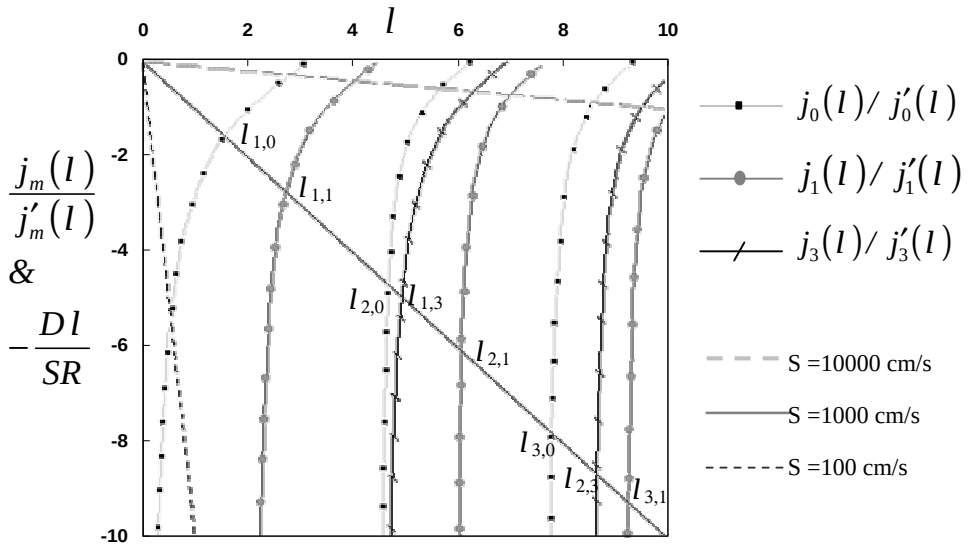

Figure 4.3: The plot of the first and the second terms of Equation (4.5) with several values of SRV, and for different orders m; the intercepts are the λ solutions of (4.5) for the case of R = 300 μm, D = 30 cm^2/s, and S = 1000 cm/s.

For each decay term, the factor $\Gamma_{i,m}$ is obtained from the initial conditions of the decay event. The excess carrier density at time zero, i.e. after the laser pulse excitation ends, dictates the initial condition. If the pulse width is short, the excess carrier at any position inside the sphere will be equal to the generation rate *G* at that position for the particular wavelength of the excitation l.

$$\Gamma_{i,m} = \frac{(2m+1)l_{i,m}^2}{pR^2} \cdot \int_0^p \int_0^R G(r,q) \cdot r^2 j_m\left(l_{i,m}\frac{r}{R}\right) \cdot sinq\ P_m(cosq) dr\, dq \tag{4.6}$$

The time dependent conductivity Δσ(t) follows the decay in the carrier concentration [41] and will then be expressed with the same system of orders m and modes i,

$$s(t) = \sum_i \sum_m \Psi_{i,m}\, exp\left[-\left(\frac{1}{t_{eq}} + D\frac{l_{i,m}^2}{R^2}\right)t\right] \tag{4.7}$$

where $\Psi_{i,m}$ values can be normalized for simplicity to remove the effect of mobility and electronic charge which are common among all $\Psi_{i,m}$ values.

4.1.3 One Dimensional Spherical PCD vs. Planar PCD

As is seen in (4.8), because of the two-dimensional charge kinetics, the photoconductivity decay consists of several exponential terms with time constants that include contributions from bulk and surface. We define a notation of $\tau_{s\text{-}i,m}$ for the surface contribution in the time constant of the i-th mode of order m corresponding to $\lambda_{i,m}$, which is in turn a function of SRV through (4.4).

$$\frac{1}{t_{s-i,m}} = D\frac{l_{i,m}^2}{R^2} \tag{4.8}$$

If the laser excitation were radial instead of normal, the zenith variation would disappear and charge kinetics would reduce to one dimension similar to a planar wafer. In this case the only existing order would be m = 0 with different modes (i = 1,2,…). Figure 4.4 shows the principle decay mode in a planar wafer and a sphere subject to radial excitation (one-dimensional). The PCD interpretation in this case is similar to planar wafer measurement. However, the sphere decay time constants $\lambda_{i,0}$ show a different dependency on SRV compared to planar wafer and may be more or less sensitive to SRV depending on the sphere radius. The main difference arises from the fact that the surface recombination contribution may be more (less) if the surface to bulk ratio increases (decreases). Consequently, the principal surface equivalent lifetime in a sphere under radial illumination $\tau_{s\text{-}1,0}$ (or simply τ_s)is essentially different from the case of a planar wafer as Figure 4.5 shows, yet behaves relatively similar.

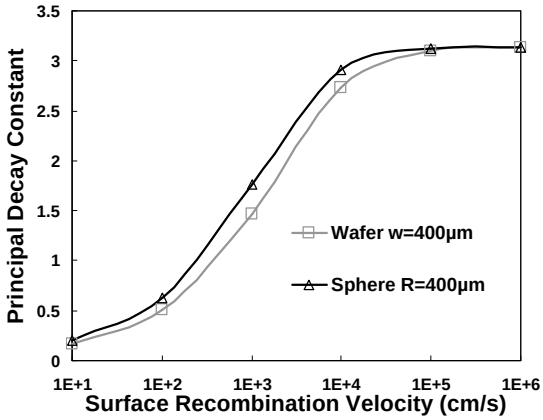

Figure 4.4: Calculated principal decay constants in a planar wafer λ_1 and a sphere with radial (1-D) excitation $\lambda_{1\text{-}0}$.

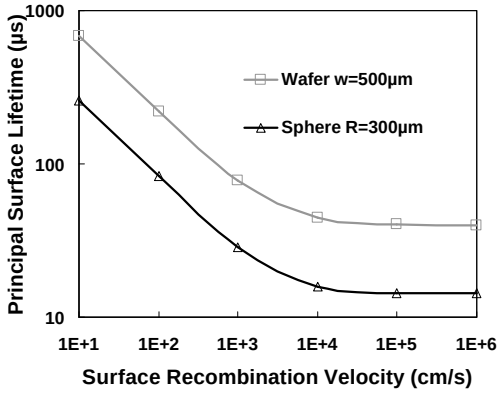

Figure 4.5: Calculated surface recombination lifetime in planar wafer and sphere with radial (1-D) excitation; in absence of 2-D charge kinetics, the sphere behaves similar to a planar wafer.

4.1.4 Multi-Order Model of Spherical PCD

For the planar case, the existence of multiple decay modes influences the conductivity signal only in a short period due to quick fading of various modes, and only a single exponential practically appears in the measurement because of the principle mode as stated in (4.1). In contrast, fitting single exponential to the conductivity of a sphere leads to considerable error due to the presence of higher orders. This is due to the fact that the principal mode of different orders (m = 0, 1 …) may last long and undermine the single exponential assumption even though higher modes (i = 2,

3 ...) will still fade out quickly. Table 4.1 shows that the existence of higher order decay modes in a sphere compared to a planar wafer. In fact, the principal mode of the first order creates a decay term that does not fade out immediately, and a one-dimensional approach will be inaccurate.

Figure 4.6 highlights the time extent of activity of the higher orders of decay in a sphere with similar parameters as in a planar wafer in which only different modes are considered. The extraction of the apparent lifetime in spheres is complicated mainly due to mixing of the principal mode of the zeroth and the first order decays and a single exponential fit to the PCD signal of spheres will not produce repeatable results.

Table 4.1: Calculated decay constants in planar wafer and spherical silicon for s = 10000 cm/s for wafer thickness of 500μm and sphere of radius 300μm.

Planar wafer	$\lambda_{s\text{-}1}$			$\lambda_{s\text{-}2}$	
	2.808	$$	$$	5.631	$$
Spherical Silicon	$\lambda_{s\text{-}1,0}$	$\lambda_{s\text{-}1,1}$	$\lambda_{s\text{-}1,2}$	$\lambda_{s\text{-}2,0}$	$\lambda_{s\text{-}1,3}$
	2.836	4.066	5.227	5.717	6.352

$$: only different modes of decay exist in a planar wafer

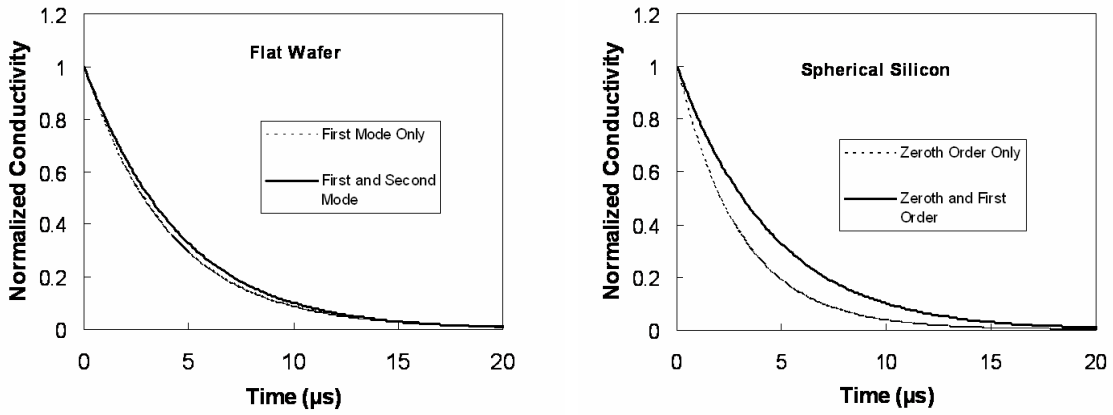

(a) (b)

Figure 4.6: Calculated conductivity decay in (a) planar wafer with different modes, (b) silicon sphere with principal modes (i = 1) of orders zero and one (m = 0,1).

4.1.5 Experimental Spherical PCD Measurement Results

Figure 4.7a shows an experimental PCD signal measured on a stack of spheres with 904 nm wavelength laser excitation (~30 μm penetration depth in silicon). By a simple single-exponential technique, the extracted apparent lifetime (by the measurement system software) is 1.38μs. It is seen in Figure 4.7b that the extracted apparent lifetime does not exactly match the whole time span of the measurement, especially out side the interval between 1μs and 2μs. Considering quick fade-out of higher modes and measurement error of around 10% for the microwave components, the extracted apparent lifetime is expected to be consistent with the logarithmic experimental curve of Figure 4.7b from well below 1μs to around 3.5μs for a real single exponential decay; This is apparently not observed due to lack of accuracy of the single exponential model.

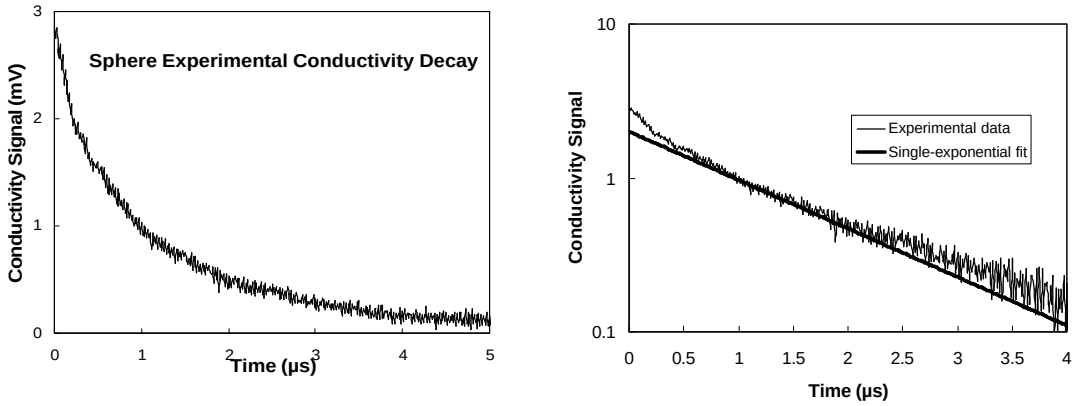

(a) (b)

Figure 4.7: Experimental conductivity decay of silicon spheres (a) the PCD signal (b) a single-exponential fit by the measurement system software; the single exponential model is unable to produce an appropriate curve fitting.

To more accurately estimate the bulk and surface recombination rates, we fit a double-exponential pattern to the experimental data knowing from the calculations of the kind given in Table 4.1 that the dominant decays are the principal modes of the zeroth and the first orders. From the two exponents, two “apparent” lifetimes are obtained,

$$\frac{1}{t_{a1}} = \frac{1}{t_{eq}} + \frac{1}{t_{s-1,0}} \quad , \quad \frac{1}{t_{a2}} = \frac{1}{t_{eq}} + \frac{1}{t_{s-1,1}} \tag{4.9}$$

We calculate the surface recombination lifetimes based on the decay constants for different SRVs similar to the sample given in Table 1 for s = 10000 cm/s. From the difference between the experimentally measured apparent lifetimes in (4.9) and the theoretically calculated values through (4.8), the effect of bulk and surface can be separated.

Figure 4.8 shows a double exponential fit to the experimental data of Figure 4.7a. As is seen, the tail of the experimental curve (t > 2μs) is covered by the principal decay mode of the zeroth order kinetics and the initial part follows a first order (m = 1) exponential. The under test stack of spheres were initially etched to eliminate any surface damage from processing. The average radius of the spheres was measured to be 340~350μm. The calculated recombination lifetime from the double-exponential is 2.77 μs for the bulk equivalent lifetime τ_{eq}. The apparent lifetime can be taken as the time constant of the first exponential fit (which lasts longer) and equals 1.87 μs. As per the results above, the 1.38 μs apparent lifetime extracted by a single-exponential approach (the same technique used by the system for planar wafers) underestimates the lifetime.

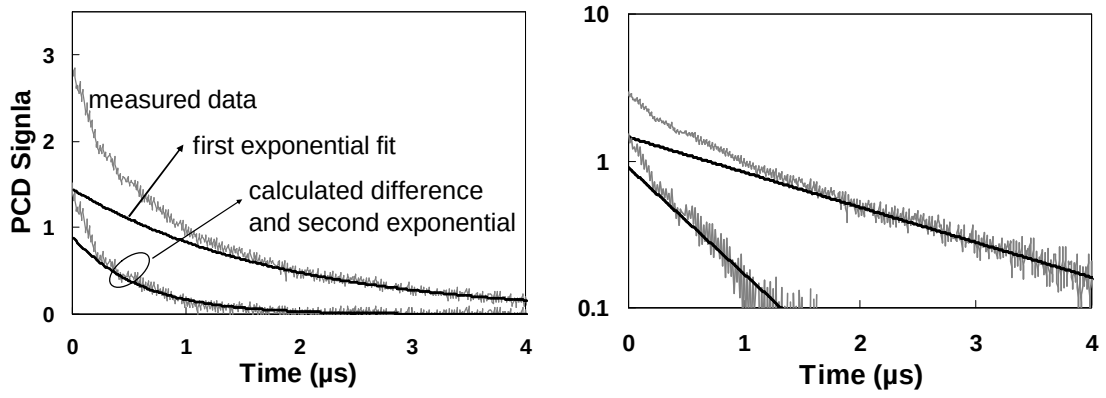

(a) (b)

Figure 4.8: Double exponential fit to the experimental conductivity decay data from Figure 4.7 based on the model developed in this section.

4.2 Characterization of Electronic Defects Using Carrier Lifetime

As we will discuss in full details using modeling spherical PV devices in Chapter 5, one of the most important material parameter in the efficiency of photovoltaic devices is minority carrier diffusion length which strongly depends on minority carrier lifetime. Thus the value of bulk equivalent lifetime in silicon spheres is an appropriate figure to asses the material quality of produced spheres for device fabrication purposes.

At the same time, lifetime is an extremely sensitive parameter to structural defects and impurities. Therefore, in addition to assessing the material quality for device modeling/fabrication purposes, lifetime measurements can be used to monitor the process steps. After the spheres are produced from OFP clusters or granular beads, there are several steps that affect the impurity and especially electronic defects, such as melt and recrystallization for impurity elimination, denuding for oxygen removal, diffusion for pn junction fabrication, defects annealing, and other potential processes such as rapid thermal oxide passivation. Lifetime measurements can be employed to optimize the processes and increase the efficiency of the final device or to ensure the process step is being performed under the correct conditions.

4.2.1 Grown-in and Process-Induced Defects

In the standard process flow for the growth of silicon spheres, prior to melt and recrystallization, high concentration of impurities may exist in the silicon materials used for the device fabrication. After recrystallization, although the transitional metals and structural defects are greatly reduced, high oxygen concentration still exist. The oxygen removal from the subsurface region using denuding for 24 to 48 hours at temperatures above 1200 ^{o}C leads to structural defects creation which was identified using defect etching in Chapter 3.

Once silicon spheres of the appropriate electronic properties are grown, phosphorous diffusion is usually performed at 900~950 ^{o}C for durations of less than 1 hour. For deep junctions, a second diffusion may be added after removing the phosphosilicate glass, which may or may not be followed by an additional drive-in step at similar process conditions without phosphorous dopant source.

Radio frequency PCD lifetime measurement has been previously used to evaluate the quality of spheres produced from MG-Si and SG-Si [42] and also as a process monitor for the effectiveness of the melt and recrystallization process [43].

We performed PCD lifetime characterization on different stacks of spheres from several process steps. In order to eliminate any ambiguities about the bulk quality of silicon spheres, we eliminated the effect of surface recombination in the μ-PCD measurement using solution based passivation during the measurements. Concentrated HF and iodine solution were used to minimize surface recombination. Once the surface recombination is eliminated (or considerably slowed down compared to bulk recombination), the measured apparent lifetimes can be considered as bulk lifetime. Thus we interpreted the measurement results directly as bulk equivalent lifetime of the spheres.

Figure 4.9 shows the results of lifetime measurements on different stacks of spheres. The low carrier lifetime in the spheroidized and recrystallized spheres is an indication of high defect density due to structural defects and oxygen. These electronic defects that contribute to the fast recombination of carriers are regarded as grown-in defects. Although denuding removes the high concentrations of oxygen, it actually induces a high density of defects due to very high temperature (~1200 ^{o}C) and long duration (>20 hrs). The result is again low lifetime values due to process induced lattice defects.

The diffusion process appears to anneal to some extent the lattice defects induced by the denuding process. However, a more critical annealing step in the electronic quality of the spheres (namely carrier lifetime) appears to be the controlled cool down after denuding. For spheres cooled down slowly enough to have sufficient stay at defect annealing temperatures, higher carrier lifetimes are achieved. The controlled cool down after denuding, when combined with the annealing effect of lower temperature diffusion and additional gettering that is facilitated by diffused phosphorous leads to highest lifetime values.

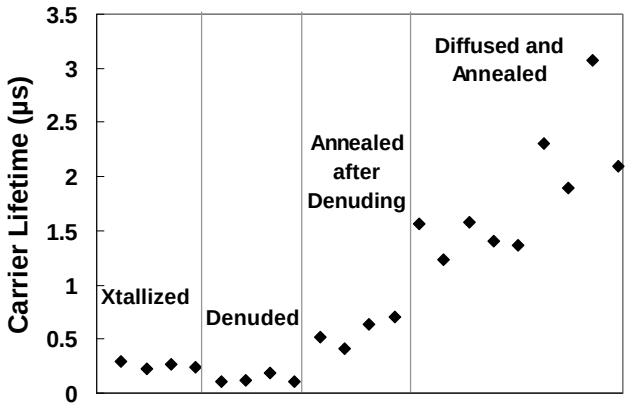

Figure 4.9: Minority Carrier lifetime measured on various sphere stacks throughout the standard process flow.

4.2.2 Process Development with Carrier Lifetime as Process Monitor

Characterization of electronic defects through lifetime measurement can also be employed to evaluate the effectiveness of any potential additional steps developed for the device fabrication in spherical cells. It is also a useful tool to ensure the developed processes do not cause much degradation in the spherical material when enhancing other parameters.

Some examples of potential process steps that can be developed for advanced device fabrication are additional annealing steps for gettering purposes, high temperature oxidation for surface passivation purposes, and related post-oxidation annealing steps.

Separation of Bulk and Surface Effects: Figure 4.10 shows the effect of high temperature oxidation on the evolution of electronic defects in the bulk and at the surface of silicon spheres. While processing spheres in nitrogen ambient mainly affects the bulk properties, oxidation influences both the bulk and the surface. The processes shown are performed with a quick ramp to the desired oxidation temperatures with 5 minute stay at maximum temperatures of 900 and 1000 ^{o}C. The quick ramp to high temperature process apparently degrades the bulk as is observed on the samples processed in nitrogen ambient. If the surface is oxidized, the drop in carrier lifetime appears to be even higher, which implies the oxidation induced defects are added to the bulk defect creations. An annealing step at 850 ^{o}C is effective to counteract the defect creations. The bulk defects in the samples processed in nitrogen ambient seem to be equally cured. We conclude that the same annealing effect exists for the bulk defects evolved during oxidation as well. Thus it seems that the higher temperature oxidation leads better surface quality as higher lifetime is achieved on the 1000 ^{o}C oxidized spheres.

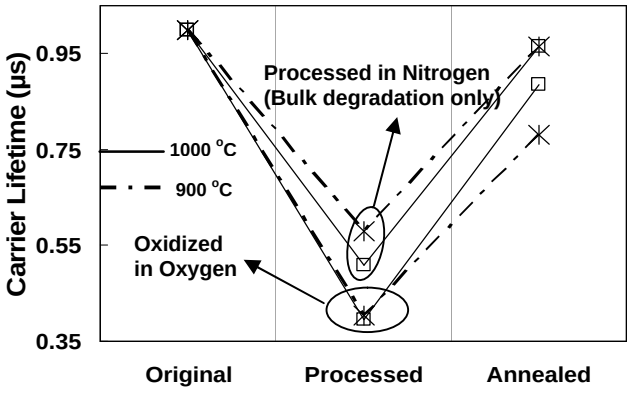

Figure 4.10: Carrier lifetime change during different high temperature processes and anneals implemented using RTP system.

Defect Annealing and Gettering: After denuding, low concentration of oxygen exists in the subsurface region (denuded zone). However, in addition to impurities carried along from the melt and recrystallization step, a high density of structural defects is created. Appropriate annealing and gettering steps are required to improve the electronic quality of the spherical silicon material. An example of the application of carrier lifetime to characterize electronic quality of a stack of denuded spheres is shown in Figure 4.11 for two processes, LH and HL. The processes consist of 5 minute 850 ^{o}C and 2 minute 1000 ^{o}C steps with the low temperature step first followed by the high temperature for LH process and vice versa for HL.

As seen in Figure 4.11, the thermal pattern of HL is more effective in improving the carrier lifetime. Several mechanisms can affect the creation, annihilation, and redistribution of electronic defects. Oxygen atoms may exist as individual interstitials or as concentrated Si-O precipitates depending on the thermal history of the sphere and the background concentration in the start material. Oxygen atoms may be exchanged between the two mentioned states depending on temperature pattern of process steps. Furthermore, the interaction of oxygen defects and metallic impurities makes the process of purification even more complicated. Oxygen sites are appropriate sinks for metal atoms in silicon lattice. Lattice defects can also be annealed using proper annealing temperatures and durations. High temperature (~1000 ^{o}C) is known as appropriate condition for gettering [6] and lower temperature anneals appear to be effective in removing structural defects as shown in Figure 4.10. The HL pattern seems to speed up gettering first, followed by an annealing of the defects. During the LH process, more defects are created during the final high temperature phase, which leads to poor lifetime compared to HL process.

Therefore, the thermal pattern of the process steps can be tailored for certain feedstock to effectively combine crystallization, impurity segregation, oxygen precipitation, oxygen effusion, gettering, and defect annealing. In short, by optimizing the temperature and the flow of process

steps using carrier lifetime as the monitoring tool, it is possible to enhance the quality of the finished sphere, leading to high carrier lifetime and diffusion length, which will in turn result in higher efficiency of the device.

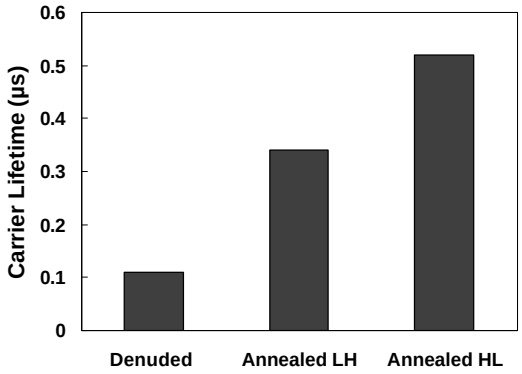

Figure 4.11: Effect of different annealing steps after denuding on carrier lifetime; LH and HL correspond to the implemented process order: the 5 minute low temperature (850 ^{o}C) anneal L and the 2 minute high temperature process (1000 ^{o}C) H.

Oxidation Process Optimization: When oxidation is employed for surface passivation purposes, in addition to oxidation temperature and duration, it is important to optimize the temperature profile especially in the case of rapid thermal oxidation (RTO). The minority carrier lifetime of the oxidized spheres is a useful tool to monitor the effectiveness and to optimize this process. Figure 4.12 shows three high temperature processes on similar stacks of spheres of original carrier lifetime of 1.2~1.3 μs, with the resulting lifetimes indicated. Processing below 750 ^{o}C generally has negligible effect on both surface and bulk. The oxidation steps at 900 ^{o}C for 2.5 minutes shows significant reduction in the lifetime (down to 0.7 μs). However, by slow temperature ramp-up and ramp-down, significantly higher carrier lifetime can be achieved (0.86 μs). The process can be further optimized for better lifetime values and further annealing steps can be employed to maximize the achievable lifetime. The 950 ^{o}C annealing for another 2.5 minutes proves to increase the as-oxidized lifetime to 1 μs.

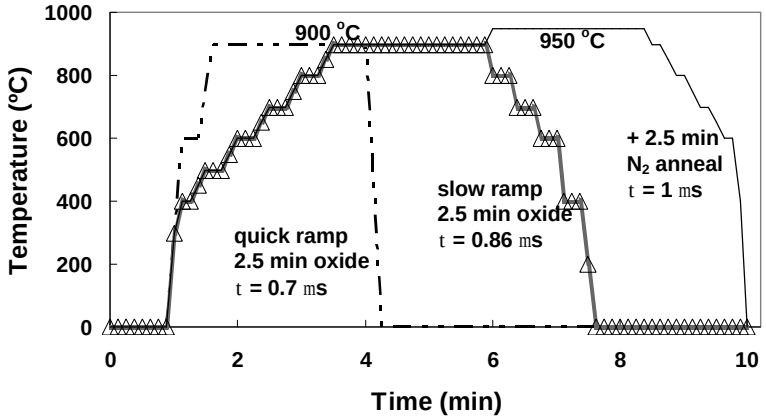

Figure 4.12: The effect of different oxidation processes performed in RTP on the measured carrier lifetime of spheres with original carrier lifetime of 1.2~1.3 μs; the oxidation followed by annealing appears to result in highest carrier lifetime.

In general, any high temperature process on high quality spheres (τ > 1 μs) seems to degrade the bulk equivalent lifetime in the spheres unless the processes are optimized to limits through repetition on different sets of spheres. However the as-measured equivalent lifetime is not the only significant parameter in the device performance. One of the important parameters in the performance of photovoltaic devices, besides bulk recombination rate that affects the short circuit current, is surface recombination rate that affects the open circuit voltage. It is desired to minimize the surface recombination rate (maximize τ_s) to obtain higher open circuit voltages. We estimated the effective bulk and surface recombination rates in spheres prior to and after oxidation and annealing by measuring the spheres with and without HF passivation (assuming HF passivation reduces the surface recombination rate considerably below the bulk rate). Figure 4.13 shows the recombination rates on spheres (from standard process flow) and after oxidation and annealing of Figure 4.12. As is seen in this figure, although the bulk recombination rate increases after oxidation over the original value, the surface recombination drastically decreases. The former effect reduces the photocurrent of the device, and the latter slightly counteracts this reduction, and significantly reduces the saturation current acting towards higher output voltage.

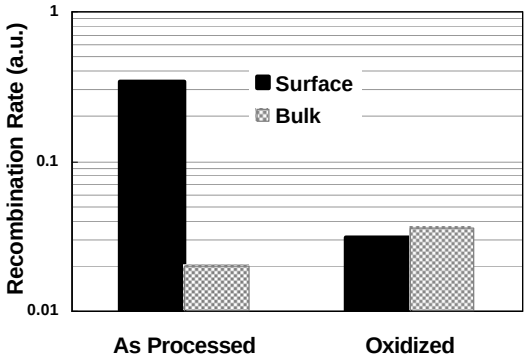

Figure 4.13: Evolution of bulk and surface recombination processes during oxidation and nitrogen annealing process performed according to Figure 4.12.

4.3 Non Uniformity of Electronic Properties in Silicon Spheres

During the formation of silicon spheres, the controlled solidification process causes crystallization to proceed in the radial direction. Impurities (including oxygen) are distributed radially due to segregation at melt-solid interface during crystallization. The denuding step then removes oxygen from the subsurface region through out-diffusion of oxygen atoms. This is in fact a high temperature soak [29] during which O atoms are partially evacuated from the subsurface region. On the other hand, O sites in the central region act as intrinsic gettering sites for remaining metallic impurities during the annealing/gettering steps. The overall effect is that the material quality is somewhat inferior in the central regions. As a consequence, the carrier lifetime decreases from surface to center and a decreasing profile is expected for the minority diffusion length, the rate of which influences the device performance. The fast degradation of bulk material as we move from surface to center translates to a low efficiency at the device level. It is important to characterize these variations for device modeling and design purposes. Moreover, the fabrication process should be optimized for deepest oxygen-free denuded zone and maximum diffusion length in the bulk. In this section, we analyze the PCD results to obtain the spatial distribution of lifetime, as well as the denuded zone depth.

4.3.1 Radial Variations of PCD Carrier lifetime

The model developed for interpreting the PCD measurement results in silicon spheres in Section 4.1 was based on an "equivalent" bulk lifetime for the spheres. The equivalent bulk lifetime in fact represents a value that is assumed to be spatially constant inside the spheres and corresponds to the rate of the effective recombination that occurs inside the sphere. However, measuring lifetime on a stack of spheres etched to smaller radii, shows that the lifetime is not constant in the spherical bulk (Figure 4.14) and the radial distribution of oxygen, other impurities, and defects leads to a non-uniform carrier lifetime in practice.

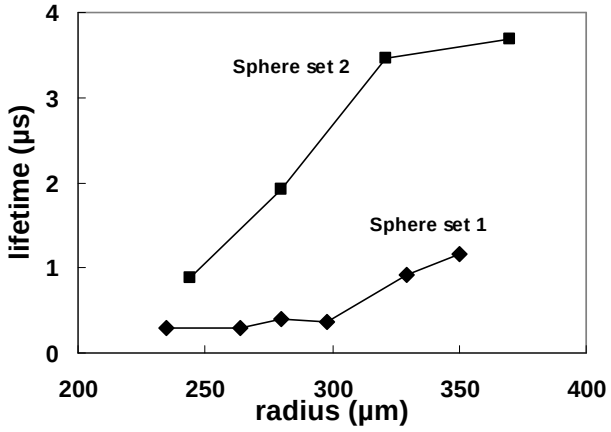

Figure 4.14: Results of equivalent carrier lifetime measurements on spheres with different radii after etching; equivalent lifetime decreases on spheres etched to smaller radii.

This non-uniformity from surface to center causes a slight decrease in the carrier lifetime across the denuded zone and a drastic change afterwards (inner core). The initial value of the apparent bulk lifetime is a measure of the quality of the spherical material, which is determined by the subsurface quality as well as the rate of decrease towards center. The depth at which the lifetime drops below a certain fraction of the initial value (e.g. 90%) can be assumed as the denuded zone depth. This depth is related to the denuding process and must be ideally maximized through a long denuding step. We used the equivalent lifetime of processed spheres as a process monitor in

the previous section. The spatial variation of carrier lifetime can be used for device modeling purposes and it is important to note that the measured PCD carrier lifetimes are not exactly the spatial distribution of carrier lifetime, but a representation of the remaining spherical bulk. For modeling purposes, it is important to have the actual lifetime value at any radius. Similarly, the depth of the denuded zone which is an indication of the effectiveness of denuding does not explicitly appear in the measured equivalent lifetime. Therefore, developing a model to translate the variation of the equivalent lifetime to actual distribution of the carrier lifetime and the depth of denuded zone can be greatly helpful in device modeling and further process monitoring.

4.3.2 Denuded Zone Depth and Spatial Distribution of Carrier lifetime

In order to model minority carrier (electron in p-type sphere) lifetime non-uniformity, we assume that electron lifetime starts from a subsurface value of τ_{sub} and will decrease towards the center. We define the edge of the denuded zone at radius $r = R_i$ inside the sphere of radius R where the carrier lifetime drops to around 90% of its subsurface value. This definition of denuded zone edge corresponds to a decrease in diffusion length at R_i to approximately 95% of its original value at R, as the diffusion length varies mainly due to lifetime variations rather than diffusion coefficient variations.

The radial variations in the bulk carrier lifetime $\tau_b(r)$ can be modeled by a continuous decrease in bulk lifetime including the subsurface lifetime and a unitless function u(r) that would decrease as we approach the centre (r = 0).

$$\frac{1}{t_b(r)} = \frac{1}{t_{sub}} + \frac{1}{t_{sub}u(r)} \tag{4.10}$$

We adopt a quadratic function for u(r) normalized to sphere radius R and including a model parameter γ which represents a measure of denuded zone depth.

$$u(r) = g^2 \frac{r^2}{R^2} \tag{4.11}$$

As Figure 4.15 shows, variation of model parameter γ in the range of 3.5 to 7 corresponds to R_i changing from around 250 μm to 100 μm in a sphere with radius of 300 μm, i.e denuded zone depth of around 50 μm down to 200 μm.

It is worth mentioning that (4.10) is a key assumption for u(r) in modeling the PCD lifetime and extracting the approximate spatial distribution of actual carrier lifetime as it enables us to obtain analytical interpretation of PCD measurement.

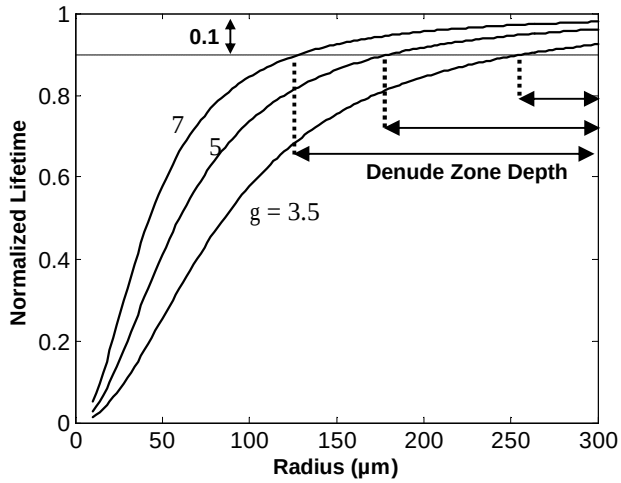

Figure 4.15: Model of (4.10) for spatial distribution of carrier lifetime; parameter γ determines the depth of denuded zone (10% decrease in lifetime).

4.3.3 Charge Kinetics in Radially Non-Uniform Spheres

As we saw at the beginning of this chapter, when spheres (e.g. p-type) are stimulated by a laser impulse, the generated excess minority carriers (electrons) redistribute and recombine according to the continuity equation in a spherical system of coordinates (with azimuthal symmetry). The solution of the continuity equation includes Bessel (varying with radius) and Legandre (varying with zenith angle) functions and the resulting charge kinetics consists of m-th order i-th mode

decay lifetimes with m = 0,1,3,… and i = 1,2,... for each order m. We saw in Section 4.1 that the principal decay constant is the first mode of the zeroth order. This principal decay constant is actually independent of zenith angle. Thus if we reduce the charge kinetics equation to include only radial variations, and at the same time eliminate the effect of surface (by immersion in HF for instance), we relate the principal decay constant of PCD to bulk material parameters (τ_{sub} and γ) by monitoring the PCD principal decay constant.

$$\frac{\partial n}{\partial t} = D\left[\frac{1}{r^2}\frac{\partial}{\partial r}\left(r^2\frac{\partial n}{\partial r}\right)\right] - \frac{n}{t_b(r)} \tag{4.12}$$

Combining the model definition in (4.10) and (4.11) for $\tau_b(r)$ into (4.12) results in a partial differential equation with a constant K^2 for separation of variables. The radius dependent terms of (4.12) form a Bessel equation while the time dependent terms of the equation lead to an exponential decay in which the principal decay constant is related to τ_{sub} and separation constant K^2 (K^2 is in turn related to γ and surface recombination velocity at r = R). The resulting photoconductivity of the sphere is then obtained as:

$$\Delta s(t) = \Gamma exp\left[-\left(\frac{1}{t_{sub}} + DK^2\right)t\right] \tag{4.13}$$

where Γ is a constant. The value K^2 in (4.13) is similar to the λ^2/R^2 in (4.7). However, λ is determined from the boundary condition of SRV assuming an equivalent bulk lifetime (spatially constant), whereas K is related to spatial variations of carrier lifetime, and is determined by applying the negligible recombination at the surface as the boundary condition imposed on the separated Bessel equation. K is related to τ_{sub} and γ through an implicit equation:

$$\frac{J_a'(KR)}{J_a(KR)} = \frac{1}{2KR} \tag{4.14}$$

In which J and J' are the Bessel function of the first kind and its derivative and α is a function of τ_{sub} and γ:

$$a = \frac{1}{2}\sqrt{1+\frac{4R^2}{g^2 t_{sub} D}} \tag{4.15}$$

Equations (4.13)-(4.15) suggest that for a silicon sphere with known subsurface carrier lifetime and denuded zone depth, we calculate the time constant of PCD after a laser diode impulse creates excess carriers in the sphere, which we have named apparent PCD lifetime τ_a of the sphere as appears in (4.13).

While we are able to calculate the apparent lifetime for given subsurface carrier lifetime and denuded zone depth, the reverse procedure is required in practice, i.e. we need to extract subsurface lifetime and parameter representing spatial variation of lifetime (γ) by performing PCD measurements. For the reverse operation (going from PCD apparent lifetimes to bulk carrier lifetime), we will need at least two PCD measurements to extract the two parameters of interest, τ_{sub} and γ.

4.3.4 Measurement and Extraction of Radial Profile of Carrier Lifetime

For the purpose of a second measurement to produce an extra piece of information, we observe the following fact: if after a PCD measurement, silicon spheres are chemically etched to radius R^* and the measurement is repeated on them, among the Equations (4.10)-(4.15), only (4.14) changes; (4.14) corresponds to a physical boundary at the surface, whereas other equations in which R appears are based on the assumed u(r) model and the physical radius does not play a role. In other words, if we perform PCD measurement on a set of spheres, and then reduce the radius of the spheres (e.g. by chemical etching), the only change in the model is the implicit calculation of K through (4.14).

Based on this observation, we perform two PCD measurements. First, the spheres are exposed to laser pulse and the decay in photoconductivity is monitored to obtain the original apparent lifetime τ_a for a sphere with radius R. Next, the spheres are chemically etched to a new radius R^* and a second PCD measurement is performed to obtain a new apparent lifetime τ^*_a. This apparent lifetime corresponds to new value of K^* which is computed from (4.14) by replacing R with R^*. It is important to note that (4.15) is derived from the solution of the Bessel equation obtained by separation of variables in (4.12) and is only influenced by the assumed model for u(r); thus there is no need to modify this equation according to the new radius R^*.

By performing these two measurements, the two apparent lifetimes are related to the subsurface lifetime and values of K and K^*.

$$\begin{aligned} \frac{1}{t_a} &= \frac{1}{t_{sub}} + DK^2 \\ \frac{1}{t^*_a} &= \frac{1}{t_{sub}} + DK^{*2} \end{aligned} \tag{4.16}$$

with K defined in (4.14) and K^* defined similar to (4.14), yet for the new radius.

$$\frac{J'_a\left(K^*R^*\right)}{J_a\left(K^*R^*\right)} = \frac{1}{2K^*R^*} \tag{4.17}$$

The values of K and K^* in fact realize (through the intermediate parameter α) the inclusion of model parameter γ in the two measured lifetimes. The set of (implicit) equations of (4.14), (4.16) and (4.17) must be numerically solved with τ_a and τ^*_a obtained from PCD measurements on spheres with original radius of R and then etched to radius R^*. The numerical solution is tedious and starts with a primary assumption for γ and continues with iterative calculation of τ_{sub} and γ. A computer code can be generated to receive the values of measured lifetimes and the corresponding sphere radii and compute the model parameters.

Figure 4.16 shows the experimental results of PCD on a set of spheres of an approximate radius of 310 μm. with an extracted equivalent lifetime of 3.46 μs along with the results on the same spheres after chemical etching of the radius to around 270 μm. The equivalent lifetime of the spheres after etching is 2.99 μs.

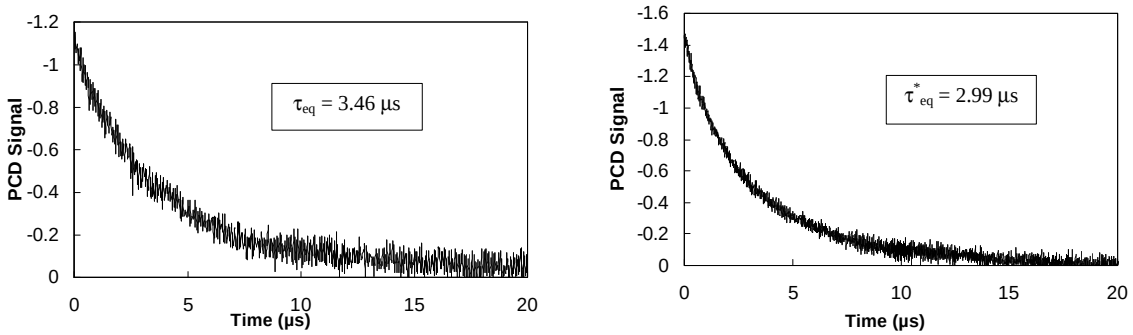

(a) (b)

Figure 4.16: Experimental conductivity decay measured on a stack of silicon spheres (a) original radius of 310 μm (b) chemically etched to radius of 270 μm.

It must also be noted that the spheres were passivated by immersing in solution during the PCD measurements to minimize surface recombination. In presence of non-negligible surface recombination velocity, the model will not be valid as we assumed the only mechanism affecting decay of photoconductivity is bulk recombination. An important aspect of the experimental PCD measurements on the spheres is that the radius reduction of the spheres must be sufficient to obtain distinguishable measured lifetimes before and after etching; the difference must be sufficient to dominate the inaccuracy that may rise from PCD lifetime estimation. However, if the thickness of the stripped layer is very large compared to the denuded zone depth, the second measurement will be insensitive to the subsurface lifetime. This may result in inaccurate parameter extraction.

By iterative solution as explained above, model parameters of 4.1 μs for τ_{sub} and 3.69 for γ are computed. These results correspond to spheres with 52 μm deep denuded zone where the electron lifetime is approximately 3.82 μs. Figure 4.17 depicts the spatial variation of carrier lifetime resulting form the extraction of model parameters. It can be found out from the results that the extracted value for the model parameter τ_{sub} (subsurface lifetime) is not the actual bulk lifetime just below the surface $\tau_b(r = R)$, but rather a characteristic number that represents the bulk lifetime only when the effect of spatial variation is included through the other model parameter γ.

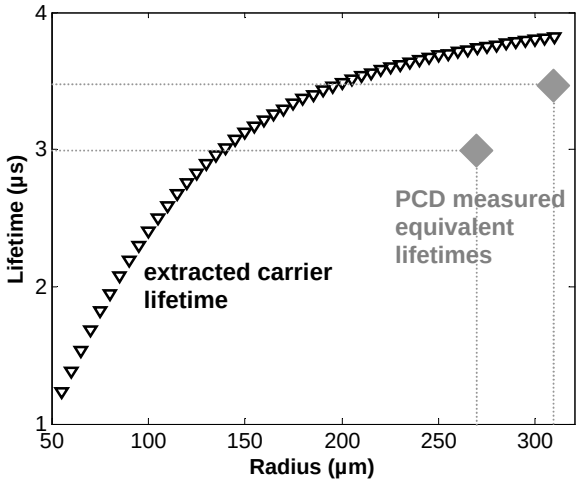

Figure 4.17: Extracted spatial distribution of carrier lifetime from two PCD measured lifetimes on spheres with different radii; the actual carrier lifetime at certain radius r inside the sphere is more than the equivalent lifetime measured on spheres of radius r.

4.3.5 Characterization Approach for Electronic Properties and Non-Uniformities on Silicon Hemispheres

An alternative approach to the contactless PCD measurement can be the modulation of voltage between the metal contacts patterned at different radii of a hemisphere with constant current and static optical generation as in Figure 4.18a. The contacts in Figure 4.18b were developed using

optical lithography and constant light measurements were performed, with the assumption that photoconductivity $\Delta\sigma$ is proportional to carrier lifetime τ under constant optical generation G.

$$\Delta s \propto G \times t \tag{4.20}$$

However, the effect of contact resistance can be dominant over the variations of photoconductivity due to spatial profile of lifetime. In a modified setup, illumination pulses can be applied to detect the transient in conductivity and extract the spatial profile of carrier lifetime.

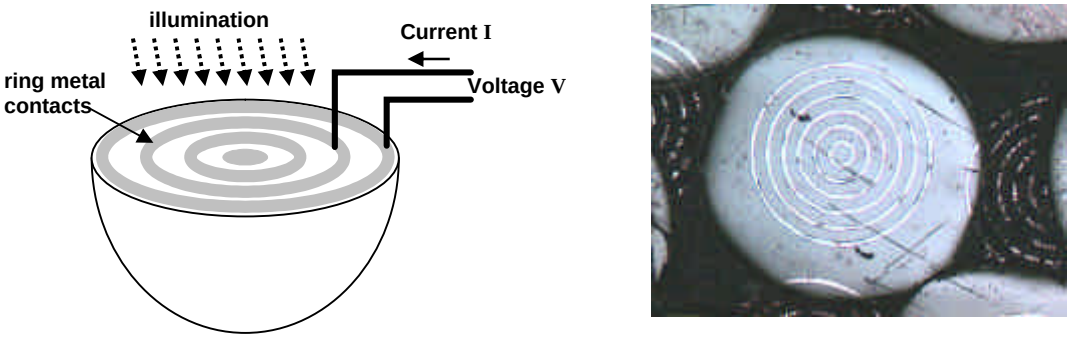

(a) (b)

Figure 4.18: Contact measurement of photoconductivity to extract radial profile of carrier lifetime in hemispheres (a) setup (b) aluminum contacts patterned by lithography.

4.4 Summary

A model was developed to interpret photoconductivity decay measurement results in silicon spheres. The model makes it possible to separate and extract bulk equivalent and surface equivalent carrier lifetimes. The equivalent bulk lifetime can be used as a tool to asses the quality of produced and processed spheres at different stages of the fabrication flow. Separation of bulk equivalent and surface lifetimes facilitates process monitoring for the introduction and development of additional fabrication steps such as high temperature oxide surface passivation. It can also be helpful in optimizing the denuding and annealing process conditions.

By further improving the model, the spatial profile of carrier lifetime was extracted from PCD lifetime measurements. The actual position dependent value of lifetime is useful for device modeling purposes. From these calculations, the depth of the denuded zone was also extracted in the spheres. This latter parameter can be used as a tool to accurately monitor and optimize the denuding and the following annealing process steps as they determine the extent of oxygen soak and the progress of precipitation and gettering.

Chapter 5

Development of Three Dimensional Model for Spherical Photovoltaic Devices

Spherical photovoltaic technology is a promising emerging technology for cost-effective terrestrial applications. Clear understanding of the spherical devices and ability to model their optoelectronic behavior are essential not only to further improve the performance but also to invent new generations of spherical devices. The photovoltaic device is in fact a spherical pn junction device (Figure 5.1) in which the carriers are generated in the spherical bulk and collected at the contacts on the sides. Due to geometrical and material-specific issues, spherical cells significantly differ from planar devices. Since all the existing models are developed based on the one dimensional planar PV devices, an accurate 3-D modeling is necessary for advanced device design and material processing optimization. The model must be able to accommodate the optical, electrical, and material aspects of the spherical device. The model can then be useful in performance prediction and also in providing a basis for device design and material fabrication.

The specific material and processing features of the spherical silicon, which play an important role in the performance of the device, must be taken into account for modeling purposes. These features that stem from the different growth and fabrication of Si spheres mainly affect the electronic properties of spherical silicon and were analyzed in details in Chapter 4.

In this chapter, a model is developed based on the geometrical and materials specific properties. In Section 5.1, the challenges of modeling due to the electronic properties specific to the spheres are discussed including non-uniformities in the spherical bulk.

A detailed analysis of the propagation and absorption of light in the spherical geometry is provided in Section 5.2. Based on this analysis, the optical model is developed in terms of photo-generation inside the spheres.

The optical model is followed by the electrical model of the spherical photodiode in Section 5.3, which deals with carrier collection. The current collected from the different region of the spherical diode are treated separately in this model, and by summing the monochromatic responses the quantum efficiency of the device is calculated. The I-V curve of the spherical device is generated by calculating the photocurrent (similar to the quantum efficiency but solar weighted) while the boundary conditions corresponding to different voltages are applied.

A simulation tool was developed based on this model, the simulation results of which are presented in Section 5.4. The results are interpreted to account for geometry specific and materials processing aspect of spherical devices. Moreover, the model results will be used in Chapter 7 as a basis for the design and the experimental work on the development of advanced device structures proposed for next generation spherical photovoltaic devices.

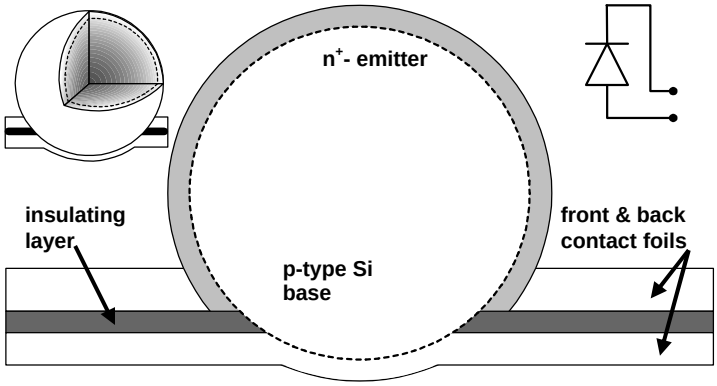

Figure 5.1: The structure of spherical pn photodiode used as solar cell.

5.1 Implications of Material Peculiarities of Spherical Silicon for Modeling

After p-type silicon spheres are formed from the start OFP clusters or granular beads, denuded, and annealed, the final step is a diffusion of phosphorous to create a spherical pn junction. The diffusion process is performed at around 950 ^{o}C for durations around 1 hour from an infinite dopant source that covers the whole surface of the sphere. The metallurgical junction is a spherical plane at a radius close to the sphere surface with around 1μm junction depth. As was mentioned in Chapter 4, the fact that O atoms are partially evacuated from the subsurface region and high density of defects exist in the inner shell of the spheres causes the minority carrier lifetime to degrade from surface to center. The overall effect was shown to be inferior material quality in the central regions; the minority diffusion length is thus expected to decrease. Following the model adopted in Chapter 4 for the radial distribution of minority carrier lifetime, the diffusion length is expected to be approximately constant in a denuded zone (dropping to 95% of subsurface value at the edge $r = R_i$) and then quickly decrease the center approached. Figure 5.2 shows the profile of the diffusion length for several depths of denuded zones. The model must be able to include the effect of variable diffusion length in the calculation of device parameters.

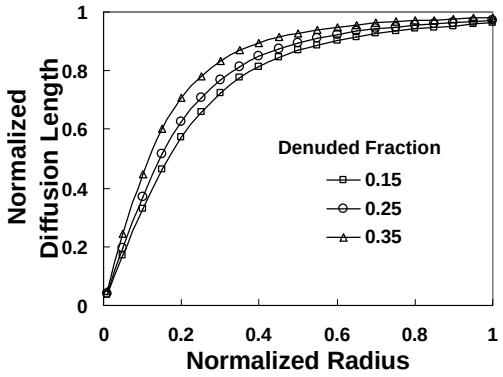

Figure 5.2: Diffusion length profile for different denuded zone depths based on the model the model of Section 4.3 used for modeling of this chapter.

5.2 Development of Optical Model

Unlike the case of planar devices the incidence angle changes with position in spheres leading to position dependent refraction, which complicates the modeling of photo-generation. In this section we model the wavelength (λ)- and position- dependent optical path of photons and photo-carrier generation rates using spherical coordinates. We also consider the incidence angle dependence of reflectivity.

For the purpose of modeling, we assume a smooth spherical surface and apply geometrical optics. More advanced optics such as statistical or lambertian optics take into account randomly rough [44] or regularly textured surfaces [45]. The adopted spherical system of coordinates (r,θ,ϕ) is shown in Figure 5.3. A ray incident at an angle γ from normal (radial) direction refracts by refraction angle β and travels a path of length χ before reaching an arbitrary point (r,θ,ϕ) inside the sphere. Because of the azimuthal symmetry (ϕ-independence) for normal exposure, any ray incident at (R,γ,ϕ) (R being the radius of the sphere) remains in the same constant-ϕ plane (e.g. plane of ABC in Figure 5.3). This reduces the three dimensional syatem to two dimensions for mathematical analysis.

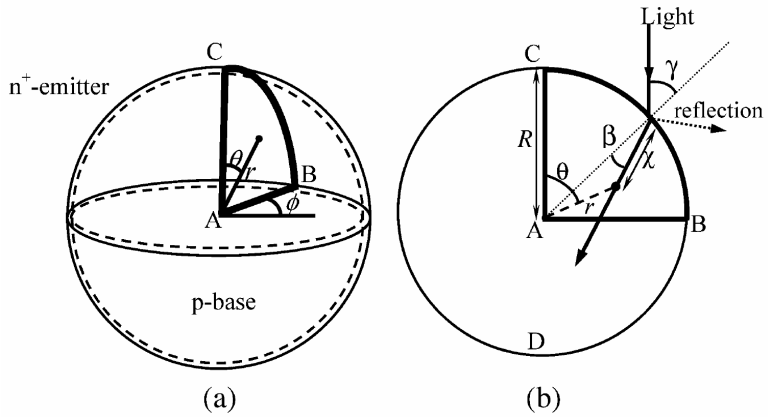

Figure 5.3: (a) Spherical coordinates used in the modeling with arbitrary point (r,θ,ϕ), (b) the path of monochromatic light inside the sphere on a constant-ϕ plane; due to symmetry, the constant-ϕ plane is representative of the whole system.

Photon absorption is most easily calculated by ray tracing. Figure 5.4 shows the traced path of equally spaced light rays incident on the surface between point B and C in Figure 5.3b for 600 nm wavelength, as they continue their path inside the sphere.

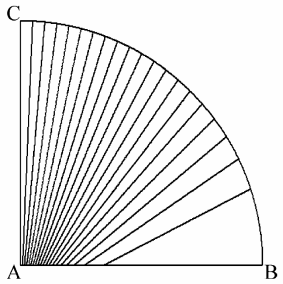

Figure 5.4: Simulated optical path of equally spaced rays of 600nm wavelength inside a sphere on plane ABC of Figure 5.3.

Considering the ray convergence and absorption pattern, i.e. dividing the exponentially decaying photon flux reaching a certain point by the distance from a neighboring ray, we estimate photon absorption density inside the sphere. Figure 5.5 shows the results of such calculation in the right half of the constant-ϕ plane of Figure 5.3b summed over the solar spectrum from 400 nm to 1100 nm. As seen in this figure, most of the photons are absorbed in the upper hemisphere leading to minimal carrier generation below the equatorial plane (line AB). The local peak in the generation rate below center of the sphere is due to ray convergence near the focal region of the sphere. Carrier generation in the lower hemisphere calculated by ray tracing equals around 1% of the total generation, while a large portion of it occurs in the region of low carrier lifetime near the center and thus has little contribution to collected current. Considering these results, we neglect the generation in the lower hemisphere. The data in Figure 5.5 consist of a huge matrix making it impossible to be deployed in electrical modeling. Also, as λ and the emitter width vary, different step and matrix sizes are required for numerical calculations. Step size must be very small for the emitter and for short λ due to large absorption coefficient; whereas the range in which generation

must be calculated in the base is large and demands larger step sizes or otherwise the matrix size will be huge. Thus, for every simulation the generation rate at any point in the upper half of the sphere is directly calculated instead of plugging in the data from ray tracing of Figure 5.5.

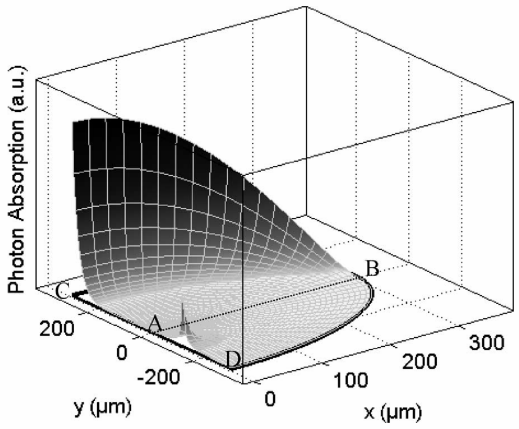

Figure 5.5: Simulated photon absorption pattern (by ray tracing) in a half circle constant-ϕ plane showing negligible absorption below the equatorial plane (line AB of Figure 5.3).

5.2.1 Length of Optical Path and Incidence Angle

To calculate the generation rate in the upper hemisphere, we observe, by tracing the paths of monochromatic light, that rays of the same λ do not intersect in the upper half (Figure 5.4). We mathematically verified that distance of the point where a refracted ray crosses the equatorial plane from the center monotonically increases (Figure 5.6) as the incidence point moves from the top C point towards point B, proving the result graphically derived from ray tracing in Figure 5.4.

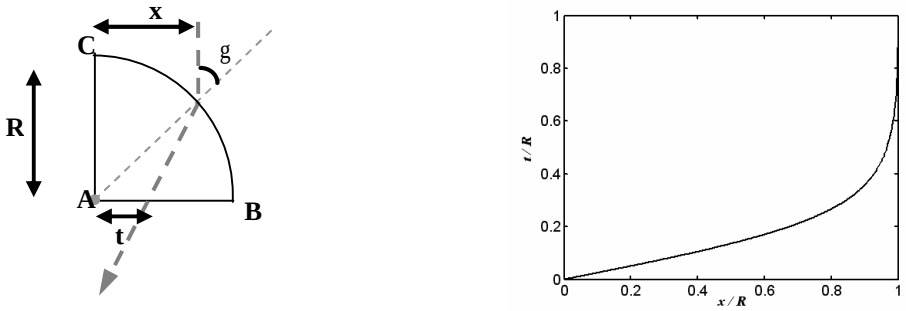

Figure 5.6: Monotonic increase of the distance of the incidence point on the equatorial plane (AB)

for beams farther from the axis; proof for no interference of the beams in the upper half of sphere. Therefore, the photogeneration due to monochromatic light at any point in the upper hemisphere can be calculated by considering the one single optical path that passes through that point. For a given λ, the length (χ) of the optical path passing through a ϕ-independent point (r,θ) can be calculated by solving equations (5.1)-(5.3), with the unknowns χ, γ, and β (refer to Figure 5.3):

$$c^2 = R^2 + r^2 - 2rR\cos(q - g) \tag{5.1}$$

$$\frac{c}{\sin(q-g)} = \frac{r}{\sin b} \tag{5.2}$$

$$\frac{\sin g}{\sin b} = n(l) \tag{5.3}$$

where n(λ) is the λ-dependent refractive index. Equations (5.1)-(5.3) are solved to give the values of χ and γ for any point (r,θ,ϕ); this gives, for any point (r,θ,ϕ) inside the sphere, a "corresponding" incidence point (R,γ,ϕ) on the sphere surface. The distance χ shows how much attenuation occurs in photon flux due to absorption up to that point, and γ is required for calculation of reflectivity at the surface.

5.2.2 Incidence Angle Dependent Reflectivity

As the incidence angle (γ) changes from 0 to π/2, reflectance (R_f) also changes for different polarizations of light. For any γ, R_f can be calculated using Fresnel equations if the light polarization is known. In particular, closed forms exist for parallel and perpendicular polarizations [46]. Since the solar spectrum can include any arbitrary polarization, for the calculation of R_f, we assume half of the total power is included in each extreme of polarization, and calculate $R_f(\lambda,\gamma)$ as the average of the two values for these polarizations:

$$R_f(l,g) = \frac{1}{2}\cdot\left(\frac{\sin(g-b)}{\sin(g+b)}\right)^2 + \frac{1}{2}\cdot\left(\frac{\tan(g-b)}{\tan(g+b)}\right)^2 \tag{5.4}$$

where β and γ are related through $n(\lambda)$ according to (5.3) (Snell's law). The reflectance of different polarizations is plotted in Figure 5.7 as a function of incidence angle.

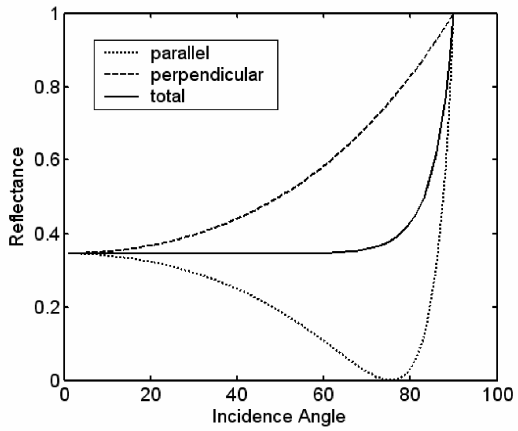

Figure 5.7: Calculated incidence angle dependent reflectance for 600 nm wavelength.

5.2.3 Generation Rate at an Arbitrary Point inside the Sphere

To find the generation rate at a point (r,θ,ϕ), the difference of the flux entering and exiting the volume element at that point is considered (Figure 5.8). The system is discretized with Δr, $\Delta\theta$ and $\Delta\phi$ steps, and the volume element is taken as a volume differential centered at the point (r,θ,ϕ) extending from $-\Delta r/2$ to $\Delta r/2$, from $-\Delta\theta/2$ to $\Delta\theta/2$ and from $-\Delta\phi/2$ to $\Delta\phi/2$ around that point. Out of the six faces of the volume element, the two constant ϕ planes do not experience photon crossing and thus do not contribute to generation rate.

To calculate the number of the photons crossing the other four faces, ΔS_1 to ΔS_4, namely Φ_1 to Φ_4 in Figure 5.8, we first find ΔS_1^* to ΔS_4^*, the optical projection of these area elements through refracted rays on the surface of the sphere (Figure 5.9). The optical projection of an area element on the sphere surface is found by projecting every point to its "corresponding" light incidence point. We next calculate the number of photons crossing ΔS_1^* to ΔS_4^* and then consider photon flux attenuation caused by absorption in Si along the optical path.

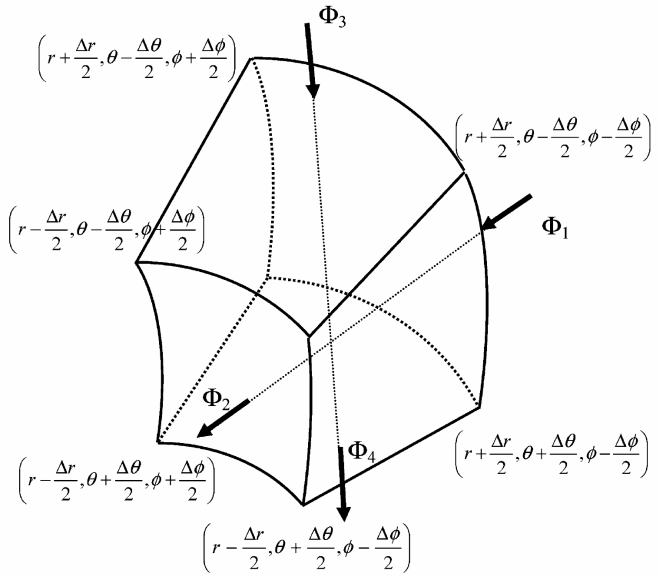

Figure 5.8: Adopted volume element centered at a point (r,θ,ϕ) with number of entering and exiting photons Φ_1 to Φ_4 at area elements ΔS_1 to ΔS_4 at constant r and constant θ; no photons pass through constant ϕ planes.

As depicted in Figure 5.9 for instance, to find Φ_1, the total number of the photons passing through a ΔS_1 face of the volume element, Φ_1^* the total number of the photons passing through the related ΔS_1* is calculated using the solar flux density and the incidence angle-dependent reflectivity $R_f(\lambda,\gamma)$. The number of photons reaching ΔS_1 is then the original number of photons entering the sphere Φ_1^* attenuated according to the absorption coefficient:

$$\Phi_i = \left[\iint_{\Delta S_i^*} S_0(l)\left[1-R_f(l,g)\right]\cos(g)\right] \exp\left[-a(l)c\right] \qquad i=1..4 \tag{5.5}$$

Where $\alpha(\lambda)$ and $S_0(\lambda)$ are the wavelength-dependent absorption coefficient and solar photon flux respectively. The numerical calculation of the integral in (5.4) is performed over the projection of the faces of the volume element and each time χ is calculated accordingly. By superimposing the results of (5.5) for the four faces and normalizing to differential volume, the generation rate is calculated from the total number of photons absorbed in the volume element:

$$G(r,q,f)=[\Phi_1+\Phi_3-\Phi_2-\Phi_4]/[r^2\sin q\,\Delta r\,\Delta q\,\Delta f] \tag{5.6}$$

Once the photogeneration at each λ and the total solar-weighted generation are calculated, the electrical model is employed to calculate the internal quantum efficiency and the device current.

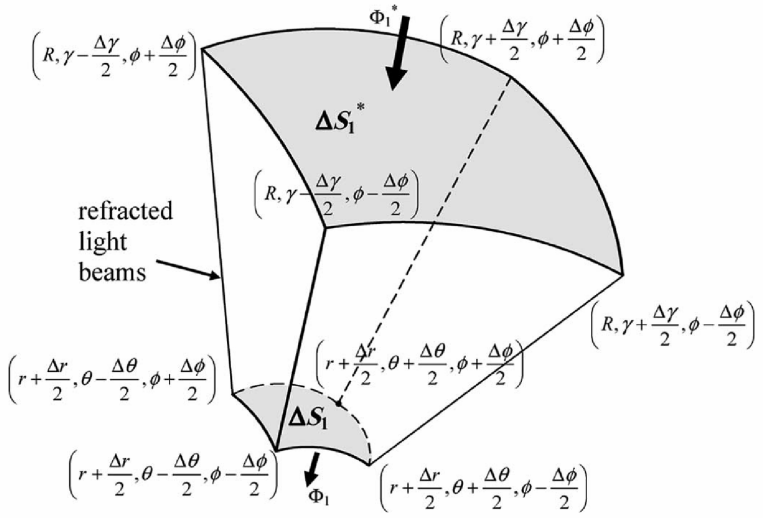

Figure 5.9: Calculation of photon fluxes by optical projection of an elemental face ΔS_1 of the volume element of Figure 5.8 obtained by projection of the points to their "corresponding" light incidence points on the surface of the sphere. Φ_1 is the photon flux crossing a face ΔS_1 of the volume element and Φ_1^* is the original entering photon flux at the sphere surface.

5.3 Development of Electrical Model

5.3.1 Device Structure Used for Electrical Model

The spherical device is modeled considering its geometry, material properties, and the diode fabrication technology. The modeled spherical device in Figure 5.10 consists of a p-type base of about 300 μm radius and a diffused n^+ emitter (1μm deep or less) with error function or uniform doping profile. As has been discussed in Section 5.1, due to the fact that the central part of the sphere contains a higher concentration of O and metallic impurities, L_n is expected to be lower there. Therefore L_n is modeled as in Figure 5.2 for device modeling purposes. The very low L_n at

the center enables us to adopt a boundary condition at the center by defining a spherical plane with near-zero radius R_o, without imposing any limit on the model. Carrier loss at this plane is modeled by a "loss recombination velocity" (L_{rv}). Since L_n is very small at the vicinity of this imaginary plane, the value of L_{rv} does not affect the calculated carrier concentration throughout the cell. We have verified this by varying L_{rv} over a wide range (10^2 to 10^5 cm/s) and observed no impact on simulation results for L_n values as high as 30 μm at a radius R_o=10 μm.

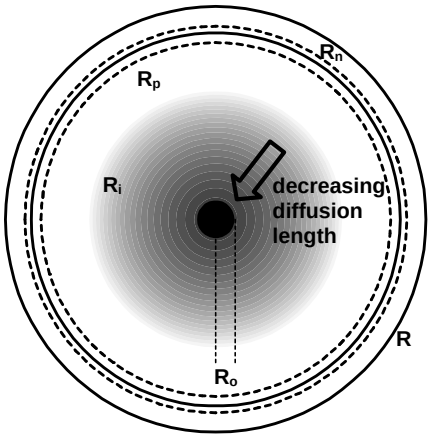

Figure 5.10: Structure of a Si sphere with boundaries for the electrical modeling.

5.3.2 Formulation of Equations and Boundary Conditions

Photocurrent from the Emitter: To analyze the emitter contribution to photocurrent, the continuity- and transport- equations are formulated in 3-D form for the spherical system of coordinates. The steady state minority hole concentration in the quasi neutral emitter can be expressed by the charge continuity equation:

$$\frac{p_{i+1\,j}+p_{i-1\,j}-2p_{i\,j}}{(dr)^2}+\frac{2}{idr}\cdot\frac{p_{i+1\,j}-p_{i-1\,j}}{2dr}+\frac{1}{(idr)^2}\cdot\frac{p_{i\,j+1}+p_{i\,j-1}-2p_{i\,j}}{(dq)^2}+\frac{1}{(idr)^2\tan(jdq)}\cdot\frac{p_{i\,j+1}-p_{i\,j-1}}{2dq}-\frac{p_{i\,j}}{L_p^2}+G=0 \quad (5.7)$$

where L_p and p are the diffusion length and excess concentration of holes. δr and δθ are the descritization steps with indices i and j. The diffused emitter has a high carrier concentration and as was mentioned in Section 3.5.3, suffers from high defect density. Thus L_p is expected to have a low value and a constant value is assumed for modeling. Solving (5.7) with appropriate boundary conditions gives δp. For this we first consider the angular boundaries which hold for both base and emitter: At axis θ = 0 and π (lines AC and AD in Figure 5.3), the two sides of the cross sectional circle are identical, implying that no current flow occurs across this axis. Therefore, the angular gradient of the carrier concentration along these axes is zero.

$$\left.\frac{\partial n}{\partial q}\right|_{q=0} = \left.\frac{\partial p}{\partial q}\right|_{q=0} = \left.\frac{\partial n}{\partial q}\right|_{q=p} = \left.\frac{\partial p}{\partial q}\right|_{q=p} = 0 \tag{5.8}$$

n is excess electron density in the base. The radial boundary conditions for the n^+-emitter are given at the surface of sphere and at SCR edge. Assuming an equipotential spherical plane at the SCR edge, for a junction voltage of V, the excess carrier density is written as,

$$p_{(r=R_n)} = \frac{n_i^{\,2}}{N_d}\left(exp\frac{eV}{kT} - 1\right) \tag{5.9}$$

where n_i and N_d are intrinsic and donor dopant concentrations. For the outer surface boundary condition a surface recombination velocity (S_{rv}) is used:

$$D_p(\nabla p)\big|_{r=R} \cdot a_n = D_p \left.\frac{\partial p}{\partial r}\right|_{r=R} = -S_{rv}.p \tag{5.10}$$

where D_p is the hole diffusion coefficient and a_n is the normal surface vector which happens to be radial unity vector $\hat{a}_r$ in this case.

Once (5.7) is solved using the above boundary conditions, the emitter contribution I_e to the total photocurrent is obtained by calculating the total current density crossing the edge of the SCR at the emitter side.

$$I_e = \left| \iint_{r=R_n} \left(\mathbf{J}_p . \hat{a}_r \right) r^2 \sin q \; dq \; df \right| = 2p\, eD_p R_n^2 \left| \sum_j \frac{p_{(R_n+dr,\, jdq)} - p_{(R_n-dr,\, jdq)}}{2dr} \sin\left(jdq \right) dq \right| \tag{5.11}$$

Photocurrent from the Space Charge Region (SCR): The contribution of SCR to the total photocurrent is found from the total generation in the SCR.

$$I_g = 2p\, e \left| \sum_i^{R_p < idr < R_n} \; \sum_j G(idr,\, jdq)(idr)^2 \sin\left(jdq \right) dq \; dr \right| \tag{5.12}$$

This is based on the assumption that photogenerated carriers are swept to the quasi neutral edge by electric field. The second diode arising from recombination through deep level traps inside the SCR is not included in this current.

Photocurrent from the Base: In the base region L_n is taken as a function of r mainly due to spatial variations of electron lifetime is in Figure 5.2. The continuity equation is thus written as:

$$\frac{n_{i+1\,j} + n_{i-1\,j} - 2n_{i\,j}}{(dr)^2} + \frac{2}{idr} \cdot \frac{n_{i+1\,j} - n_{i-1\,j}}{2dr} + \frac{1}{(idr)^2} \cdot \frac{n_{i\,j+1} + n_{i\,j-1} - 2n_{i\,j}}{(dq)^2} + \frac{1}{(idr)^2 \tan(jdq)} \cdot \frac{n_{i\,j+1} - n_{i\,j-1}}{2dq} - \frac{n_{i\,j}}{L_n^2(r)} + G = 0 \tag{5.13}$$

The angular boundary conditions are similar to those for the emitter as given by (5.8). Also, one radial boundary condition is similar to (5.9) and is written as:

$$n_{(r=R_p)} = \frac{n_i^{\,2}}{N_a} \left(exp \frac{eV}{kT} - 1 \right) \tag{5.14}$$

The second radial boundary condition is defined at the imaginary boundary very close the center. This boundary, defined as a tiny spherical surface at r = R_o, is modeled using L_{rv}, as introduced earlier in this section. The boundary condition is then written as:

$$D_n (\nabla n)\big|_{r=R_o} \cdot a_n = D_n \frac{\partial n}{\partial r}\bigg|_{r=R_O} = L_{rv} . n \tag{5.15}$$

Once (5.13) is solved for n, the contribution of the base to the photocurrent can be obtained as:

$$I_b = \left| \iint_{r=R_p} (\mathbf{J}_n . \hat{a}_r)\, r^2 \sin q \; dq \; df \right| = \\ = \left| 2p\, eD_n R_p^2 \sum_j \frac{n_{(R_p+dr,\, jdq)} - n_{(R_p-dr,\, jdq)}}{2dr} \sin(jdq)\, dq \right| \tag{5.16}$$

5.3.3 Calculation of Device Parameters and Quantum Efficiency

The photogeneration data is obtained by numerical discretization and integration of photon fluxes crossing the differential areas, using known values for n(λ) and α(λ) in equations (5.1)-(5.6). The model assumes that no antireflection coating (ARC) is present on the sphere surface. For the electrical part, the 3-D equations (5.7) and (5.13) are solved by finite difference method using the stated boundary conditions. With the partial derivatives in a spherical system, the whole structure is discretized in terms of radial and zenith angular steps with the results integrated over azimuthal range {0,2π}. The total device current is obtained from the three current components described by equations (5.11), (5.12), and (5.16). The voltage dependence of the external current is imposed through the voltage-dependent boundary conditions. Thus, the complete I-V curve of spherical cell is generated by finding I for different boundary conditions. The short circuit current density is defined based on the effective area of photon absorption, i.e. the area of the equatorial plane of the device. The zero voltage analysis at every λ yields the internal quantum efficiency (IQE).

5.4 Usability of the Developed Model for Simulation of Spherical Solar Cells

The model developed in the previous sections is implemented in a computer program to simulate and analyze the performance of spherical solar cells. The simulation tool is flexible to variations in device design and dimensions, and position dependent material parameters can be plugged in.

It should be noted the fill factors (FF) resulting from this model exclude the effect of shunt/series resistances; these parameters have significant technology dependence, and the FF calculation in the model is somewhat idealized.

Spherical devices with any set of parameters can be simulated using the developed simulation tool. As is expected, emitter response in strongly influenced by emitter surface S_{rv}. The base IQE is affected mainly by subsurface L_n as well as by the size of the denuded zone. Table I gives an example of a set of simulation parameters.

Table 5.1: Sample input parameters for spherical device simulation based on the developed model

Emitter depth (μm)	0.5
Hole lifetime[1] (μs)	0.05
Hole diffusion coeffiecient[1] (cm^2/s)	1
Emitter surface S_{rv} (cm/s)	10^3
Subsurface electron lifetime (μs)	10
Electron diffusion coeffiecient (cm^2/s)	30
Loss recombination velocity, L_{rv} (cm/s)	10^5
Denuded zone end radius, R_i (μm)	200
Radius of plane with L_{rv}, R_o (μm)	10
Emitter doping (cm^{-3})[2]	$8x10^{18}$
Base doping (cm^{-3})	10^{16}

1: Effective emitter values
2: surface concentration

5.4.1 Ramifications of Sphericity of the Device

Comparing the spherical device with a planar one highlights the difference in performance imposed by the geometrical aspects of the device. Figure 5.11 shows the IQE comparison of spherical and planar cells with identical parameters except for the geometry. The spherical cell in this case has a constant L_n throughout the base with the L_{rv} taken as the same as the back surface S_{rv} of the planar device. The spherical cell is somewhat less efficient compared to a conventional cell. This is due to the fact that the angular variations in photogeneration rate (Figure 5.5) causes a lateral (parallel to the SCR edge) carrier concentration gradient leading to an angular carrier

diffusion. The angular current component, while not contributing to the current collected at the SCR edge, forces the carriers to travel a longer path increasing their chances for recombination**.**

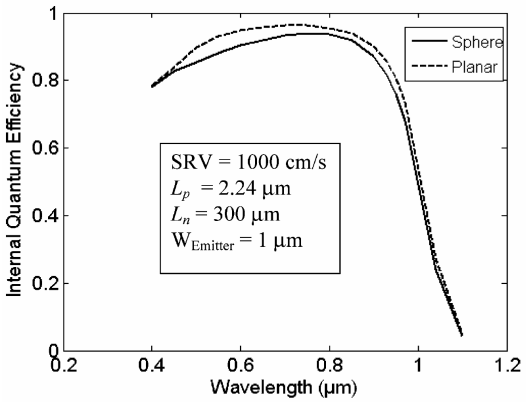

Figure 5.11: Simulated internal quantum efficiency of a spherical cell compared to a planar cell with all device and material parameters identical other than geometry.

The effect of this lateral carrier diffusion in spherical devices is demonstrated by comparing the optical and electrical behavior of differential slices of the spherical device from zero to 90^o zenith angle. Figure 5.12 shows the photon absorption and carrier collection in device sections of differential zenith angle. As θ increases, less carriers are collected per absorbed photon; this means that some generated carriers travel laterally instead of diffusing radially toward SCR edge. However, near the equatorial plane, where photon absorption drops to close to zero, electrical activity by collection of laterally diffused carriers exceeds photogeneration; this can be seen at the tail end of the two curves in Figure 5.12. Simulation results also show that in case of emitter and SCR IQE, there is no substantial difference between spherical and planar devices; this is due to the fact that emitter and SCR widths are very small compared to sphere radius, making the effect of the curvature negligible. The slightly inferior performance of spherical devices however, does not outweigh their potential cost advantages in terms of material and process simplicity, and the fact that flexible modules can be built using spherical silicon.

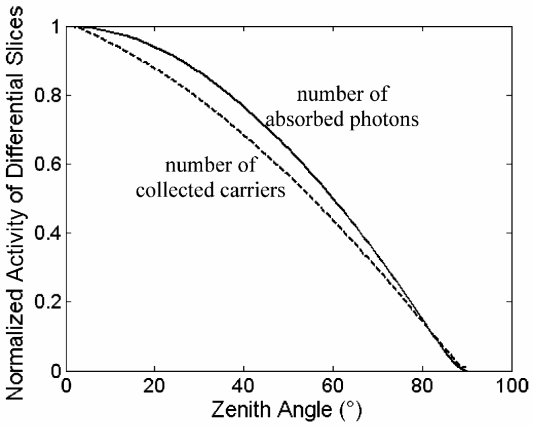

Figure 5.12: Simulated angular contribution of slices of a sphere to photo-generation and carrier collection, showing evidence of lateral carrier diffusion in a spherical diode.

5.4.2 Spherical Solar Cell Characteristics and Efficiency

The typical output of the simulation tool is the I-V characteristic and the spectral response. All the parameters of Table 5.1 as well as the emitter profile and the spatial distribution of carrier lifetime in the base can be varied. It should be noted that all the efficiency calculation is based on the cells without any antireflection coating, and 832 W/m^2 optical power [47] which is less than 1 sun.

Figure 5.13 shows the simulation results for the cell of Table 5.1 with 25.1 mA/cm^2 short circuit current density (J_{sc}) and 541.3 mV open circuit voltage (V_{oc}). Parameters that significantly affect the device performance are mainly the subsurface carrier lifetime and the depth of the denuded zone. Surface recombination velocity affects the open circuit voltage but has less significant effect on the current compared to the bulk material parameters.

Table 5.2 summarizes simulation results for several cells; the parameters not stated are similar to Table 5.1 and the error function emitter profile is assumed. The simulation results with different sets of parameters are helpful to optimize the device design and process flow of spherical cells. From fabrication viewpoint, a realistic window of parameters for spherical cells consists of

relatively deep emitters, S_{rv} varying over a range of 10^3~10^6 cm/s, denuded zone depth smaller than 200 μm, and subsurface L_n of less than 200 μm in the denuded zone.

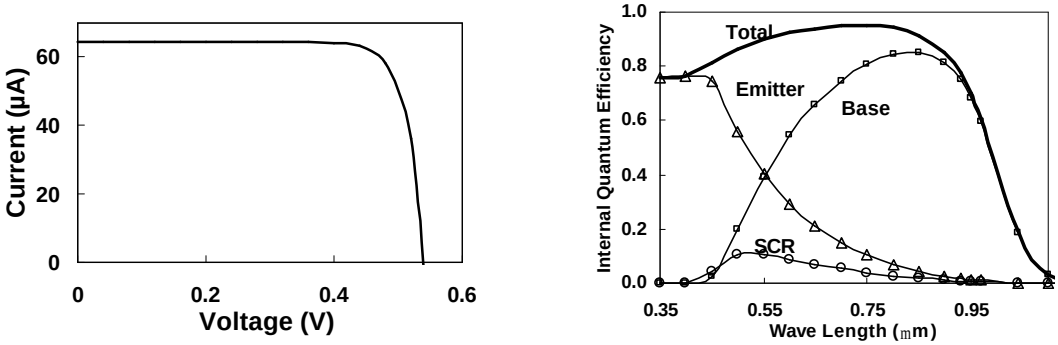

Figure 5.13: Sample output of the simulation tool; I-V curve and spectral response for the input parameter set of Table 5.1.

Table 5.2: Simulation results for several spherical silicon solar cells

Subsurface L_n (μm)	R_i (μm)	S_{rv} (cm/s)	J_{sc} (mA/cm^2)	V_{oc} (mV)	Fill Factor[1]	Efficiency[2] (%)
80	250	10^5	18.24	522.9	0.813	9.28
80	250	10^3	21.81	534.6	0.813	11.36
80	200	10^3	22.18	534.9	0.813	11.56
150	250	10^5	18.93	529.5	0.813	9.77
150	250	10^3	22.51	539.2	0.813	11.85
150	200	10^3	22.85	539.7	0.813	12.05
250	250	10^5	19.40	533.4	0.813	10.10
250	250	10^3	22.97	538.8	0.813	12.10
250	200	10^3	23.22	539.4	0.813	12.24

1: Idealized Fill Factor
2: Effciency without ARC and with 832 W/m^2 input solar power [47]

5.4.3 Silicon Sphere Growth and Device Performance

The main spherical material parameters, i.e. the subsurface diffusion length and the extent of the denuded zone, have the most significant influence on the device performance. High electronic quality in the subsurface region and deep regions of such high quality (denuded zone) result in higher efficiencies. For maximum efficiency, it is important to design, according to simulation results, the spherical crystal formation process to achieve the most effective approach.

Figure 5.14 the constant efficiency contours for cells with 1μm deep uniform emitter, 10^3 cm/s surface recombination velocity, and Gaussian profile for diffusion length degradation inside the base. The curves suggest that for a specific target efficiency, there is an optimized set of (R_i,L_n) for a fixed surface passivation quality. Also, when one parameter is limited, it imposes an upper limit on the performance of the device even if the other parameter is strongly improved. For example in Figure 5.14, given certain subsurface L_n of 170 μm, efficiency is limited to ~11% even if the denuding process is optimized to shrink the inner low quality core to close to zero.

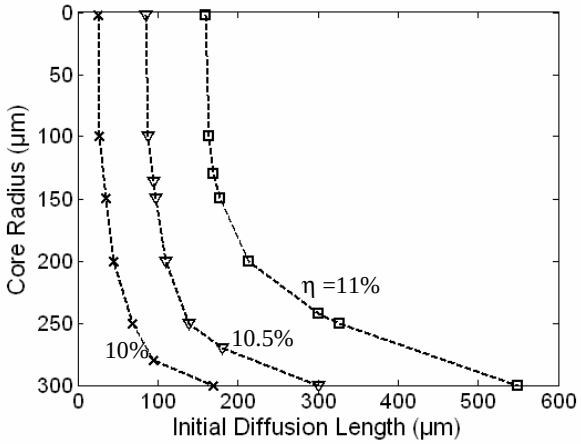

Figure 5.14: Constant efficiency curves for spherical device showing effect of radius of decaying lifetime region and the subsurface diffusion length; values at $R_i < 25$ μm are extrapolated.

Subsurface L_n is mainly determined by the effectiveness of melt/etch steps and annealing processes, whereas region of decaying L_n can be shrunk by optimizing the denuding step. Therefore, it is possible to optimize the processes for different cost or efficiency considerations according to the simulation results. For instance, the higher temperature denuding process can be to some extent shortened while prolonging the lower temperature annealing process to maintain certain efficiency.

5.6 Summary

In this chapter, a detailed optical and electrical modeling was presented for spherical *pn* junction silicon solar cells. The challenges in the device simulation as opposed to planar devices were highlighted using a 3-D numerical approach. The model has taken a realistic approach, taking into account the particular material properties imposed by the sphere formation method, geometry of the device, and the specific device structure. Simulation results on device quantum efficiency and I-V characteristics were used to provide design guidelines for advanced device design and processing.

The existing model does not include complicated optical analyses such as non-uniform angle dependent antireflection coatings or lambertian light scattering for possible future textured spheres. Also, the model excludes the effect of technologically defined parameters at the module level such as series resistance at the sphere-foil contact. In addition to the possibility of adding optical and technology-dependent features, it is also helpful to include the effect of recombination centers in the space charge region around the metallurgical junction of the device to model the second diode effect and ideality factor of the cells. For this purpose, an accurate modeling and characterization of the defects in the immediate subsurface region is required. Photoluminescence with short wavelength excitation seems to be a promising approach for this characterization.

Chapter 6

Development of Methodologies for Characterization of Spherical Photovoltaic Devices

In the previous chapter, a model was presented to simulate and predict the optoelectronic behavior of spherical devices. In order to improve the performance and also to invent new generations of spherical devices, it is crucial to acquire profound knowledge of the performance and of the limitations of the existing device. To accomplish this, in addition to the simulation tool presented in the previous chapter, detailed characterization of the spherical devices is required. Once the appropriate characterization is established, the limitations of the device will be identified and modeling can be employed to design new device structures. Further characterization of the experimentally developed devices will help improve and optimize the new structures and processes for maximum efficiency. Special approaches are required to characterize various features of the device that affect efficiency, and to assess fabrication processes.

In this chapter, characterization of the spherical devices and modules are investigated at different levels and the characteristics of the existing spherical technology are extracted. Section 6.1 presents the illuminated characterization on the module level for spherical cells which includes full module measurement and measurement on finite number of spheres by illumination through a mask. It is shown that the open circuit voltage extraction faces difficulties when the module is partially illuminated. Direct illuminated measurement of single spherical cells is discussed in

Section 6.2 along with the implemented measurement setup and the model to interpret the results. Dark characterization of spherical cells, both at the module level and at the single device level, is discussed in Section 6.3. Spectral response characterization of the spherical devices is presented in Section 6.4 along with the implemented measurement setup for this purpose.

For the different techniques and setups, the limitations and challenges at the levels of module and cell are described and analyzed. The developed approaches will play a key role in evaluating viable process developments as some examples will be presented, and are also crucial to demonstration of the effectiveness of the advanced designs of Chapter 7.

6.1 Characterization of Spherical Device Arrays

Spherical PV "modules" are arrays of pn junction diodes embedded in aluminum foils all in parallel in ordered matrices. The boron doped p-type spherical bulk is doped at the surface with phosphorous to generate an n^+-p junction. Once spherical photodiodes are complete, they are first coated with TiO_2 as an anti-reflection coating in a fluidized bed reactor. The coated spheres are next spread over a large perforated aluminum foil, where they are sucked by vacuum to rest in holes smaller than spheres. A thermo-compression is then applied to the whole module that mechanically bonds the spheres to the (front) foil through the TiO_2 coating. The tips of the spheres at the back of the device are then chemically etched so that the p-type material is accessed. At this stage, the front foil is contacting the emitter of all the diodes, and the base is exposed at the back. In the base process, the backside of the foil is then covered with an insulator polymer layer (polyimide) which goes through a mechanical abrasion step for via opening. A second foil is then applied to the bottom of the module, which provides the base contact for all the spheres as in Figure 6.1a.

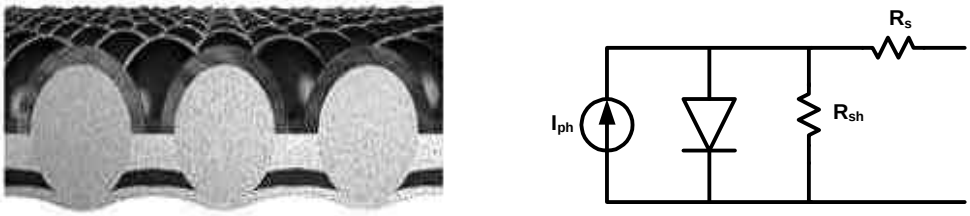

(a) (b)

Figure 6.1: Spherical solar module (a) side view schematic of devices in parallel and (b) solar cell equivalent model.

6.1.1 Spherical Module Measurements

At the finished module level measurements, the whole spherical module can be considered as a solar device with a total photocurrent I_{ph}, a (single or double) diode that represents the parallel combination of spherical junctions, and total series and shunt resistances R_s and R_{sh} which mainly affect the fill factor of the module (Figure 6.1b).

Spherical modules were produced in different sizes. The large module is a 6'x6' square. Small modules approximately 1 ½' x 1 ½' were also specifically assembled and used in our work for process development and measurement purposes. The number of the spheres in parallel per unit area of the module depends on the packing factor on the foil which is approximately 80% for the modules with flat front foil. A new design of the front foil with cup-like concentrator has been employed recently to reduce the number of spheres per module while maintaining the same optical absorption [35]. Such modules have packing factors typically less than 50% and are more efficient from the viewpoint of gram silicon per watt.

Under illumination near one sun, 6'x6' modules usually have short circuit current I_{sc} of 3~5A and open circuit voltage V_{oc} is in general in the range of 0.5~0.6 V depending on the efficiency. Figure 6.2 shows the illuminated I-V curve of a 6.56% efficient module.

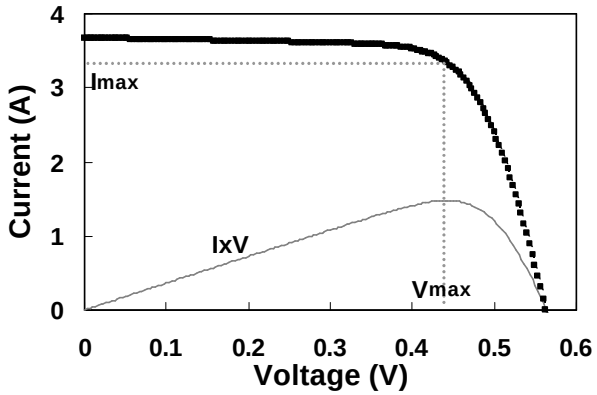

Figure 6.2: Illuminated I-V curve of a 6.56 % efficient module with the maximum power point highlighted.

The shunt and series resistances of the module are extracted from the illuminated I-V curve, as well as the fill factor and the efficiency. Since the whole module is regarded as a single cell in this case, the extracted resistances are at the module level rather than for single spheres. Output parameters corresponding to the module of Figure 6.2 are summarized in Table 6.1.

Table 6.1: Output parameters of the module of Figure 6.2

I_{sc} (A)	J_{sc} (mA/cm^2)	V_{oc} (mV)	I_{max} (A)	V_{max} (mV)	R_s (mΩ)	R_{sh} (mΩ)	FF (%)	Efficiency (%)
3.68	16.36	564.8	3.33	443.3	13.6	4722	71	6.56

The module level characterization is mainly helpful in process developments that deal with the overall output of the end product. One example of such processes is rapid thermal annealing (RTA) of the contacts to decrease the series resistance. Table 6.2 shows the results of different RTA processes on several cells. In general, temperature below 550 ^{o}C have negligible effects, and temperature above 580 ^{o}C adversely affect the shunt resistance; processes at around 575 ^{o}C for durations between 50 to 90 seconds were found to be effective in enhancing the contacts without substantially degrading the shunt resistance.

Table 6.2: Effect of rapid thermal annealing on the module performance

Cell	Process	V_{oc} (mV)	I_{sc} (A)	R_s (mΩ)	R_{sh} (mΩ)	FF (%)	Efficiecny (%)
1	As Processed	586.6	3.63	48.0	1383	52	4.92
	590 ^{o}C 20 s	561.6	3.74	32.8	781	51	4.76
2	As Processed	565.1	3.61	19.4	1756	66	5.98
	575 ^{o}C 50 s	551.2	3.89	13.6	1689	67	6.38
3	As Processed	583.3	3.96	46.1	1964	51	5.24
	550 ^{o}C 90 s	567.4	4.07	34.1	1887	51	5.23

6.1.2 On-Array Spherical Cell Measurements

Measurements connections on the finished module are realized through the two foils and will be common to all the photodiodes on the module. While the end product characterizations such as the results given in Table 6.2 are important to some module level processes, it is impossible to probe spherical cells individually. However, it is still possible to mask the module and illuminate certain number of cells through an aperture. In this case, the model of the module can be treated as parallel combination of all the single spherical cells, with photocurrents of i_{ph} and series and shunt resistances r_s and r_{sh} as in Figure 6.3. Obviously, the photocurrent of the masked cells will be zero during the measurement, and only the exposed cells will contribute to the photocurrent of the module.

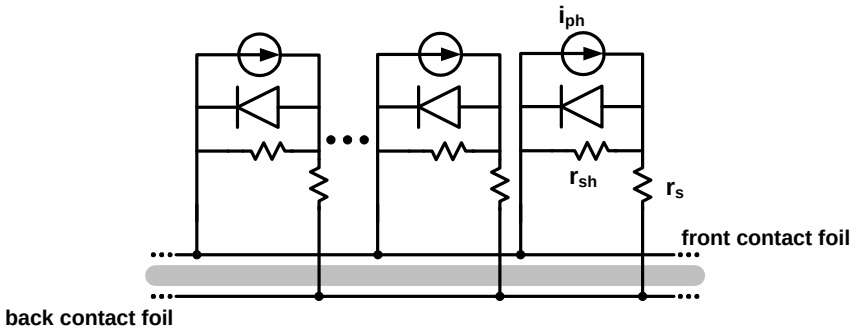

Figure 6.3: Spherical module model as a parallel combination of several cells each with photocurrent i_{ph} and series and shunt resistances r_s and r_{sh}.

Figure 6.4 depicts the dark and illuminated I-V curve of a 9.3% efficient 6'x6' module under illumination through ¼' diameter aperture, which allows approximately 29 spheres to be exposed on this module; this module uses the cup-like concentrator and has a packing factor of 43.66%. The illuminated curve reveals a quick change with the voltage (even negative voltages) due to the fact that the photocurrent is supplied by the 29 exposed spheres, whereas the open circuit voltage is affected by the shunt elements (double diodes and shunt resistances) of all the spheres on the module. Therefore, the measured open circuit voltage is not representative of the actual V_{oc} of the devices. The photocurrent is extracted from the difference between the measured dark and illuminated currents at negative voltages. By dividing this current by the number of the exposed cells, the average photocurrent of a single cell is obtained. Spherical cell current density J_{sc} is calculated by dividing the average photocurrent by the equatorial area of the spheres; the equatorial area is actually the area occupied by the sphere on the module or in other words, the effective area absorbing photons from the light source. The spheres on this cell have an average radius of approximately 390 μm, and the current density of the devices is approximately 65 mA/cm^2. The relatively high J_{sc} of the device is due to the concentrator foil which is balanced at the module level by the packing factor of the spheres. The module level current density in this case (with ¼' diameter aperture) is approximately 28 mA/cm^2.

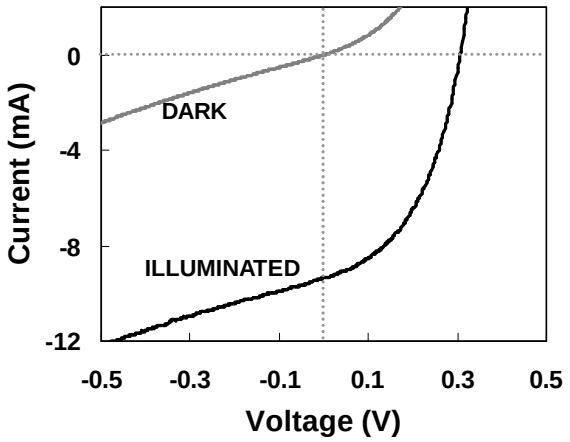

Figure 6.4: Dark and illuminated I-V characteristic of a 6'x6' 9.3% efficient module with only 29 cells exposed; low V_{oc} is due to the shunt of the masked diodes with no contribution to photocurrent.

The problem of the low voltage open circuit conditions observed in the partially illuminated module is less grave in smaller modules due to fewer dark shunt elements. This is shown in Figure 6.5 in which the illuminated curves of a 6'x6' and a small (1 ½' x 1 ½') module are compared under approximately 2 sun illuminations through an aperture of ¼' diameter. While the short circuit currents are approximately equal, the open circuit condition is reached by the small module at considerably higher voltage, 476 mV compared to 367 mV in the 6'x6' module.

The total current of a 6'x6' module is usually high, but for a small module, if the number of cells is limited and all the devices are under illumination (close to 1 sun), the equivalent V_{oc} of the devices can be estimated directly as was done in Table 6.1 for a 6'x6' module, and also the current of the module can be divided by the number of (active) cells on the module to obtain the average I_{sc} of the single spherical cells.

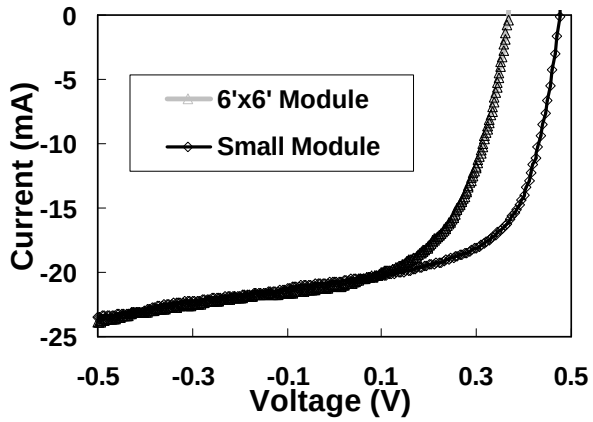

Figure 6.5: Illuminated I-V curves of 6'x6' and small modules showing the effect of dark shunt elements in the early occurrence of open circuit conditions in partially illuminated modules.

6.2 Photovoltaic Characterization of Spherical Photodiodes

The solar module characterizations of the previous section can only be performed on finished modules, and are incapable of producing information on single spherical device without interference from the other devices on the module. For developing new devices, it is desirable to characterize the cell before and after each step to evaluate the effect of different steps on the performance of the device. For some purposes such as plasma processing, it is impossible to process the finished module. Also it is often desirable to probe single devices as the phenomenon of interest might not be easily observed at the module level. In all these cases, a probing scheme that makes it possible to perform measurements on spheres individually is helpful.

6.2.1 Characterization Requirements for Advanced Device Processing

After bonding the spheres to the front foil and etching the backside to expose the p-base, it is possible to probe the pn junction as both anode and cathode are accessible. At this stage (Figure 6.6) that the module is half way complete, it is possible to modify the device using several processes. Any modification prior to this step must be symmetrical as spheres will be moving and

changing direction. Once the spheres are bonded, the directionality constraint is lifted. Yet the thermal budget must remain sufficiently low to avoid melting of aluminum and for most processes, the spheres must have no TiO_2 so that silicon surfaces on both sides of the foil are exposed. Moreover, it is possible to use plasma processing on the modules at this stage; addition of the (organic based) insulator layer, prohibits the use of plasma at any later steps.

Film deposition can be employed on the structure of Figure 6.6 for front or back surface passivation using plasma deposited silicon nitride, or to create back surface field by plasma deposition of doped amorphous silicon. Dry or wet etching can be used for emitter thinning or selective emitter. Subsurface hydrogenation processes can be designed by hydrogen plasma or annealing and hydrogen drive-in from silicon nitride films. Forming gas annealing and rapid thermal processing can be used for interface annealing or contact sintering.

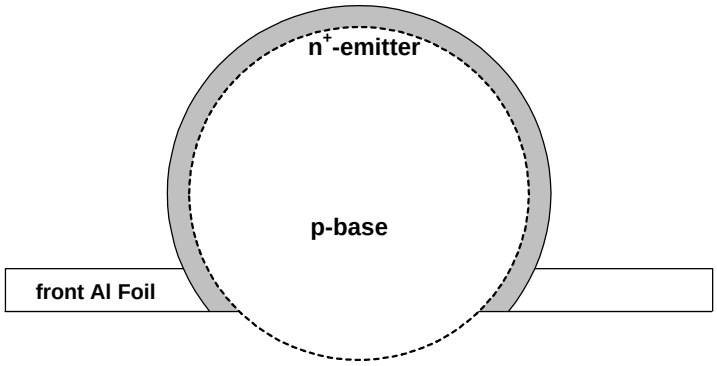

Figure 6.6: Spherical device bonded to the front foil with the base exposed by backside etching; appropriate structure for plasma and other processes with the possibility of direct cell probing.

As will be discussed in Chapter 7, when one or more of such processes are employed to process new device designs, it is important to probe the spherical devices individually before and after the process to evaluate the enhancement. For this purpose, the front foil is used as the cathode contact of the devices, and a probe is placed on the exposed anode for measurement.

6.2.2 Direct Probing of Single Spherical Solar Devices

The measurement setup for the structure of Figure 6.6 is best achieved by the device face down and illumination from bottom (Figure 6.7). In this configuration, the probe tip is properly positioned on the exposed anode for measurement. With the relatively large size of the spheres, probing is easily done. However, measurement results show that because of lack of an atomic level contact between the probe and silicon, a barrier against carrier flow forms at the probe tip.

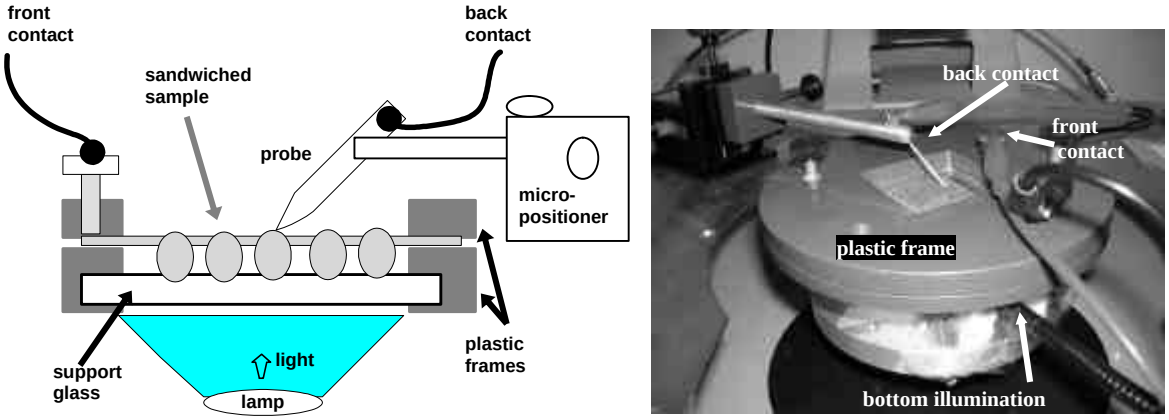

Figure 6.7: Schematic and photograph of the implemented measurement setup for I-V characterization of single spherical cells (illuminated and dark).

Figure 6.8 shows illuminated curve of a single spherical cell under approximately half sun illumination. The photocurrent of the device remains approximately constant as long as the voltage is negative. As the voltage increases, the current drops and a distorted I-V curve is observed with very small fill factor. Figure 6.9 shows the equivalent circuit model of the measured device with contact resistance r_c and a Schottky diode that models the barrier formed at the contact point of the probe tip.

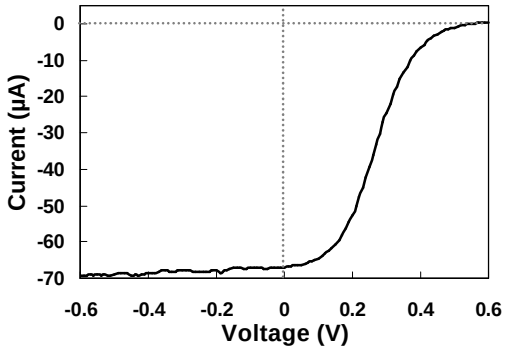

Figure 6.8: I-V curve of a single spherical cell; fill factor degraded due to potential barrier formed at the contact point of the probe tip.

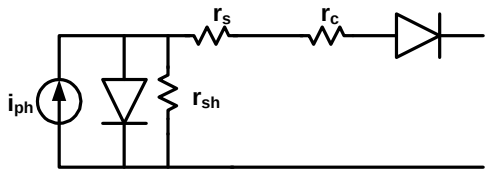

Figure 6.9: Model of the direct probing of a spherical device with the contact resistance r_c and Schottky barrier at the contact point of the probe tip.

The existence of the parasitic barrier affects the shape of the illuminated I-V curve of the devices. Yet the photocurrent of the device is directly measured when the cell is biased at negative voltages. At sufficiently negative voltages, the barrier and the other series elements do not impose a positive voltage across the internal diode of the photocell and the photocurrent flows to the external circuit which is the measurement system in this case. As the output voltage (the voltage at the cathode of the contact barrier diode) increases, the photocurrent will have to overcome a higher barrier in order to exit the device, and the output current drops. In other word, the Schottky induces a voltage across the shunt elements and this causes the current to circulate inside the cell. The voltage at which the photocurrent starts to be considerably reflected towards the shunt elements depends on the probe material and contacting force. In general, a probe with aluminum coated tip was found to result in reproducible results; for this probe, the current drop was always in the positive voltage regime.

Interestingly, the barrier problem does not cause complications for the open circuit conditions. Under open circuit condition, the current flowing to the external circuit diminishes and so does the voltage drop across the series elements. The results is that the same voltage across the shunt elements that would sink all the photocurrent internally, appears in at the output ports of the device independent of the characteristics of the barrier diode and the series contact resistance. Therefore, the I-V curve of Figure 6.8 resulting from direct probing of a single spherical cell provides information on the photocurrent and V_{oc} of the device. Table 6.3 shows the device parameters extracted from the results of Figure 6.8.

Table 6.3: Output parameters of the spherical cell of Figure 6.8

i_{sc} (μA)	J_{sc} (mA/cm^2)	V_{oc} (mV)
66.9	20.80	551.6

The lamp used for illumination for the probing of single cells provides approximately half sun power. Thus the measured values are not under 6'x6' conditions, but are sufficient for comparative study of cell performance before and after a process step. Unfortunately, it is not possible to characterize the series resistance of the device at this stage as the Schottky barrier appears to be the dominant series component. Curve fitting based on the model of Figure 6.9 can be employed to extract parameters. However, it is impossible to separate r_s from other series impedances with a single measurement, and multiple measurements are not helpful as the diode characteristics and r_c change every time the probe is lifted and placed again on the device.

6.3 Dark Characterization of Spherical Photodiodes

Dark characterization can be used to evaluate the single or double internal diode of the device [39] which plays an important role in limiting V_{oc}. The dark diode characteristics are measured both at the module level and for single devices. The size of the module determines the number of

diodes in parallel to be measured and thus the dark current for a 6'x6' module is usually high. On the other hand, it is often desirable to measure the dark current with high precision measurement systems; such systems have a maximum compliance, and are saturated when measuring large area devices. Therefore, small modules are preferred for dark characterizations, as a wider voltage range can be covered.

Figure 6.10 shows the dark I-V curves of the 6'x6' and small module of Figure 6.5. The reverse current is usually dominated by the shunt resistance of the device. In the forward regime, the 6'x6' module reaches the maximum current compliance of the system used for dark measurement (100 mA) before different regions of the diode characteristics regarding space charge region and quasi neutral region are observed.

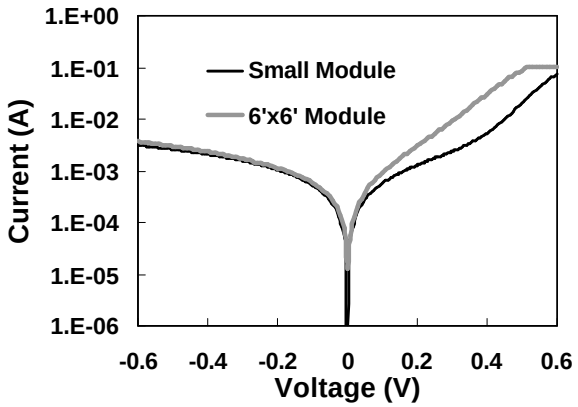

Figure 6.10: Dark I-V characteristics of a 6'x6' and a small spherical module; the 6'x6' module has reached the maximum compliance of 100 mA.

From the dark curve of the small module replotted in Figure 6.11, it is possible to define the different regimes of the diode characteristics corresponding to the parallel combination of all the spherical diodes on the foil. The space charge region (SCR) seems to dominate over a wide range of voltages below 0.4 V, and the dark series resistance dominates above 0.6 V. In between, the quasi neutral region (QNR) plays the main role in shaping the dark characteristic. The

corresponding saturation currents can be extracted for a double diode model of the spherical module based on the extrapolation of the slopes of the different dominant recombination regimes in the diodes.

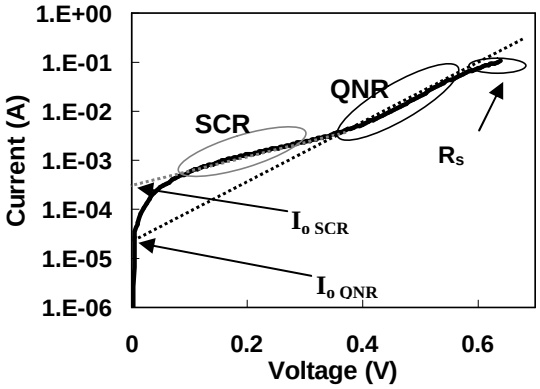

Figure 6.11: Dark I-V characteristics of a small spherical module with different diode regimes and saturation currents indicated.

The dark characteristics of a single spherical diode probed directly as described in Section 6.2.2 is significantly affected by the Schottky barrier. Figure 6.12 shows the dark diode characteristics of the spherical cell of Figure 6.8. The different regimes of the diode current are masked by the early dominance of the series limiting components which is distinguishable even before 0.4 V. The initial linear slope can still be used to extrapolate the space charge region saturation current. The Schottky barrier effect in the case is not considerable as the current is small and little voltage drop is caused by the barrier. In general, the illuminated I-V is more vulnerable to the series barrier due to the fact that currents of much greater orders flow and an additional voltage drop is induced due to the internal photocurrent of the Schottky barrier.

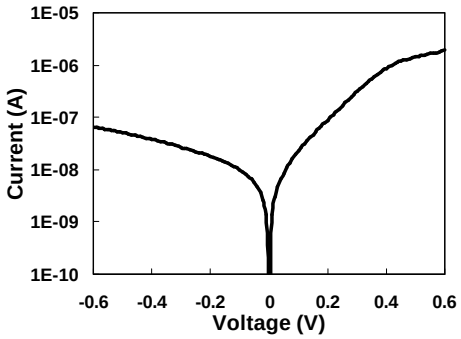

Figure 6.12: Dark I-V of a single spherical diode with series path dominating even below 0.4 V.

6.4 Spectral Response of Spherical Photodiodes

The internal and external quantum efficiencies (IQE and EQE) of a solar cell are in fact the main factors determining the conversion efficiency. Characterizing the quantum efficiency is a powerful tool that provides information on different aspects of the device. As was shown by the simulation results in Section 5.4.2, the spectral response (SR) of a photodiode is influenced by the different regions of the device; the short wavelengths SR mainly contains information on the emitter and some information on the base can be extracted from long wavelengths SR.

The optical power of the monochromatic light in SR characterization is small compared to the illuminations used for I-V measurements, and module measurements are easier as the current level is low. Moreover, the device is operated close to the short circuit conditions for SR characterization, and the measurement at module and cell levels are equally accurate since the number of shunt elements on the module or the series barrier of probing have minimal effect on the current at short circuit. However, probing of single photodiodes for SR measurement is more complicated than illuminated I-V probing. Since the monochromatic light is directed horizontally, the device mounting must be done vertically (Figure 6.13). This can lead to poor contacting by the probe tip, or loss of contact due to vibration. For repeatable measurements, a silver paste was

applied to the back of the single devices (the bottom tip of the sphere in Figure 6.6) and baked to act as a contact pad for better connectivity during the measurement.

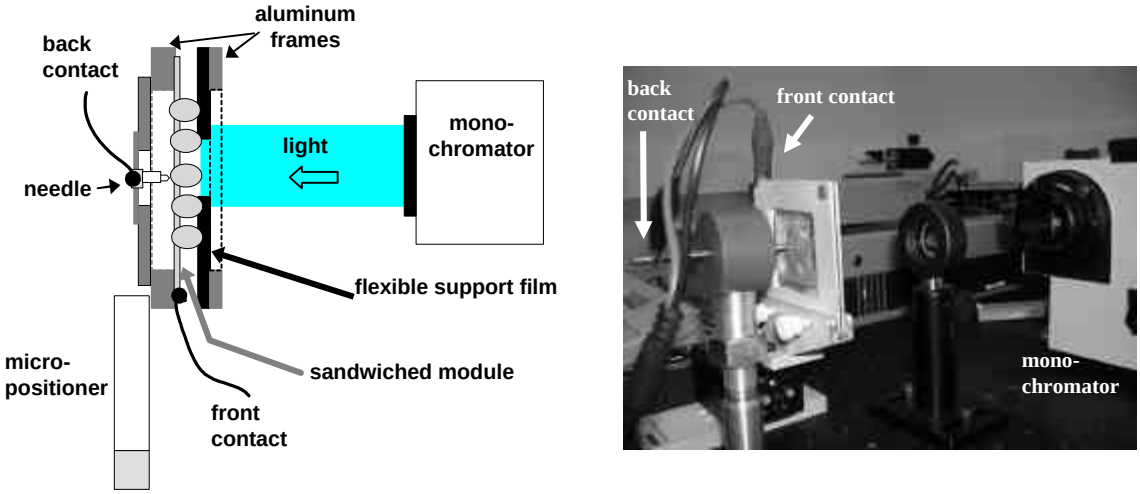

Figure 6.13: Schematic and photograph of the implemented measurement setup for spectral response characterization of single spherical photodiodes.

Figure 6.14 shows the spectral response of a 9.3% efficient 6'x6' module, calibrated according to the response of a 6'x6' commercial photodetector, and normalized to cancel the effect of cell area coverage on the module. Normalization is required as the spot size of the monochromatic light is small (0.5 mm x 3 mm approximately), and alignment of the beam on the module/device area has a great impact on the electronic signal detected by the lock-in amplifier.

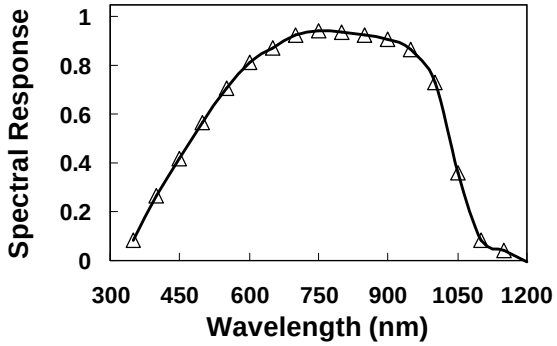

Figure 6.14: Normalized spectral response of a 6'x6' 9.3% efficient module.

As Figure 6.14 reveals the spherical cells appear to suffer from poor blue response. This is due to deep emitter junctions and poor surface quality of the device as was mentioned in Section 5.5, and will be the basis to the advanced designs for surface passivated and selective emitter spherical devices in Chapter 7.

It must be noted that the information provided by the normalized SR curve of Figure 6.14 is not the actual IQE of the spherical photodiode; yet the spectral distribution of quantum efficiency and the blue response can be interpreted to characterize the surface and emitter properties of the cells. The actual efficiency and the total current of the cells are better characterized using the illuminated curves of Sections 6.1 and 6.2.

6.4 Summary

The illuminated and dark characteristics of spherical devices were characterized at the module level and as single devices using different setups. The illuminated curves can be used to extract the J_{sc} and V_{oc} of spherical solar end product modules, as well as single cells; the dark characteristics show the saturation current and other diode properties of the device.

The characterization results can be interpreted to extract device parameters, to evaluate the device performance, and to assess the effectiveness of the advanced processes developed for new device designs. Together with the modeling tool of Chapter 5, the characterization will be used for the designs of the new spherical device structures in Chapter 7.

Development of contacting scheme for probing of single spherical devices without Schottky barriers is important for further characterizations, especially when series resistance of the device is of interest. The ability to extract and monitor the series resistance is beneficial in the design considerations regarding spherical bulk resistivity and emitter sheet resistance. Coating the probe with aluminum enhanced the contacting to some extent. Silver paste contacting was not able to

overcome the barrier although it facilitated probing in the vertical position. Aluminum deposition through shadow masking was tested and was found difficult to avoid shorting, especially for the backside that only a small area of the sphere is exposed; the deposition was successful on the front side for some other experiments that were designed for DLTS measurements.

For real lab scale measurements, in addition to probe contacting without Schottky, it is important to bond single sphere to aluminum foils, which can be as small as 1 cm in dimensions. This is to avoid the presence of shunt elements of other spherical diodes during the measurement of a single device.

Chapter 7

Design and Fabrication of Advanced Spherical Photovoltaic Devices

Spherical silicon is an approach to combine low cost feedstock with superior performance of single crystal for solar energy conversion. Spheres are made form silicon feedstock that is inappropriate for microelectronic industry. Given the current shortage in silicon supplies, spherical solar technology has proved to be promising for the future of photovoltaic systems. However, shipment, installation, and related labor currently constitute a great portion of PV systems costs, and the trend is changing from low cost device fabrication to maximum efficiency module manufacturing. Therefore, it is important to enhance the efficiency of the existing devices, as well as to design new high efficiency device structures.

The simulation tool and the characterization of the device performance discussed in the two previous chapters provide the necessary tools to identify the limitations of the existing devices as basis for approaches to device improvement and new designs. Given the manufacturing issues in the spherical technology, technological constraints beyond the device and the electronics must be also considered.

Based on the modeling results and technology features and limitations, some viable processes and advanced device designs are proposed in this chapter. The significance of surface passivation is

discussed in Section 7.1 along with some experimental surface passivation attempts. A plasma deposited silicon nitride film is developed for the passivation of spherical devices. However, it is found that with the existing deep emitter devices, surface passivation has minimal effect on the efficiency enhancement. Based on the results of Section 7.1, different approaches are pursued in Section 7.2 to fabricate shallow emitter devices without compromising the yield during the front foil bonding, where devices are likely to be shorted by aluminum spikes through shallow emitters. Silicon (isotropic) wet etching is used to thin deep emitters after bonding. Yet the increase in the sheet resistance of the emitter is found to counteract enhanced photocurrent in thinned emitter devices. In Section 7.3, a dry etch process is developed using reactive ion etching, in which the emitter is etched back in a non-uniform manner, creating a selective emitter. The selective emitter sheet is shallow enough to allow passing of photons at the top of the sphere, while it remains thicker (with less resistance) in the areas that greater current flows (on the sides). Together with the passivation scheme developed in Section 7.1, the selective emitter is shown to have superior performance compared to deep emitter and uniformly thinned emitter spherical cells.

7.1 Surface Passivation of Spherical Devices

Surfaces and interfaces in semiconductor lattice introduce a major distortion to the periodicity and thus create defects within the semiconductor bandgap known as interface defects or traps. In fact, dangling bonds at the surface increase the rate of recombination at the surface/interface which is known as surface recombination velocity (SRV). It was shown in the simulation results of the previous chapter that high surface recombination velocity degrades the cell efficiency in the device. In this section, a surface passivation technique using silicon nitride is used to enhance the cell efficiency.

7.1.1 Significance of Surface Passivation

As can be seen in the simulation results of Section 5.4.2, the surface recombination of the device affects the performance of the cell and for improved efficiency, the surface recombination velocity (SRV) must be reduced [48]. The effect of low surface recombination is partially due to the increase in the photocurrent of the device. Photogenerated holes in the emitter have a chance of recombining with the electrons at the interface. Passivation suppresses this phenomenon, and as a result, the emitter supplies a larger population of holes to be injected to the base. This is most significant for the carriers generated close to the surface. Since the short wavelength photons are immediately absorbed after entering the silicon medium, a device with passivated surface shows superior blue response in the quantum efficiency. Figure 7.1 depicts the simulation results for emitter blue response with different passivation qualities in a device with 0.5 μm deep emitter and uniform doping density of $5x10^{18}$ cm^{-3}.

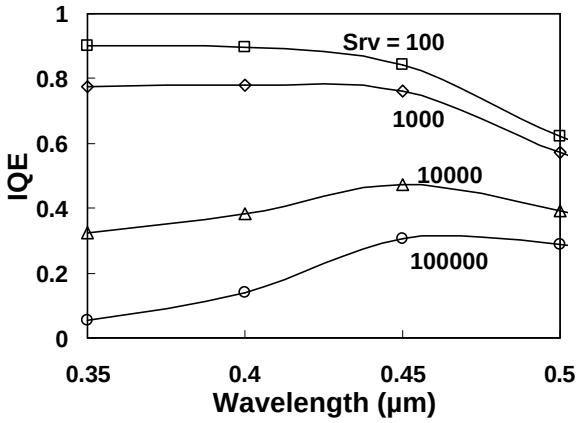

Figure 7.1: Simulated emitter blue response for different surface recombination velocities.

In addition to enhanced photocurrent, and more considerably, surface passivation increases the open circuit voltage of the device as the results of simulation in Figure 6.2 show for two different depths of emitter with error function profile. This is mainly due to the fact that the saturation

current of the device is considerably decreased after passivation. The increase in V_{oc} is more effective in shallow emitters where the surface recombination directly influences the carrier distribution at the edge of the space charge region (SCR). The deeper the metallurgical junction, the more separated would be the effect of surface from the space charge region.

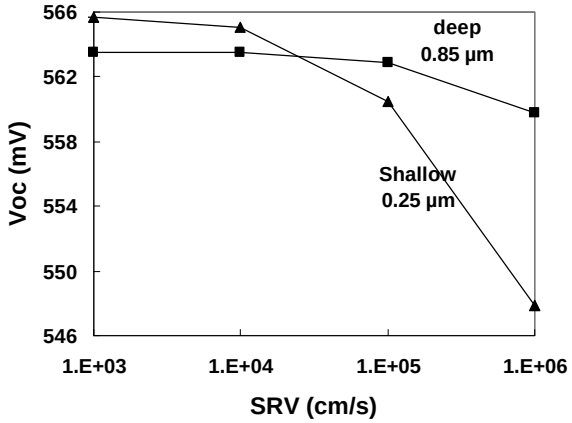

Figure 7.2: Simulation results of open circuit voltage variations with surface recombination for shallow and deep emitter devices.

7.1.2 Surface Conditions of Current Spherical Devices

The measured spectral response of spherical cells (even for relatively high quality cells similar to that of Figure 6.14) reveals poor blue response of the devices. Comparing the experimental curves with simulation results (such as Figure 5.13 for a cell with 10^3 cm/s SRV) shows that the response of an actual device is close to the base response in the simulated device; this implies the emitter response and the SCR response are weak. Since the emitter response is mainly affected by the surface recombination it can be concluded that the devices suffer from very high surface recombination velocity. This is mainly because the spherical devices are embedded on the foil directly after the phosphosilicate glass formed during diffusion is removed or after vapor deposition of TiO_2 in a fluidized bed. While the results of simulation (Figure 7.1) suggest that a

simple passivation to decrease SRV to below 10^4 cm/s can significantly improve the efficiency of the spherical cells, the bare silicon surface or the interface with TiO_2 form indeed unpassivated surfaces where SRV can be as high as 10^6 cm/s at the high surface concentrations after a typical diffusion step.

7.1.3 Surface Treatment through TiO_2 Coating Annealing

After the diffusion step for the formation of the n^+-emitter is complete, the surface of the spherical diodes can be coated with TiO_2 in a fluidized bed reactor. This layer is added as an anti-reflection coating (ARC) to reduce optical loss due to high reflection of silicon. The spheres are then bonded to the front foil through this layer, and are etched at the backside of the foil to expose the p-base by removing the TiO_2 layer and n^+-emitter.

The ARC increases the photocurrent of the device, and slightly enhances V_{oc} as a result. The V_{oc} can be further enhanced by reducing SRV through treating TiO_2/Si interface at high temperature [49]. In order to achieve this, the TiO_2 coated spherical cells were annealed at 750 ^oC for 10 minutes. The cells were then assembled to test modules for measurement. The results summarized in Table 7.1 show that with identical bonding procedure for all cells, leading to similar series and shunt elements, the annealed cells enjoy higher V_{oc}. The fact that short circuit currents are approximately equal implies that the enhancement in V_{oc} is mainly the result of reduction in saturation current due to slower surface recombination. Thus it can be concluded that the high temperature treatment has a great impact on the surface recombination velocity of the devices.

Interestingly, inclusion of oxygen in the annealing ambient enhances the passivation achieved at the TiO_2/Si interface. This is believed to be due to transport of oxygen through the TiO_2 layer to the interface and deactivation of Si dangling bonds [49].

Table 7.1: Effect of high temperature treatment of TiO_2/Si on the performance of spherical cells.

Annealing Conditions	I_{sc} (μA)	J_{sc} (mA/cm^2)	V_{oc} (mV)
NO Anneal	152.6	28.48	551.2
100% N_2	154.0	28.74	566.6
67% N_2 : 33% O_2	152.1	28.38	581.8
50% N_2 : 50% O_2	153.2	28.59	581.6

7.1.4 Process Development for Passivation of Spherical Cells

The TiO_2/Si interface annealing in oxygen ambient is helpful in suppressing surface recombination and can be easily integrated to the existing process flow for the fabrication of spherical cells. However, other processes for high quality interface can be developed to maximize V_{oc} and efficiency of the cells. High temperature silicon dioxide growth and deposited silicon nitride layers are commonly used in conventional photovoltaic cells for surface passivation.

Once the emitter diffusion in finished and the phosphosilicate glass is removed, prior to coating the spheres with TiO_2, it is possible to grow thermal oxide at the surface of the spheres. TiO_2 may or may not be applied to the spheres. In either case, the spheres will be bonded to the aluminum foil as usual and fabrication process can continue with SiO_2 covered spheres as in Figure 7.3a.

We used rapid thermal oxidation (RTO) for the purpose of surface passivation of the spheres. RTO can be easily replaced by belt furnace in an industrial scale process for high throughput. The spheres were oxidized at 950~1050 ^oC for 10~120 seconds, and the thickness control was performed by adopting the RTO growth rates on planar wafers measured by spectroscopic ellipsometry. Although the spheres were successfully bonded to the foil even in the case of thick oxide layers (10 nm), the bulk degradation of the spherical material deteriorates the device performance. This degradation that adversely affects the carrier lifetime as was discussed in detail in Section 4.2.2 is a serious draw-back in applying thermal oxide on spheres as any defect creation/activation must be avoided.

An alternative approach is plasma enhanced chemical vapor deposition (PECVD) of silicon nitride (SiN) [50]. PECVD nitride is widely used in industry and is known as a large area technique. The deposition can be performed after the spheres are bonded to the front foil directly after removal of phosphosilicate glass of the diffusion step and without TiO_2 coating as in Figure 7.3b. Since the foil material is aluminum, and the organic insulator layer has not yet been added at this stage, the plasma processing can be easily implemented. With the PECVD nitride formed at temperatures typically below 400 ^oC, the risk of activating defects in the bulk while passivating the surface disappears. Also the processing temperature is low enough for the aluminum foil and the absence of the TiO_2 is no concern as the nitride layer serves as ARC for the device.

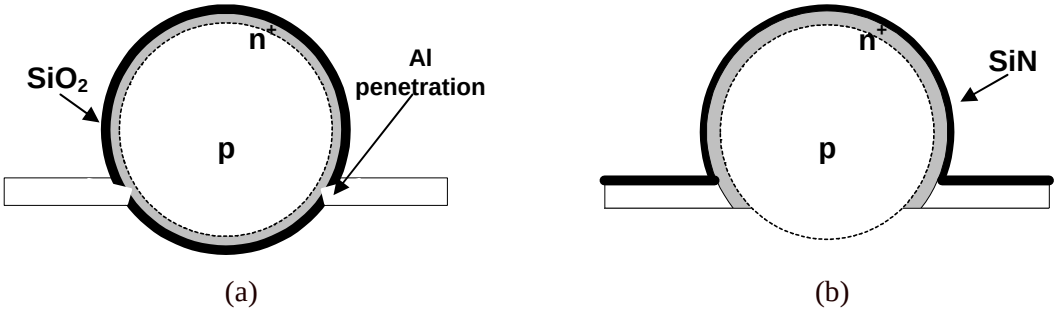

(a) (b)

Figure 7.3: Surface passivation layers for spheres (a) thermal oxide before bonding of front foil with Al penetration through oxide during bonding (b) nitride deposition after bonding.

7.1.5 Plasma Enhanced Chemical Vapor Deposition of Silicon Nitride

The development of PECVD nitride was performed on planar 100 Si wafers. The films were deposited with a 13.56 MHz radio frequency power supply at pressures ranging from 100 to 300 mTorr. The deposition temperature was 250~350 ^oC, and the power density was limited between 7 to 20 mW/cm^2 for low surface damage at the initial stage of deposition. The gas precursors used for deposition were silane, ammonia, and hydrogen.

Deposition rates and hydrogen contents were extracted for process development purposes. The deposition rate was measured by patterning the nitride films and measuring the height of the steps using a surface profilometer. The hydrogen content of the films was extracted using Fourier transform infrared spectroscopy (FTIR) [51]. The process was developed to ensure considerable hydrogen content which was found to be effective in the passivation of electronic states at the interface.

The passivation quality of the films was characterized by carrier lifetime measurement using microwave photoconductivity decay (μ-PCD); the equivalent surface recombination lifetime was estimated from the comparison of carrier lifetimes of the bare Czochralski silicon wafers immersed in passivating solution and on nitride passivated wafers.

Hydrogen pretreatment (wetting) of the surface prior to the actual film deposition for approximately 5 minutes was used to enhance the interface quality. It was found that surface recombination increases as the hydrogen content of the film decreases as a result of hydrogen precursor gas inclusion during deposition. The deposition temperature and the film composition were also found to have a great impact on the passivation quality. The film composition, i.e. the atomic ratio of silicon and nitrogen is mainly controlled by the silane to ammonia gas flow ratio. Figure 7.4 shows the deposition temperature dependence of surface recombination lifetime for two gas flow ratios with no hydrogen included in order to achieve maximum hydrogen concentration in the film and at the vicinity of Si/SiN interface.

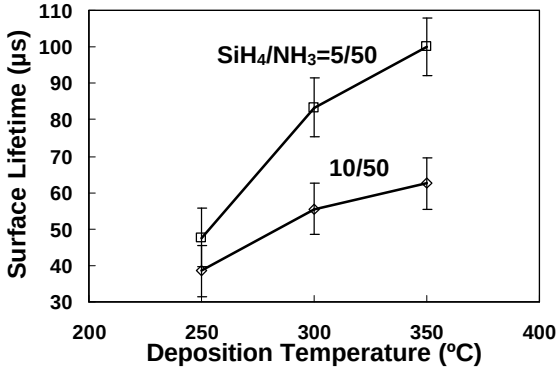

Figure 7.4: Variation of surface recombination lifetime (measured on Cz) wafers with deposition temperature and silane to ammonia gas flow ratio.

Annealing at different temperatures ranging from 375 to 450 ^{o}C for 15 minutes was also performed to enhance the interface quality. In general, nitride films deposited at lower temperature show considerable improvement after annealing. The films with higher deposition temperature show less improvement (and even degradation in some cases) in spite of the high as-deposited passivation quality as is depicted in Figure 7.5. It can be concluded that the two mechanisms of interface treatment with thermal energy and hydrogen effusion from the film both affect the interface quality and while temperature helps the annealing of some defects, some hydrogen-silicon bonds break at the interface leaving dangling Si bonds that create energy traps in the bandgap and speed up carrier recombination.

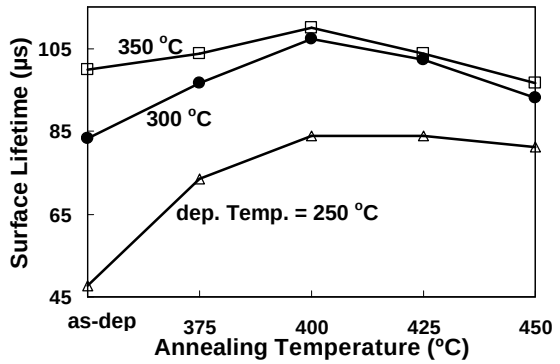

Figure 7.5: Effect of annealing on surface recombination lifetime of nitride passivated interfaces.

7.1.6 Characterization of PECVD Nitride Coated Spherical Cells

PECVD nitride was deposited on to spherical cells with the conditions given in Table 7.2. The deposition rate for this set of conditions is 5.1 nm/min and the resulting film has a thickness of approximately 65 nm. Hydrogen wetting was used prior to deposition, and the film was annealed at 410 ^{o}C for 15 minute after deposition. The illuminated I-V of the devices was measured before and after nitride passivation. Figure 7.6 shows the results of direct probing of the spherical devices bonded to the front foil with illumination from the bottom. Both I_{sc} and V_{oc} show improvement in this case as is summarized in Table 7.3. Although it seems that the passivation nitride layer has improved the device characteristics, more detailed analysis shows that the improvement is not in fact from the passivation effect of the nitride.

Table 7.2: Process conditions for PECVD nitride deposition

Time (min)	Pressure (mTorr)	Temperature (^{o}C)	Power (W)	SiH_4 (sccm)	NH_3 (sccm)
13	250	300	12	5	50

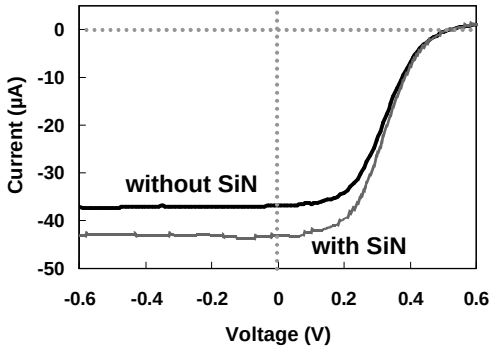

Figure 7.6: Illuminated I-V of the spherical device measured before and after PECVD nitride deposition.

Table 7.3: Cell parameters before and after nitride deposition

	I_{sc} (μA)	V_{oc} (mV)
without SiN	36.88	523.5
with SiN	43.10	526.6

While trying to reduce the surface recombination with a nitride film, an enhanced photocurrent is actually observed due to the antireflection effect of the thin film. Normalized spectral response characterization (Figure 7.7) clearly reveals that the blue response of the device has not been considerably affected by nitride deposition in contrast to the prediction by simulation results (Figure 7.1). The increase in the current and the voltage is therefore only due to the external quantum efficiency improvement as a results of reduced reflection loss.

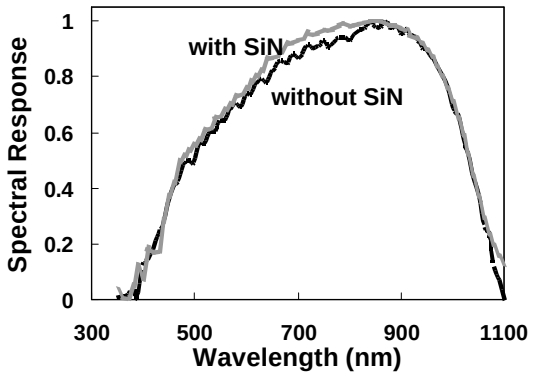

Figure 7.7: Normalized spectral response of the spherical device measured before and after PECVD nitride deposition.

Although the nitride deposition with the conditions of Table 7.2 is definitely leading to a better interface quality compared to the case of bare silicon surface, as proven by the interface characterization on planar wafers, the characteristic of the spherical device is not benefiting from the reduced surface recombination. The reason, which can also be inferred from simulation results of Figure 7.2, is the fact that the emitter in the spherical devices is too deep, and the short diffusion length of the carriers leads to poor blue response even though they escape the recombination through the defect energy states at the interface. In order to significantly increase the efficiency of the device by surface passivation, shallow emitter devices must be designed so that the effect of low surface recombination reflects in improvement of photocurrent as well as suppression of saturation current.

7.2 Shallow Emitter Spherical Cells

The emitter design has a significant impact on the efficiency of spherical cells. Deep emitters are generally avoided in silicon cells as they absorb a considerable portion of the solar photons and the high carrier concentration causes poor carrier collection efficiency due to short diffusion. Moreover, it was shown in the previous section that the nitride passivation will not effectively enhance the device efficiency as long as the emitter depth is not optimized. The challenges and approaches for shallow emitter design will be discussed in this section.

7.2.1 Effect of Emitter Depth on Cell Performance

The emitter region of spherical cells is fabricated by a high temperature diffusion step and has a high carrier concentration. The introduction of a high density of guest atoms in the lattice and the presence of carriers in high concentrations lead to high Shockley-Reed-Hall and especially Auger recombination rates. As a consequence, the carrier lifetime is short and most of the photogenerated holes in the emitter cannot reach the space charge region to drift to the base (even when they escape the surface recombination) if the emitter is deep. Figure 7.8 shows the change in the photocurrent of simulated spherical cells with different diffused junction depth (error function profile) and SRV of 10^4 cm/s.

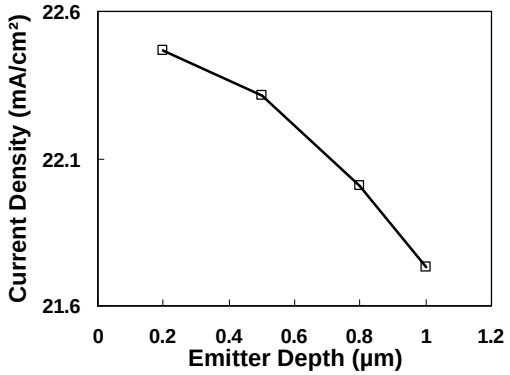

Figure 7.8: Simulated photocurrent of spherical cells with different diffused junction depths.

The increased photocurrent of shallow emitter cells will naturally tend to increase V_{oc} of the device. Yet this is subject to the surface quality. The saturation current of shallow junction devices is more sensitive to SRV and might increase faster than the photocurrent with downsizing of emitter. Figure 7.9 show the V_{oc} as a function of emitter depth (error function profile doping) for spherical cells with different surface qualities. Apparently, any design for shallow junction devices must be accompanied by a passivation step in order to reach high efficiency, or the photocurrent enhancement will be counterbalanced by the V_{oc} degradation.

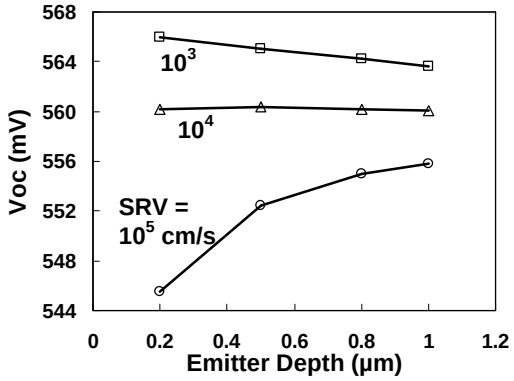

Figure 7.9: Simulated photocurrent of spherical cells with different diffused junction depths.

7.2.2 Deep Emitter Constraint of Spherical Devices

In general, the diffusion step in spherical cells is critical and needs optimization for maximum yield and maximum efficiency. For the front aluminum contact to the outer n^+ emitter layer, the cells undergo a thermo-mechanical step to bond into the perforated foil. To obtain a mechanically stable and electrically conductive contact, pressure is applied at temperatures around 400 ^oC to attach the spheres that are physically separate from the aluminum foil. Due to the mechanical pressure and relatively high temperature, aluminum is likely to spike into silicon, and the Si-Al contact interface may penetrate deep into the emitter. Furthermore, the proceeding steps of curing of the insulator and bonding and sintering of the second aluminum foil for p-base contact are

performed at higher temperatures (which may exceed 500^{o}C for durations more than 10 minutes), increasing the chance of deeper Al-spikes into the bulk of the sphere; this is mainly due to segregation of silicon into aluminum which occurs even far below the eutectic point.

If aluminum passes through the emitter layer, it will short the junction and a shunted device forms. Shunted devices will be electrochemically isolated from the module later and will not cause module failure. Yet the shorted diode, while occupying area on the surface of the module, does not contribute to the current and thus reduces the active area and effective fill factor on the module area. Therefore, low yield in the front contact step will adversely affect the efficiency. To avoid this, the n^{+} diffusion in the spherical pn junctions is designed to result in a deep emitter compared to standard planar silicon cells as in Figure 7.10.

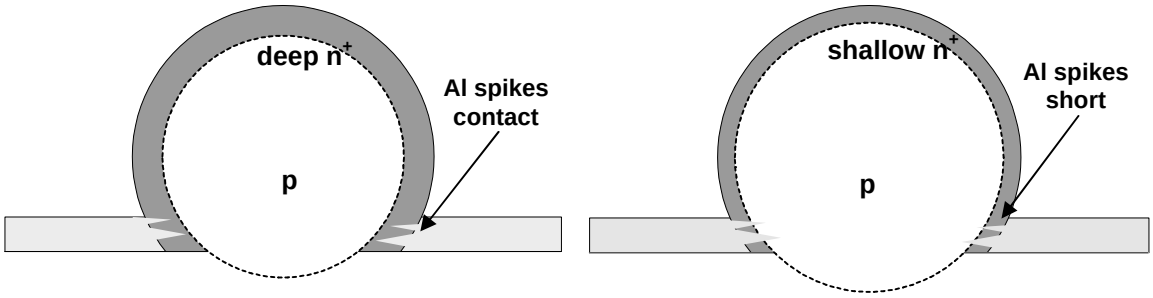

Figure 7.10: Aluminum spikes into silicon spheres during bonding (a) n-contacting in deep emitter (b) shorting junction in shallow emitter.

7.2.3 Fabrication of Shallow and Deep Diffusion Devices

To experimentally explore the possibility of achieving high efficiency by allowing a wide window of the solar spectrum to pass through the less efficient emitter and reach the base, spherical devices with different junction depths were fabricated. The phosphorous diffusions were performed at 900 ^{o}C for 60 and 120 minutes and the spheres were assembled to modules afterwards. For the bonding of the spheres on the front foil, two different pressures were tried. It

is worth noting that the regular diffusion step, designed to avoid shunted diodes, normally consists of two diffusions at 925~950 ^{o}C each for 45~60 minutes with the phosphosilicate glass removed between the two.

Table 7.4 shows the results of I-V characterization of test modules manufactured from similar spheres and different diffusions. The shallow emitter devices enjoy from higher J_{sc}, but the number of shunted devices increases due to aluminum shorting of the junction as was explained in the previous section. Moreover, in spite of higher J_{sc}, the output voltage is lower in the shallow junction devices. This is due to the fact that no passivation is employed on the measured devices and high SRV leads to high saturation current and poor V_{oc}.

Table 7.4: J_{sc}, V_{oc} and yield of spherical cells for different phosphorous diffusions at 900 ^{o}C

Diffusion Time (min)	Bonding Conditions	I_{sc} (μA)	J_{sc} (mA/cm^2)	V_{oc} (mV)	Shunted Cells (%)
60	1	145.8	23.44	536.2	7
	2	145.3	23.36	549.3	13
	Average	145.6	23.40	542.8	10
120	1	136.5	21.94	545.9	6
	2	136.8	21.99	554.7	11
	Average	136.7	21.97	550.3	8.5

7.2.4 Emitter Thinning of Deep Diffusion Devices

The deep diffusion ensures higher yield by preventing short between the front contact aluminum foil and p-base. However, it is still desirable to have shallow emitter to maximize the photocurrent as is observed in Table 7.4. An alternative approach to the emitter design of the spherical device is to employ the longer diffusion for deep emitters, and thin down the emitter by wet chemical etching at the front side after the spheres are attached to the foil(s). The doping profile of the emitter formed by diffusion follows an error function with the maximum at the surface. The high carrier density regions that suffer from accelerated recombination are removed during etch back process and thus thinning process increases the carrier collection efficiency in

the emitter layer as well. Furthermore, by thinning a deep emitter after bonding, the depth under the contact area remains intact; this is favorable as it is impossible to passivate the contact area that suffers from extremely high recombination velocity. By looking at the 10^5 cm/s SRV curve in Figure 7.9, it is obvious that a deeper junction is preferred in the regions with high surface recombination (classical selective emitter design).

Very deep junction devices were made using two regular diffusion steps with the intermediate glass removal, and a deep drive-in step at similar conditions (no doping source at the surface) after the glass of the second diffusion is removed. The deep drive-in step eliminates the risk of shunting devices and ensures yields of close to 100%. After front foil bonding, the spherical cells were then etched in 99:1 HNO_3:HF solution for different durations. The removed thickness is approximately proportional to the etching time. Characterization of a set of thinned devices is shown in Figure 7.11. The J_{sc} of the devices in this figure increases as is expected from the model. The V_{oc} however decreases in spite of the increase in the photocurrent due to dominance of the effect of high SRV on saturation current. By comparing the measurement results with simulation results for V_{oc} in Figure 7.9, it can be concluded that with the very deep junctions before thinning, the voltage first shows a slight increase induced by enhanced photocurrent, and starts to decrease as soon as the effect of surface recombination dominates the photocurrent enhancement.

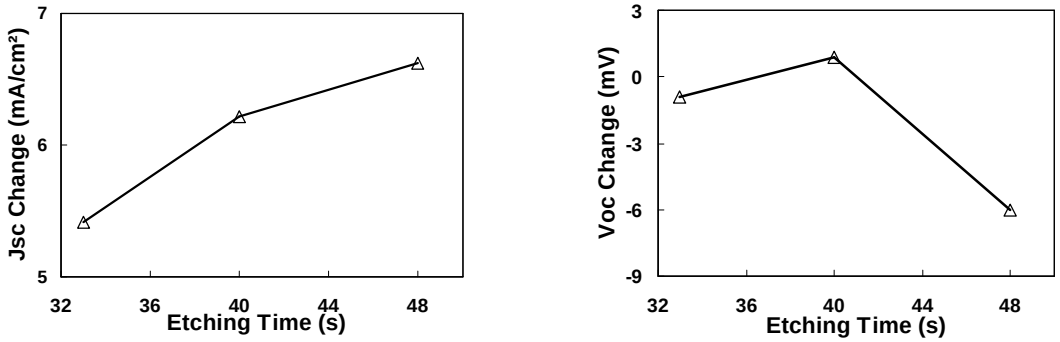

Figure 7.11: The change in the short circuit current density and open circuit voltage of spherical cells with the emitter thinned by different etching times.

Further thinning of the devices reveals that the increase in J_{sc} slows down for longer etching time and even reverses after 50 seconds as is shown in Figure 7.12. While the shallow emitter spherical devices were expected to have superior current (and requiring passivation to restore or enhance the voltage), a second mechanism appears as a result of the thinning process that directly counteracts the current enhancement. This current reduction is due to the fact that as the emitter is etched to thinner sheets with lower carrier concentration, the sheet resistance of the emitter and consequently the series resistance of the device drastically increase. This was not predicted by the simulation results of Figure 7.8. Thus, in addition to the demand for SiN passivation layer discussed in Section 7.1.6, the thinned emitter devices must be redesigned to overcome the series resistance problem or the enhanced photocurrent is masked by the high series resistance and does not appear in the actual I_{sc} of the device. In order to overcome this problem, a selective emitter etch back process is required to ensure a sufficiently low sheet resistance across the emitter, especially towards the contact areas as the current density increases.

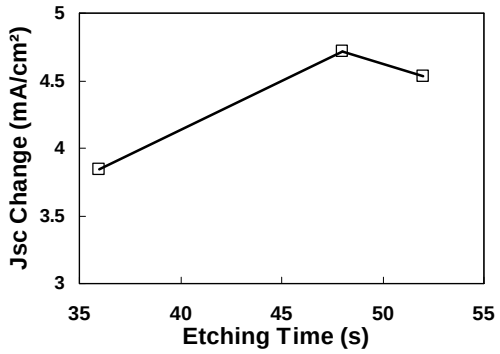

Figure 7.12: Reversal of short circuit current enhancement in thinned emitter devices due to series resistance.

7.3 Selective Emitter Spherical Devices

In the previous section, a wet etch-back process was considered for the shallow emitter design of spherical cells. Together with the nitride passivation of section 7.1, it was expected to provide

both high open circuit voltage and short circuit current. However, the increased series resistance of the thin emitter sheet apparently neutralizes the increase in the photocurrent under short circuit conditions. In this section, a dry etching process is employed to create a non-uniform emitter to avoid the increased series resistance.

7.3.1 Sheet Design for the Spherical Device Emitter

The emitter of the spherical device has an error function profile after the diffusion step; the diffusion is usually designed to reach a certain sheet resistance in conventional photovoltaic devices. Uniform etch-back of the emitter in spherical devices, as in the discussed thinning process, increases the sheet resistance by two mechanisms. The thinning removes outer layers of high carrier concentration, and what remains is a lowly doped emitter with reduced conductivity. Moreover, the thin sheet basically shows higher resistance even if the conductivity stays constant. The overall result is that the sheet resistance of the emitter drastically increases with etching time. Figure 7.13 shows the increase of sheet resistance after different etch-back depths for an initial error function diffused junction of 0.8 μm depth. It is worth noting that the generally accepted sheet resistance for a diffused emitter is below 100 Ω/sq [52]. Thus as the emitter is uniformly etched beyond a certain depth (more than 0.25 μm approximately), the sheet resistance exceeds the tolerable level; the actual tolerance yet depends on sphere size and path of carriers inside the emitter until reaching the foil contact point.

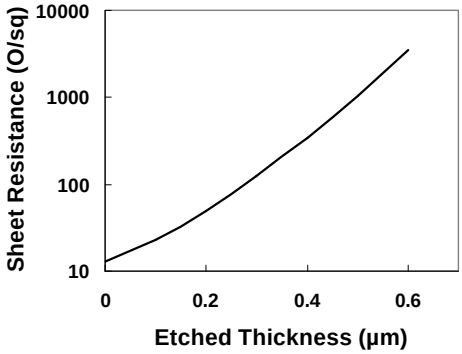

Figure 7.13: Calculation results of increased sheet resistance after uniform emitter thinning.

A solution to the series resistance increase due to emitter etch-back is a non-uniform or a selective emitter. While most of the photogenerated current originate from the areas close to the vertical axis at the top of the sphere, the carriers must travel towards the bottom of the sphere where the emitter contact is located. The current density increases along this path as a cumulative joining of the carriers from different angular slices of the sphere. From the results of electrical activity of different slices of a spherical photocell in Figure 5.12, the cumulative current can be calculated and is shown in Figure 7.14. The curve implies that the current density increases by nearly 15 times from the very topmost point of the sphere to the sides (at the equatorial plane).

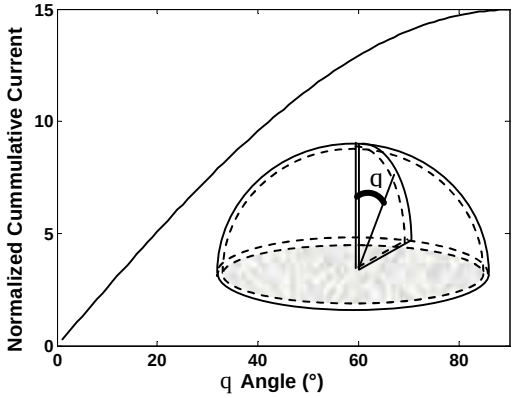

Figure 7.14: Calculation of normalized cumulative current along the emitter of a spherical cell.

While the photogeneration and carrier collection mainly occur at small angles (Figure 5.12) the sheet becomes responsible for carrying greater current at angles close to the equatorial plane. This suggests the optimized emitter design is a shallow emitter at the top and thicker sheet on the sides to both provide high carrier collection efficiency of a shallow emitter cell as recommended by simulation results and measurements of Section 7.2, and to prevent the I_{sc} degradation due to the voltage drop along the current path as was observed for wet chemically thinned down devices. In order to fabricate such selective emitters, as schematically demonstrated in Figure 7.15, a non-uniform etch-back process is required.

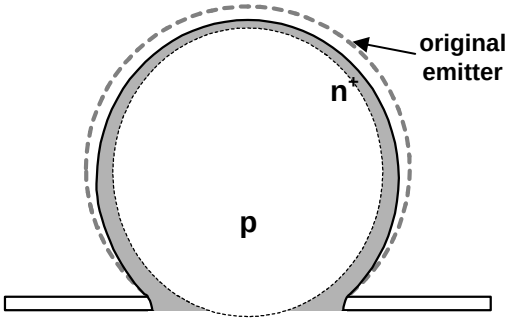

Figure 7.15: Schmatic representation of the etched back selective emitter spherical device.

7.3.2 Plasma Etch-Back Process for Selective Emitter

The non-uniform etch-back process for selective emitter fabrication is not achievable using a wet chemical etch. During wet etching, which can be realized through flooding or spraying, the solution reaches the whole spherical surface and thins the emitter uniformly. A dry process using plasma assisted etching can be employed to achieve the desired non-uniform etch.

Dry etching consists of two extremes of anisotropic sputtering (fully physical) and isotropic plasma etch (fully chemical). Reactive ion etching (RIE) is a process driven both chemically by reactive species and physically by momentum transfer from ions. The process conditions

including pressure, power (both direct capacitive and inductively coupled), and ion acceleration (or self-bias voltage) determine the etch rate and the anisotropy of the process.

The etch rate of an RIE process for a crystal can be defined as the number of atomic layers removed from the surface times the spacing of adjacent layers parallel to the surface of the specimen. We define the etch rate on a spherical surface at a certain point (r,θ,ϕ) as the thickness etched along the radial direction (Δr) at that point divided by etch time Δt. Considering the spherical symmetry and assuming etched thicknesses are orders of magnitude greater than the lattice constant, it can be concluded that the average spacing of the atomic layers removed from the surface of the sphere is constant irrespective of the local crystallographic orientation of the surface. In other words, the spherical etch rate (SER) can be defined as:

$$SER = \frac{\Delta r}{\Delta t} \propto \text{number of removed atomic layers} \tag{7.1}$$

The etch-back process was developed based on RIE with SF_6+H_2 gas precursor. Pressures varying from 10 to 250 mTorr, self-bias voltages of 14~50 V, and inductively coupled powers (ICP) of 0~100 W were used. The direct capacitive input power is adjusted by the system. The etch rates were measured using patterned planar 100 Si wafers positioned at different tilt angles on the cathode electrode of the RIE system and etched under different conditions. The step size resulting from the RIE process was measured using a surface profilometer, and the angle dependent etch rates were calculated.

Figure 7.16 shows the measured etch rates at different zenith angles for process conditions given in Table 7.5. The SER for a certain set of process conditions is not necessarily the extrapolation of the measured values as the interlayer distance of 100 crystal is different from the average interlayer distance in a shrinking sphere. Yet the trend and the angular profile do not change and only a scaling correction factor is involved.

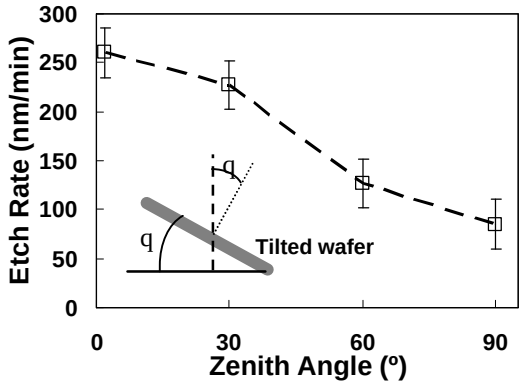

Figure 7.16: Extracted zenith angle (θ) dependence of etch rate for tilted wafers.

Table 7.5: RIE process conditions for etch rates of Figure 7.16

Pressure (mTorr)	Self-bias (V)	Power[1] (W)	ICP (W)	SF_6 (sccm)	H_2 (sccm)
50	23	27	0	20	5

1: measured value; power is set by the system

In order to design an optimized etch-back process for the spherical surface, it is helpful to control the angle dependent etch rate by controlling the process conditions. For any RIE etching process, the number of atoms removed from a surface depends on the flux and the energy of ions per unit area colliding with the atoms and the density of available reactive species in general. For a regular etching of a planar wafer resting horizontally on the cathode of the RIE system, a first order approximation is that the "base" etch rate (BER) is the sum of the ion momentum transfer assisted removal rate α and the pure chemical reaction rate β. The former depends on the pressure and self-bias voltage of the plasma process, and the letter is a function of total input power and pressure. If the specimen is held at a tilt angle with respect to the horizontal plane, the ion assisted etch rate changes as the per unit area flux of the incident ions decreases; this is assuming constant momentum and energy transfer yield during the collision of the ions (valid for this range of ion accelerations [53]). The purely chemical reaction rate is expected to remain constant as the number of colliding particles does not change in the neighborhood of a surface atom (excluding the effect of ions). With this first order estimation, SER at zenith angle θ is approximated as:

$$SER(q) = a \cdot \cos(q) + b \tag{7.2}$$

The base etch rate BER and the isotropy ρ of the RIE process can be then defined as:

$$BER = a + b \tag{7.3}$$

$$r = \frac{b}{a + b} \tag{7.4}$$

In developing the desired etch-back process, ρ is the critical parameter that creates the non-uniformity of the emitter thickness from the top to the sides as in Figure 7.15and must be optimized. Figure 7.16 depicts the angle dependent etch rate that can be optimized to produce the desired emitter configuration. It is worth noting that BER only determines the process time and does not influence the emitter shape.

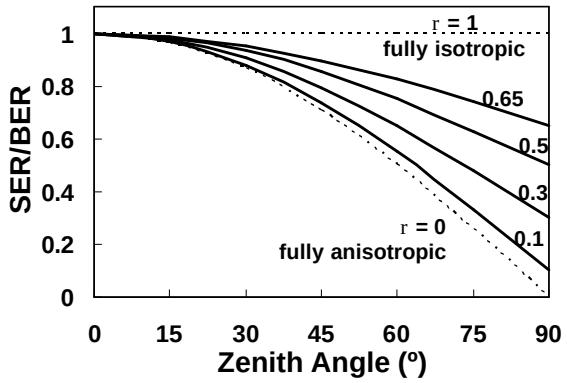

Figure 7.16: Zenith angle (θ) dependence of etch rate for tilted wafers.

In order to fabricate selective emitter devices, the process conditions dependence of the isotropy parameter ρ was investigated. In general, higher self-bias voltage drives the process towards anisotropy and higher pressure promotes isotropy. By inclusion of ICP power, the process drastically moves towards isotropic etching. Figure 7.17 show the effect of different process conditions on the isotropy parameter.

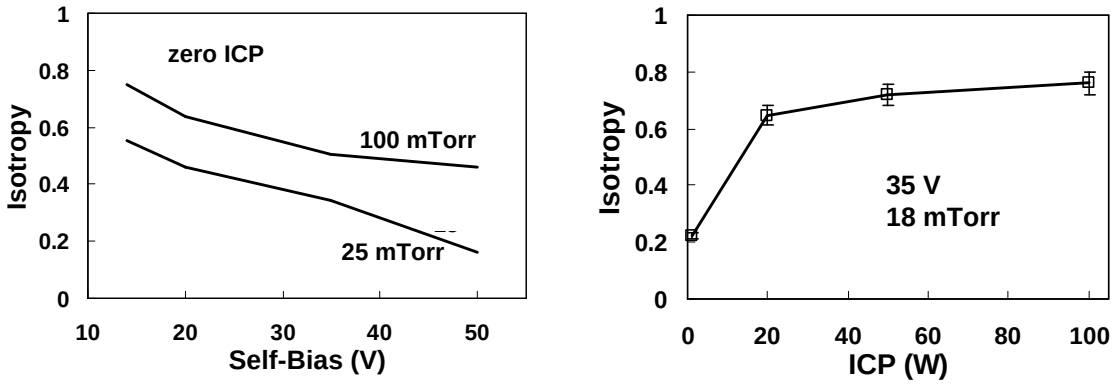

(a) (b)

Figure 7.17: Effect of used plasma conditions on anisotropy of the etch-back process.

7.3.3 Characterization of Selective Emitter Spherical Devices

Two modules (front foil only) consisting of spherical cells with deep junctions resulting from drive-in step were processed according to the uniform and the selective emitter etch-back RIE conditions of Table 7.6. Both modules were coated with PECVD nitride with process conditions of Table 7.2 for surface passivation at the same time after cleaning. Figure 7.18 shows the illuminated I-V curves of the two modules before and after the etch-back and passivation process. Since the emitter is considerably thinned down in the uniform device, the enhanced photocurrent quickly decreases even before the short circuit condition is reached. In contrast, the difference between the available photocurrent and the actual short circuit current in the selective emitter device is much less.

Table 7.6: Process conditions for uniform thinning and selective emitter devices

Process	Time (s)	Pressure (mTorr)	Self-Bias[1] (V)	ICP (W)	SF_6 (sccm)	H_2 (sccm)	BER (nm/s)	ρ
Uniform	161	150	0	100	20	5	3.1	0.85
Selective	69	15	40	0	20	5	7.2	0.12

1: set point value

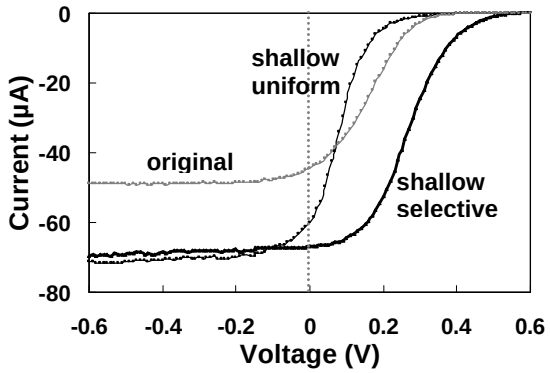

Figure 7.18: Illuminated I-V curves of uniformly thinned and selective emitter spherical cells.

The spectral response characterization of the two devices (Figure 7.19) shows that both devices enjoy enhanced blue response after the nitride passivation. Since the spectral response characterization is performed at a constant voltage (close to short circuit conditions) and the curves are normalized to eliminate the effect of the area coverage by the monochromatic beam, the considerable difference between the performance of the two devices due to series resistance is not observed in the spectral responses.

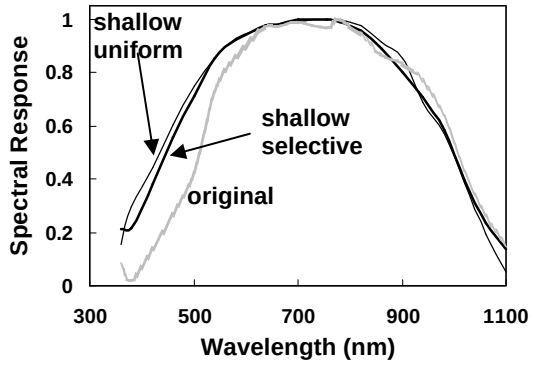

Figure 7.19: Spectral response of uniformly thinned and selective emitter spherical cells.

7.4 Other Viable Designs for Spherical Device

The proposed passivated selective emitter device is designed on the platform of the existing diffused n^+ emitter on p-type spheres. With the development of controlled lab scale sphere groth,

the selective emitter device can be designed and fabricated as self-aligned if the p-base/n-emitter device structure is changed to n-base/p-emitter. As Figure 7.20 shows, the front aluminum contact bonding at temperatures higher than the existing (400 ^{o}C) can lead to a high quality bonding, good contact, and a selectively formed deep junction underneath the high surface recombination velocity contact area.

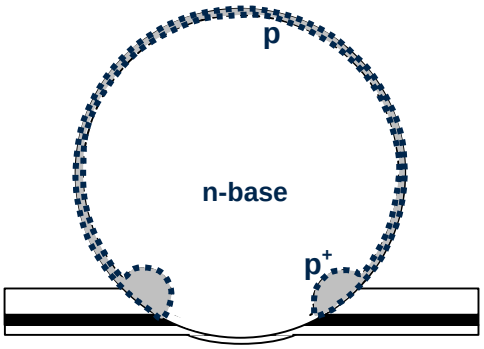

Figure 7.20: Proposed design for self aligned selective emitter device bases on n-type silicon spheres.

A second new design is the heterostructure spherical device, with the sphere as the base, and the emitter deposited as PECVD amorphous or nanocrystalline silicon film (Figure 7.21). This structure can benefit from the low thermal budget emitter formation [54] that can be extremely important in case of the spheres in which electronic defects might be affected by a high temperature diffusion step.

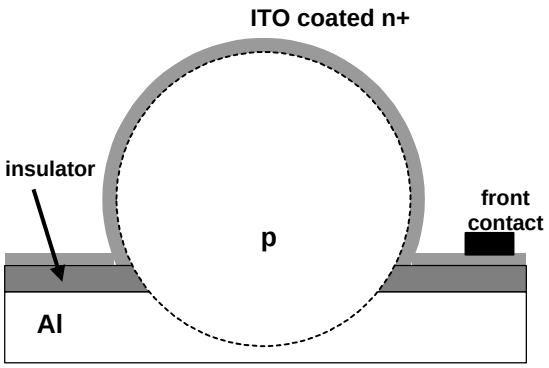

Figure 7.21: The heterostructure spherical devices with PECDV deposited amorphous or nanocrystalline emitter.

We have developed appropriate bonding process. Some experiments have also been conducted on forming insulator layer by baking solution based films and the PECVD amorphous emitter was deposited (Figure 7.22). However applying an insulator layer that forms a stable coating and is also plasma compatible for the next PECVD step seems to be the main challenge and must be further investigated. The insulator in Figure 7.22 turned out to be leaky and the structure was shorted. Applying too much of the solution for thicker insulator causes the liquid to climb up the sphere and cover the surface.

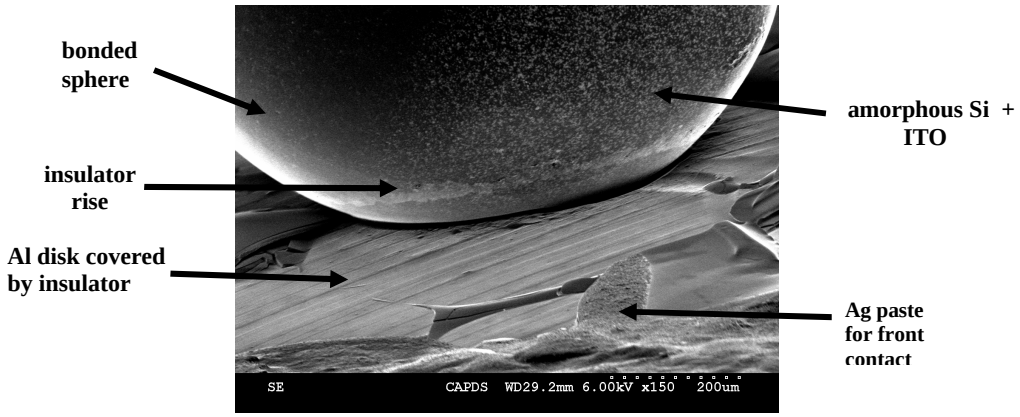

Figure 7.22: The preliminary developed heterostructure device; the insulator layer reveals poor adhesion to aluminum disk.

7.4 Summary

In the existing spherical cell technology, no surface passivation processes have been considered, and the bonding processes dictates fabrication of deep junction devices. These two result in poor blue response of the devices. Different processes were developed and implemented on the spherical devices to address the issues. Silicon nitride passivation was not effective with the deep emitter devices, and thinning the emitter uniformly introduced series resistance problems. Reactive ion etching was used to etch back the emitter non-uniformly to accomplish both high carrier collection efficiency and low loss current transport.

A brief investigation of the passivating SiN that was observed to also serve as anti-reflection coating suggests that the deposition rate changes as we move over the surface of the sphere from top to the sides. Optical analysis of the PECVD film can help to design deposition recipes that offer low reflection loss in addition to high passivation quality.

The RIE process can be further optimized according to the junction depth and doping density.

Chapter 8

Guidelines for Practical Manufacturability of Spherical Solar Cells

Spherical solar cells have unique features in both aspects of material and device that make them attracting for large scale industrial manufacturing. The low cost associated with the start material, the high throughput growth of the spheres, the simple cell fabrication, and the virtually unlimited module size (due to flexibility) are among the industrial advantages of the spherical cell technology.

With the recent growth in the installment of solar cells for grid connected purposes, new challenges emerge for the silicon PV industry. The silicon feedstock shortcoming is the major current issue and is inherently addressed in spherical technology. Moreover, cost reduction in material growth and cell fabrication may have less significant impact on the issue of cost effectiveness that it previously had given the back end electronics and power conditioning components costs, the shipment and installation costs, and other hidden costs of PV modules for grid connected electricity. This urges manufacturing of highly efficient cells (although costly) and in large volumes to break down the fixed expenses to the possible extent.

For the spherical technology to be a major player in the PV industry, enhanced efficiency, high throughput and large scale production are extremely important. On the other hand, there are

mechanical challenges at the module level to be overcome, in addition to the materials and device issues considered in this work. Therefore, any enhancement to the existing production technology, or any new design that includes modification of the machinery must be industrially up-scalable and maintain the simplicity and/or high throughput.

In this chapter, guidelines for the industrial implementation of some of the main proposed processes and designs are briefly discussed. In Section 8.1 the issue of high quality spherical crystal growth is considered. It is discussed that by tailoring the sequence of the thermal processes, growth of higher quality spheres is possible with no need to significant modification to the existing growth line. In Section 8.2, the feasibility of rapid thermal oxidation for surface passivation is discussed. It is mentioned that when appropriately combined with the optimization for high quality spheres as suggested in Section 8.1, the oxide layer can effectively enhance the surface without compromising the bulk quality; and it can be further helpful in the design of shallow diffusion and better back contact sintering without the risk of shorting the emitter contact to the base. In Section 8.3, the up-scalability of the plasma processes for selective emitter etch-back and nitride deposition is discussed. Dual purpose plasma reactors and reel-to-reel systems are proposed to fabricate the passivated selective emitter spherical devices without compromising the throughput. Section 8.4 presents the possibility of growing n-type silicon spheres for the self aligned selective emitter design, which requires a totally new production process flow.

8.1 Sphere Growth and Crystal Quality

The material properties of the spheres were studied in Chapter 3, and were correlated to the electronic parameters in Chapter 4. It was also shown in Section 3.2 that spheres contain lower impurity concentration levels compared to the start powder or granular melt stock. It was also shown that due to oxygen and high temperature processes, defects exist in the inner core of the

spheres in large densities. The structural defects in the bulk and oxygen are responsible for the low minority carrier lifetimes, and according to results of simulation in Section 5.4, the efficiency is limited as long as subsurface minority carrier and denuded zone depth are not simultaneously enhanced.

The thermal history of the silicon crystal has the most significant role in the precipitation and distribution of oxygen in the bulk. As was shown in Section 4.2, the sequence of the high temperature processes for silicon spheres can be tailored in a manner that precipitation, denuding, and interstitial distribution of oxygen lead to higher carrier lifetimes.

From industrial point of view, this can mean higher thermal budget expenditure for the production line. With the well established furnace technology, belt furnaces with very accurate zoning are available and the sphere formation and upgrading can be conducted sequentially in a longer system. With higher grade silicon melt sock, the need to multiple melt and etch processes can be eliminated and by the integration of powder fusing, crystal growth, annealing and other high temperature steps into a single belt furnace, high throughput and high material quality are achievable.

The approach actually increases the start material cost by switching from MG-Si or off-spec SG-Si to a higher grade melt stock. However, due to the reasons mentioned at the beginning of this chapter, the enhanced efficiency counterbalances this and the desired cost effectiveness can be guaranteed even with shipment and power system expenses included.

8.2 Oxidation and its Effect on Sphere Bonding and Sintering

One proposed surface passivation scheme for the spheres in Section 7.1 was rapid thermal oxidation (RTO) of the spheres prior to bonding to the front foil. The results in Section 4.2 reveal that with the existing process flow, the oxidation tends to overly degrade the bulk by activating

electronic defects, which masks the effect of surface passivation. However, if the optimization of interest is in place for the controlled thermal history of the sphere prior to diffusion, the device can benefit from RTO passivated surface after diffusion.

The RTO layer has significant impact on the device design by the superior passivation quality. In addition, the relatively impermeable oxide layer can act as a buffer against the aluminum spiking during the front contact bonding. The spiking is mainly due to segregation of silicon from the crystal to the aluminum, which strongly depends on the surface concentration of silicon atoms. Since the silicon is less concentrated at the oxide-aluminum interface, the transport of silicon into aluminum and the void formation is impeded. As was mentioned in Section 7.1, the bonding can be easily achieved with low contact resistance even in the presence of 10 nm thick oxide.

The impeded spiking is desirable for the design of shallower emitters (with milder diffusion and better cell quantum efficiency). It also creates more flexibility for curing of the insulating layer and sintering of the second (back) aluminum foil contact without a risk to short the devices.

8.3 Plasma Processing

The proposed passivated selective emitter device requires reactive ion etching (RIE) and plasma enhanced chemical vapor deposition (PECVD) of silicon nitride. While the processing times for the two plasma steps are not long (few minutes), the loading and the evacuation of the plasma chamber is a time consuming procedure. Moreover, PECVD chambers require cleaning on a regular basis as the film deposits on all the surfaces of the chamber; reactor cleaning is stoppage to the production line.

Currently, dual purpose reactors exist that combine RIE and PECVD. When combined with load lock, the dual purpose reactor can be easily integrated to the spherical production line with

reduced delay for loading/unloading. Interestingly, the RIE step for the selective emitter etch-back can be employed to clean the surfaces coated with nitride during PECVD.

Furthermore, the area of PECVD systems can be designed to accommodate a large number of large (6'x6') modules. PECVD systems with 13.56 MHz radio frequency power exist which are capable of accommodating up to 9 large modules with acceptably uniform film deposition [55]. However, the size requirement imposes a constraint on the maximum frequency that can be used for PECVD. Very high frequency (VHF) PECVD deposition of nitride, which has been reported to provide better passivation, is more difficult to implement on larger areas because of the shorter wavelength.

In addition to load lock dual purpose systems, the plasma processing can be implemented in a reel-to-reel (R2R) system. R2R systems with the capability of quick loading/unloading and several plasma processes have been assembled mainly for thin film photovoltaic applications. With pressurized/depressurized inter-reactor chambers, it has been possible to achieve several processes with no stoppage in between. The R2R is inherently a very high throughput technique although the flexibility of spherical modules may not be sufficient to actually roll them densely.

In both cases of large area dual purpose reactors and R2R, sphere cleaning steps must be included. The plasma cleaning with oxygen and hydrogen can be employed to remove any residue or contamination from RIE before nitride deposition. Interestingly, plasma hydrogenation can be integrated to such production line before nitride deposition to passivate bulk defects in the space charge region of the spherical device; a process that can potentially reduce the saturation current and enhance the ideality factor of spherical diodes. Figure 8.1 schematically shows the modification to the existing manufacturing line to achieve the passivated selective emitter device.

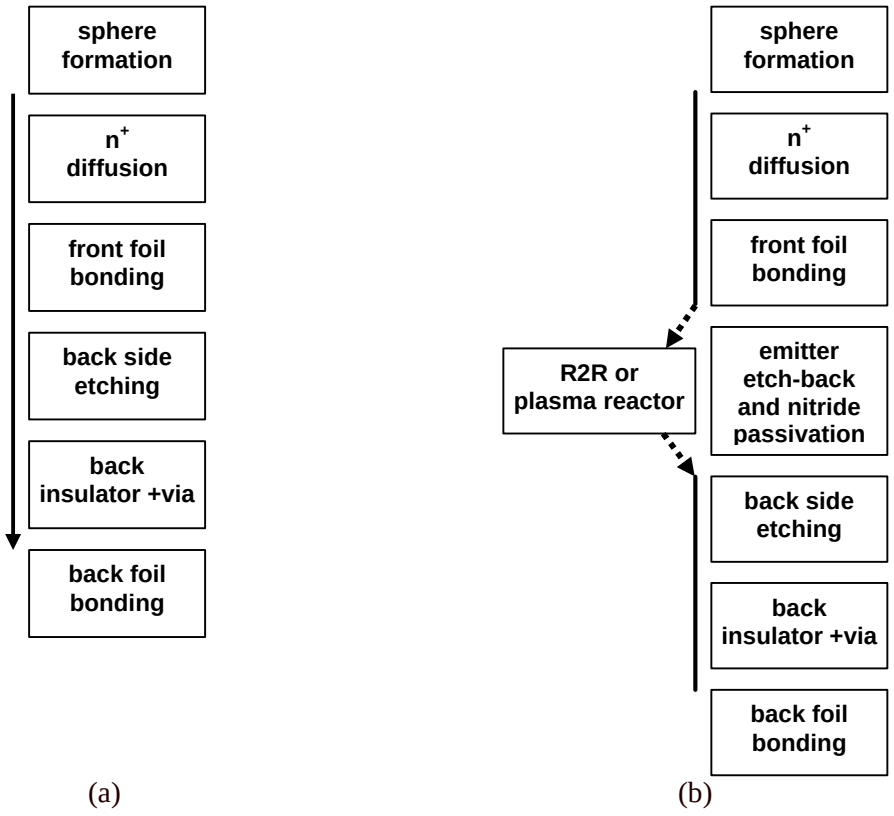

Figure 8.1: Comparison of the manufacturing flow for (a) the conventional spherical cells (b) the passivated selective emitter spherical cells.

8.4 n-type Spherical Silicon

The existing spherical silicon technology is based on p-type spheres. It was proposed in Section 7.4 that by forming a p^+-emitter on n-type spheres, the emitter depth and bonding problems will be automatically solved as a result of self aligned selective emitter formed under the silicide contact region. However, as mentioned in Section 3.3, the quick segregation of phosphorous during the melt and recrystallization, together with the slow boron segregation, tend to drive the formed sphere towards p-type. One viable solution can be the use of silicon melt stock that is overly doped with phosphorous. This is possible when higher grade silicon powder is available from technology losses such as kerf loss during wafering. A second approach to phosphorous rich melt stock is to soak the silicon powder in phosphoric acid and bake prior to fusing. Figure 8.2

depicts the new process flow required for manufacturing of the self aligned selective emitter spherical cells based on n-type sphere.

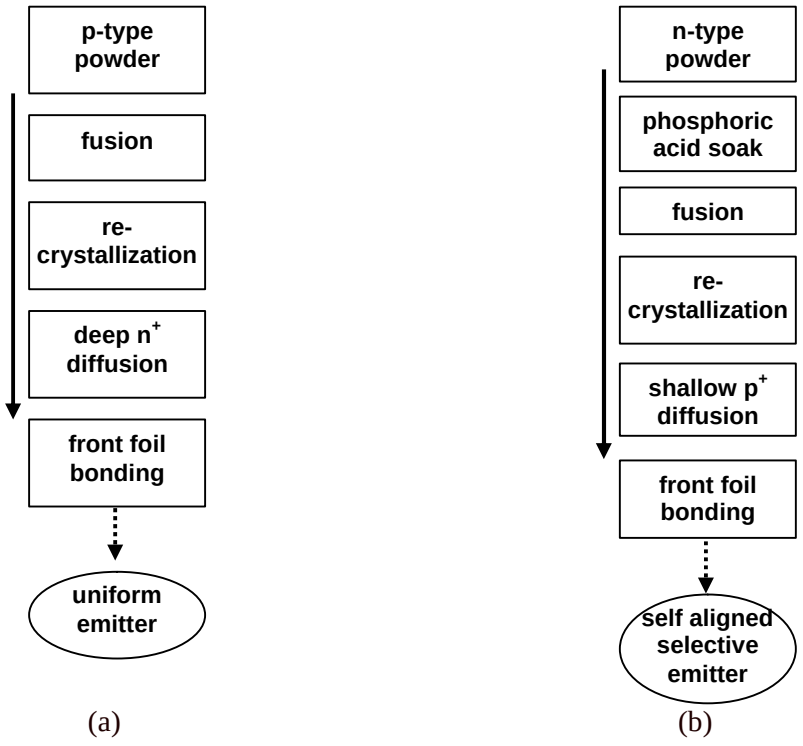

Figure 8.2: Comparison of the manufacturing flow for (a) the conventional n^+-p spherical cells (b) the self aligned selective emitter p^+-n spherical cells.

5.5 Summary

In order to reveal the industrial feasibility of the proposed designs, some guidelines were discussed for integration of the processes to the manufacturing line of the spherical modules. The guidelines are intended to reveal the feasibility of the new approaches on the platform of the already existing spherical technology which was made available for the purpose of this research. The practicality of implementing upgraded silicon sphere growth and surface oxidation were shown for the conventional device fabrication process flow. The integration of plasma processing and the redesign of the flow for n-type spheres were discussed targeting the fabrication of

selective emitter n^+-p and self aligned selective emitter p^+-n devices. The guidelines are presented to address the technological challenges beyond the material and device issues treated in the previous chapters of this thesis.

Chapter 9

Conclusion

This research was focused on spherical silicon as a photovoltaic material. The comprehensive study that has been carried out included material formation, characterization, analysis, device modeling, device design, and fabrication.

The material properties of the spherical silicon were characterized. Experimental results were presented on the aspects of crystallinity, impurities, and defects in the spheres. Electron diffraction was used to identify the single-crystallinity of the spheres. With secondary ion mass spectroscopy, evolution of impurities after crystallization was investigated and oxygen was highlighted as the dominant impurity. Defect etching was employed to monitor creation and annealing of structural defects in the spherical bulk at different steps of growth and processing.

The results of material properties characterization were used to further investigate the electronic properties of the spherical bulk. A model was developed to interpret the photoconductivity decay measurements on silicon spheres as the existing models are only valid for one dimensional planar wafer specimen. The model considers the three dimensional charge dynamics in spherical silicon, and relates the bulk minority carrier lifetime and surface recombination velocity to the measured photoconductivity signal. The developed model is able to include the spatial variation of carrier lifetime inside the spherical bulk. The results of the photoconductivity decay measurement were used to characterize the electronic quality of the spheres, monitor developed fabrication

processes, and extract bulk non-uniformities in the spheres. The extracted radial profile of minority carrier provided information on the depth of the denuding zone as well which is an indicative parameter of the effectiveness of the high temperature denuding step.

The extracted information on electronic properties of the spheres was input to in an opto-electric model developed to analyze and predict the performance of spherical devices. The optical section of the model calculates the photogeneration rate of carriers inside the sphere. The electrical section utilizes the calculated generation rate and solves the partial differential charge continuity equation to calculate the current for single-wavelength or solar-weighted photogeneration and for different voltages which are applied to the boundary condition of the equation. Thus the model can compute both spectral response and IV characteristics of spherical devices. A 3-dimensional simulation tool was created based on the developed model which allowed identifying the efficiency limitations and designing new structures.

Also characterization setups were developed specific to the spherical cells as tools to measure device characteristics. By direct probing of single spherical cells, it was made possible to characterize the spectral response and IV characteristics of individual cells, as well as an array consisting of several cells.

Based on simulation results, a selective emitter device was proposed. The new device allows higher photon absorption in the base, and provides a low resistance path for emitter current. A reactive ion etching process with controlled angle dependent etch rate was developed to non-uniformly etch-back the deep emitter of the spherical cell. A plasma enhanced chemical vapor deposition of silicon nitride was developed and optimized to passivate the surface of the device. The fabricated device was characterized using the developed setups, and was shown to have improvement in both spectral response and photocurrent over the conventional spherical cell.

Issues regarding the manufacturability of the proposed devices and processes were also discussed to provide a basis for the up-scaling and integration to the industrial manufacturing.

References

[1] *Natural Resources Canada (2001).* Photovoltaics for Buildings: Opportunities for Canada. Catalog Number M39-76/2001E, ISBN 0-662-30106-4.

[2] MARKETBUZZ 2006: *Annual World Solar Photovoltaic (PV) Industry Report*, http://www.solarbuzz.com/Marketbuzz2006-intro.htm.

[3] A. Goetzberger, C. Hebling, and H. W. Schock, "Photovoltaic Materials, History, Status and Outlook," Materials Science and Engineering, vol. R40, pp.1-46, 2003.

[4] *Photovoltaic Industry Statistics: Costs*, http://www.solarbuzz.com/StatsCosts.htm.

[5] J. Szlufcik, S. Sivoththaman, J. Nijs et al, "Low Cost Industrial Technologies of Crystalline Silicon Solar Cells," *Proceedings of the IEEE*, vol. 85, pp.711-730, 1997.

[6] F. Shimura, *Semiconductor Silicon Crystal Technology*, Academic Press, 1989, ISBN 0-126-40045-8.

[7] J. R. McCormick, "polycrystalline Silicon Technology Requirements for Photovoltaic Applications," in C. P. Khattak and K. V. Ravi, Silicon Processing for Photovoltaics I, *Materials Processing Theory and Practice*, vol. 5, 1-47, North-Holland, 1985, ISBN 0-444-86933-6.

[8] J. A. Amick, J. P. Dismukes, R. W. Francis et al, "Improved High Purity Arc Furnace for Solar Cell," *Journal of the Electrochemical Society*, vol. 132, pp.339-345, 1985.

[9] L. P. Hunt, V. D. Dosaj, "Progress on the Dow Corning Process for Solar Grade Silicon," *2nd European Photovoltaic Solar Energy Conference*, pp.98-105, 1979.

[10] M. F. Browning, J. M. Blocher, W. J. Wilson et al, "Evaluation of Selected Chemical Processes for Production of Low Cost Silicon," *12th IEEE Photovoltaic Specialists Conference*, pp.130-136, 1976.

[11] W. H. Reed, T. N. Meyer, M. G. Fey et al, "Development of a Process for High Capacity Arc Heater Production of Silicon," *31st IEEE Photovoltaic Specialists Conference*, pp.370-375, 1978.

[12] J. R. Davis, A. Rohatgi, R. H. Hopkins et al, "Impurities in Silicon Solar Cells," *IEEE Transaction on Electron Devices*, vol. 27, pp.677-687, 1980.

[13] W. Keller and A. Muhlbauer, *Floating Zone Silicon*, Marcel Dekker Inc, 1981, ISBN 0-824-71167-x

[14] R. L. Lane, "The Czochralski Method for Photovoltaic Applications," in C. P. Khattak and K. V. Ravi, Silicon Processing for Photovoltaics I, *Materials Processing Theory and Practice*, vol. 5, pp.49-84, North-Holland, 1985, ISBN 0-444-86933-6.

[15] C. P. Khattak and F. Schmid, "Growth of Silicon Ingots by HEM for Photovoltaic Applications," in C. P. Khattak and K. V. Ravi, Silicon Processing for Photovoltaics II, *Materials Processing Theory and Practice*, vol. 6, pp.153-183, North-Holland, 1987, ISBN 0-444-87024-5.

[16] T. F. Ciszek, "The Growth of Silicon Ribbons for Photovoltaics by Edge Supported Pulling," in C. P. Khattak and K. V. Ravi, Silicon Processing for Photovoltaics I, *Materials Processing Theory and Practice*, vol. 5, 131-165, North-Holland, 1985, ISBN 0-444-86933-6.

[17] J. P. Kalejs, "Progress in Development of EFG Process Control in Silicon Ribbon Production for Photovoltaic Applications," in C. P. Khattak and K. V. Ravi, Silicon

Processing for Photovoltaics II, *Materials Processing Theory and Practice*, vol. 6, pp.185-254, North-Holland, 1987, ISBN 0-444-87024-5.

[18] H. Lange, I. A. Schwirtlich, "Ribbon Growth on Substrate (RGS) – a New Approach to High Speed Growth of Silicon Ribbons for Photovoltaics," *Journal of Crystal Growth*, vol. 104, pp.108-112, 1990.

[19] R. Flackenberg, G. Hoyler, J. G. Grabmaier et al, "Si Ribbon Growth by the HSW Technique: Current Status and Prospectives," *19th IEEE Photovoltaic Specialists Conference*, pp.369-371, 1987.

[20] C. Belouet, "Growth of Silicon Ribbons for Terrestrial Solar Cells by the RAD Process," in C. P. Khattak and K. V. Ravi, Silicon Processing for Photovoltaics I, *Materials Processing Theory and Practice*, vol. 5, 85-129, North-Holland, 1985, ISBN 0-444-86933-6.

[21] A. Goetzberger and A. Rauber, "Development in Silicon Sheet Technologies," *12th IEEE Photovoltaic Specialists Conference*, pp.1371-1374, 1988.

[22] C. Okamoto, T. Minemoto, M. Murozono et al, "Defect Evaluation of Spherical Silicon Cells Fabricated by Dropping Method," *Japanese Journal of Applied Physics*, vol. 44, pp.7805-7808, 2005.

[23] S. Omae, T. Minemoto, M. Murozono et al, "Crystal Growth Mechanism of Spherical Silicon Fabricated by Dropping Method," *Japanese Journal of Applied Physics*, vol. 45, pp.3577-3580, 2006.

[24] S. Omae, T. Minemoto, M. Murozono et al, "Crystal Characterization of Spherical Silicon Solar Cell by X-ray Diffraction," *Japanese Journal of Applied Physics*, vol. 45, pp.3933-3937, 2006.

[25] C. Okamoto, K. Tsujiya, T. Minemoto et al, “Reduction in Dislocation Density of Spherical Silicon Solar Cells Fabricated by Decompression Dropping Methos,” *Japanese Journal of Applied Physics*, vol. 44, pp.8351-8355, 2005.

[26] Z. Liu, T. Nagai, A. Masuda et al, “Seeding Method with Silicon Powder for the Foarmation of Silicon Spheres in the Drop Method,” *Journal of Applied Physics*, vol. 101, pp.0935051-0935052.

[27] S. Omae, T. Minemoto, M. Murozono et al, “Effects of Hydrogen Passivation for Spherical Silicon Solar Cells Fabricated by Dropping Method,” *Japanese Journal of Applied Physics*, vol. 45, pp.1515-1519, 2006.

[28] D. Hironiwa, T. Minemoto, C. Okamoto et al, “Phosphorous Gettering on Spherical Si Solar Cells Fabricated by Dropping Method,” *Japanese Journal of Applied Physics*, vol. 45, pp.4939-4942, 2006.

[29] J. D. Levine, D. K. Woodall, V. E. Knepprath at al, “Upgrading of Silicon Spheres Using an Airjet Grinder,” *23rd IEEE Photovoltaic Specialists Conference*, pp.201-204, 1993.

[30] R. R. Schmit, M. D. Hammerbacher et al, “A Review of Spheral Solar Technology,” *Advances in Solar Energy*, vol.10, pp.347-379, 1995.

[31] R. R. Schmit, “Highlights of Texas Instruments Spheral Solar Technology,” *AIP Conference Proceedings*, vol. 303, pp.297-302, 1994.

[32] J. D. Levine, “Design Criteria of the Spheral Solar Cell,” *AIP Conference Proceedings*, vol. 268, pp.47-51, 1992.

[33] J. K. Arch, J. S. Reynolds, M. D. Hammerbacher et al, "Characterization of Silicon Spheres for Spheral Solar Cells," *24th IEEE Photovoltaic Specialists Conference*, pp.1364-1365, 1994.

[34] R. R. Schmit, B. Felder, and G. Hotchkiss, "Recent Progress in the Design and Fabrication of Spheral Solar Modules," *23rd IEEE Photovoltaic Specialists Conference*, pp.1078-1081, 1993.

[35] G. Stevens, M. D. Hammerbacher, P Sharrock et al, "Latest Developments in Spheral Solar Process and Design," *19th European Photovoltaic Energy Conference*, pp.1270-1271, 2004.

[36] F. Shimura, *Oxygen in Silicon*, Academic Press, 1994, ISBN 0-127-52142-9.

[37] K. L. Keung, L. Cheng, "Analysis of the Interaction of a Laser Pulse with a Silicon Wafer: Determination of Bulk Lifetime and Surface Recombination," *Journal of Applied Physics*, vol. 61, pp.2282-2293, 1987.

[38] Y. I. Ogita, "Bulk Lifetime and Surface Recombination Velocity Measurement Method in Semiconductor Wafers," *Journal of Applied Physics*, vol. 79,pp.6954-6960, 1996.

[39] D. K. Schroeder, *Semiconductor Material and Device Characterization*, Wiley-Interscience, 1998, ISBN 0-471-73906-5.

[40] R. K. Ahrenkiel, D. Levi, and J. Arch, "Recombination Lifetime Studies of Silicon Spheres," *Solar Energy Materials and Solar Cells*, vol. 41/42, pp.171-181, 1996.

[41] M. Kunst and G. Beck, "The Study of Charge Carrier Kinetics in Semiconductors by Microwave Conductivity Measurements," *Journal of Applied Physics*, vol. 60, pp.3558-3566, 1996.

[42] R. R. Schmit, J. S. Reynolds et al, "The Effect Silicon Purity on Spheral Solar Cell Processing and Performance," *1st World Conference on Photovoltaic Energy Conversion*, pp.1603-1606, 1994.

[43] R. K. Ahrenkiel, D. H. Levi and J. Arch, "Minority Carrier Lifetime Studies of Silicon Spheres," *World Conference on Photovoltaic Energy Conversion*, pp.1368-1371, 1994.

[44] E. Yablonovitvh, "Statistical Ray Optics," *Journal of Optical Society of America*, vol. 72, pp.899-907, 1982.

[45] P. Campbell and M. A. Green, "Light Trapping Properties of Pyramidally Textured Surfaces," *Journal of Applied Physics*, vol. 62, pp.243-249, 1987.

[46] R. S. Longhurst, *Geometrical and Physical Optics*, Longman, 1973.

[47] M. A. Green, *Solar Cells: operating Principles, Technology, and System Applications*, Prentice-Hall, 1982.

[48] H. J. Moller, *Semiconductors for Solar Cells*, Artech House, 1993.

[49] B. S. Richards, J. E. Cotter et al, "Novel Uses of TiO_2 in Crystalline Silicon Solar Cells," *28th IEEE Photovoltaic Specialists Conference*, pp.15-22, 2000.

[50] Armin G. Aberle, *Crystalline Silicon Solar Cells: Advanced Surface Passivation and Analysis*, University of New South Wales, 2004, ISBN 0-733-40645-9

[51] W. Lanford and M. Rand, "The Hydrogen Content of Plasma Deposited Silicon Nitride," *Journal of Applied Physics*, vol. 49, pp.2473-2477, 1978.

[52] A. Goetzberger, J. Knobloch and B. Voss, *Crystalline Silicon Solar Cells*, Wiley, 1998, ISBN 0-471-97144-8.

[53] P. G. Gloerse, “Ion Beam Etching,” *Journal of Vacuum Science and Technology*, vol. 12, pp.28-35, 1975.

[54] M. F. Baroughi and S.Sivoththaman, “A Novel Silicon Photovoltaic Cell Using a Low Temperature Quasi Epitaxial Silicon Emitter,” *IEEE Electron Device Letters*, vol. 28, pp.575-577, 2007.

[55] A. Kenanoglu, D. Borchert, C. Ballif et al, “New Large Area PECVD System for a-SiN:H Deposition at 13.56 MHz, *3rd World Conference on Photovoltaic Energy Conversion*, pp.1515-1518, 2003.